THE FUNDAMENTAL APPLICATION OF DECISION ANALYSIS TO MANUFACTURING

by

Jaydeep Mohan Karandikar

A dissertation submitted to the faculty of
The University of North Carolina at Charlotte
in partial fulfillment of the requirements
for the degree of Doctor of Philosophy in
Mechanical Engineering

Charlotte

2013

Approved by:

_____
Dr. Tony Schmitz

_____
Dr. John Ziegert

_____
Dr. Ertunga Ozelkan

_____
Dr. Tom Suleski

ABSTRACT

JAYDEEP MOHAN KARANDIKAR. The fundamental application of decision analysis to manufacturing.
(Under the direction of DR. TONY SCHMITZ)

Machining models are available to predict nearly every aspect of machining processes. In milling, for example, models are available to relate stability, part accuracy (from forced vibrations during stable machining), and tool wear to the selected operating parameters, material and tool properties, tool geometry, and part-tool-holder-spindle-machine dynamics. The models capture the underlying physics. However, models are deterministic and do not take into account the uncertainty that exists due to the model assumptions, model inputs, and factors that are unknown. Therefore, to enable reliable parameter selection using process models, uncertainty should be included in the formulation. This research will apply the normative mathematical framework of decision theory to select optical machining parameters while taking into account the inherent uncertainty in milling processes. The objective function will be profit because it (arguably) represents the decision maker's primary motivation in the manufacturing environment. The objective of this research is to select the optimal machining parameters which minimize cost while considering the uncertainty in tool life and stability for a given machine, tool, tool path and workpiece material.

DEDICATION

Dedicated to my family.

ACKNOWLEDGMENTS

I would like to thank my advisor, Dr. Tony L. Schmitz, for his ideas and for providing the opportunity to participate in this experience. I have grown both professionally and personally under his guidance. I would also like to thank the other members of the supervisory committee, Dr. John Ziegert, Dr. Ertunga Ozelkan and Dr. Tom Suleski, for their participation. I would also like to thank Mike Traverso and Dr. Ali Abbas for introducing me to the fascinating discipline of decision analysis and their inputs to the research.

I would like to thank all my lab mates and faculty of the Machine Tool Research Center at the University of Florida and High-Speed Machining Laboratory at the University of North Carolina at Charlotte for making the research possible. Furthermore, I would like to specifically thank Christopher Tyler and Vasishta Ganguly for their assistance and guidance throughout this effort. Lastly, I thank my family and Prachi Namjoshi for their continued support and encouragement.

TABLE OF CONTENTS

LIST OF TABLES

LIST OF FIGURES

CHAPTER 1: INTRODUCTION

1.1 Motivation and Research Objective

Machining models are available to predict nearly every aspect of machining processes. In milling, for example, models are available to relate stability, part accuracy (from forced vibrations during stable machining), and tool wear to the selected operating parameters, material and tool properties, tool geometry, and part-tool-holder-spindle-machine dynamics. While these models capture the underlying process physics, uncertainty exists due to the model assumptions, model inputs, and factors that are unknown. For example, it has been observed in practice that stable points may lie above or below the stability lobe diagram constructed using deterministic models, even though every effort has been made to accurately identify the model inputs. This is due to the uncertainties in, for example, the force model coefficients and the dynamic response of the machine which are not considered by deterministic models. Similarly, deterministic models for tool life are limited in application because tool life is generally considered to be stochastic due to the complex nature of the tool wear process and tool-to-tool performance variation. Therefore, to enable reliable parameter selection using process models, uncertainty should be included in the formulation.

Decision analysis provides a formal and logical procedure for decision making under uncertainty. The approach incorporates the state of information, preferences, and available alternatives to select the best decision. Information is described in terms of a joint probability distribution that captures the uncertainty about the possible outcomes for each alternative. In addition, decision analysis enables the value of

information (experimentation) to be calculated. While the additional information obtained from experiments (e.g., tool wear or stability tests) reduces uncertainty, these experiments require time and money. Naturally, an experiment is only worthwhile if the value of additional information exceeds the cost of performing that experiment. Decision analysis places a dollar value on the information gained from an experiment prior to performing it. The primary motivation for defining the value of information is to optimize the selection of experiments. The experimental test point should be the one which adds the most (expected) value to the profit.

The objective of this research is to apply the normative mathematical framework of decision theory to select optical machining parameters while taking into account the inherent uncertainty in milling processes. The objective function will be profit because it (arguably) represents the decision makers primary motivation in the manufacturing environment.

1.2 Stability Lobes in Milling

High speed machining (HSM) has made significant technological advances in recent years. Improved milling spindle designs enable speeds of 20000 rpm and higher with powers exceeding tens of kW. High material removal rates (MRR) can be obtained by machining at larger depths of cut and increased spindle speeds. However, a limitation to machining at higher depths of cut is chatter or unstable cutting. In milling, relative motion between a rotating cutter and workpiece is responsible for material removal. As the cutter is engaged, it experiences a cutting force which causes the tool to vibrate. The tool vibrations are imprinted on the workpiece leaving behind a wavy surface. The wavy surface left behind by one tooth is removed by the following tooth. Thus, surface regeneration occurs from one tooth to the next. The instantaneous chip thickness depends on the state of vibration of the current tooth and the surface left behind by the previous tooth and governs the cutting force. If the two surfaces are in phase, the chip thickness varies only according to cut geometry. This gives periodic

cutting forces and tool vibrations and provides stable cutting conditions. However, an out of phase profile results in a variable chip thickness which affects the cutting force and, subsequently, the tool vibrations. The resulting vibrations again affect the chip thickness. This feedback mechanism may result in self-excited vibrations, or chatter, in milling. The foundation for the stability in machining can be traced to papers by Tlusty, Tobias, and Merrit [1, 2, 3, 4], which, in turn, followed earlier work by Arnold [5]. Subsequent work involved developing modeling techniques such as time domain simulations, frequency domain analyses, and temporal finite element methods to predict the stability behavior in HSM [6, 7, 8, 9].

Stability lobes separate stable operating points from unstable, or chatter, points. All operating points below the stability boundary are predicted to be stable while the ones above are unstable. Figure 1.1 shows a typical stability lobe diagram for milling.

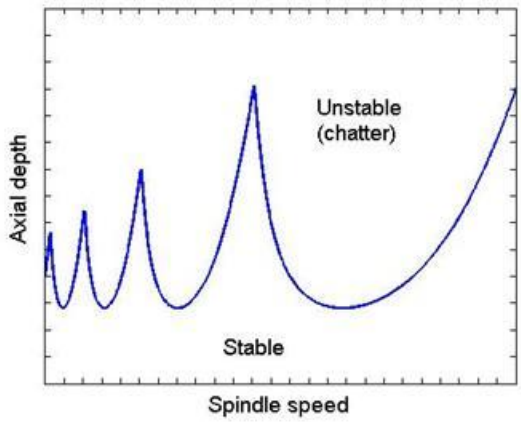

Figure 1.1: Typical stability lobe diagram for milling which identifies stable and unstable (chatter) zones.

The models used to predict the stability lobes require the tool point frequency response function (FRF), tool geometry, cutting parameters, and cutting force coefficients. The stability lobes are calculated at a certain radial depth of cut. The user can select optimum operating conditions for spindle speed and axial depth of cut based on this diagram.

1.3 Tool Wear

Tool wear in machining is damage to the cutting edge, often in the form of tool material loss, due to interaction with the workpiece during cutting. Tool wear can ultimately result in catastrophic failure of the cutting edge. Tool wear is undesirable as it affects the cutting forces and quality of the machined surface. Replacing a worn tool requires tool changing time, which increases the cost of the product in addition to the tool cost. Tool wear also results in increased cutting forces and temperatures. The various mechanisms that can cause tool wear include mechanical microbreakages, abrasion, adhesion, diffusion, and oxidation [10]. Figure 1.2 shows the various forms of tool wear.

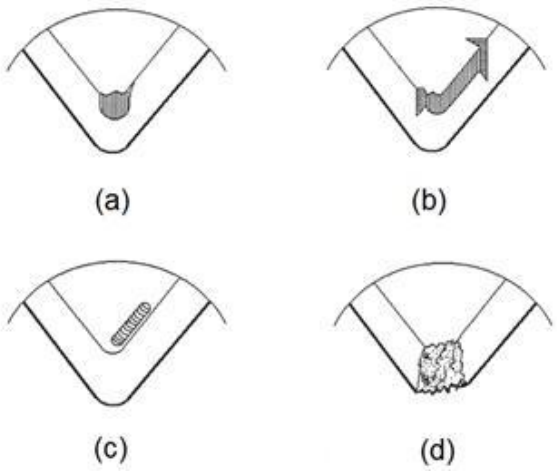

Figure 1.2: Various forms of tool wear A) Nose wear B) Notch and flank wear C) Crater wear D) Plastic/breakage [11].

Flank wear is a common wear feature and can be used to monitor tool wear. Flank wear is caused by abrasive wear of the main cutting edge against the workpiece and occurs on the tool flank face over the length equal to axial depth of cut in zero helix end milling. Flank wear is expressed in terms of the flank wear width (FWW). Flank wear increases with cutting time as shown in Figure 1.3 [10]. The tool life is based on the time required for the maximum FWW to reach a preselected value. For milling processes, according to ISO, the permissible average value of FWW is 0.3 mm in

the case of uniform wear or 0.6 mm maximum in case of irregular wear for cemented carbides [12]. The increase in flank wear width consists of three parts:

- initial rapid wear where FWW quickly increases
- uniform wear where FWW increases at a constant rate
- final accelerated wear leading to a catastrophic failure of the tool

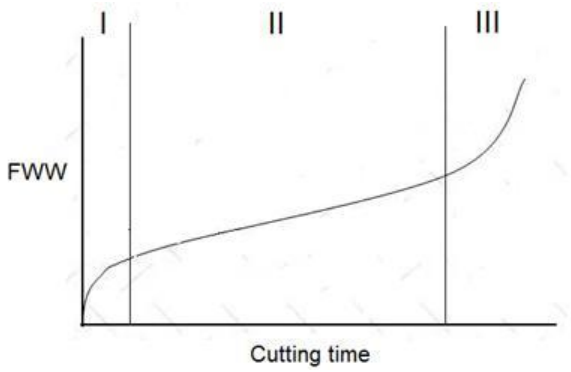

Figure 1.3: Increase in flank wear width with cutting time. I) Initial rapid wear, II) Uniform Wear, and III) Final wear (catastrophic failure) [10].

1.4 Decision Analysis

The term decision analysis was coined by Howard who defined it as "a logical procedure for the balancing of the factors that influence a decision. The procedure incorporates uncertainties, values, and preferences in a basic structure that models the decision. Typically, it includes technical, marketing, competitive, and environmental factors. The essence of the procedure is the construction of a structural model of the decision in a form suitable for computation and manipulation; the realization of this model is often a set of computer programs" [13]. See [14, 15, 16, 17] for the concepts and early discussions in the field of decision analysis.

The approach incorporates information, preferences, and available alternatives to derive the best decision alternative. Information is described in terms of a joint probability distribution that captures the uncertainty about the possible outcomes for

each alternative and uses Bayesian inference to update knowledge when new information is revealed. Bayesian inference provides a systematic and formal procedure of updating beliefs with observational data. In Bayesian inference, a probability is represented as a degree of belief. It provides a framework of incorporating judgment (prior beliefs) with observational data. Let the prior distribution about an uncertain event, A, be $\mathrm{P}(A)$, the likelihood of obtaining an experimental result B given that event A occurred be $\mathrm{P}(B|A)$, and the probability of receiving experimental result B (without knowing A has occurred) be $\mathrm{P}(B)$. Bayes' rule is used to determine the posterior belief about event A after observing the experiment results, $\mathrm{P}(A|B)$, as shown in Eq. 1.1. Using Bayes' rule, information gained through experimentation can be combined with the prior prediction about the event to obtain a posterior distribution [18, 19]. The Bayesian approach can incorporate data and/or existing models; this makes it an attractive candidate to update information in experimental settings.

$$P(A|B) = \frac{P(B|A)P(A)}{P(B)} \tag{1.1}$$

In decision theory, preferences are captured using a von Neumann-Morgenstern utility function over monetary amounts to represent the preferences under risk [20]. Given a value model that converts parameter values in a deterministic setting into dollar equivalents, a von Neumann-Morgenstern utility that captures preferences under uncertainty can be constructed. The optimal decision is the one that maximizes the von Neumann-Morgenstern expected utility. Decision theory also enables the value of a decision situation given an arbitrary knowledge state to be determined. As a result, a value, referred to as the value of information, can be assigned to gaining knowledge, such as the outcome of an experiment [16]. With this approach, optimal experiment design can be formulated as a sequential decision problem under uncertainty. The type and number of experiments that maximize expected utility are selected to determine the optimal sequence of experiments. The application of decision analysis to

value oil (petroleum) properties and make decisions about new well drilling is well documented [21, 22, 23, 24, 25, 26, 27, 28, 29].

The remainder of the dissertation is organized as follows. Chapter 2 describes the application of Bayesian inference and decision analysis to a marble drawing example. Chapter 3 describes milling force modeling using Bayesian inference. Chapter 4 shows optimal parameter selection considering uncertainty in stability using a random walk approach. Chapter 5 describes process damping coefficient identification and experimental selection in milling using Bayesian inference. Chapter 6 describes Bayesian updating of tool life and optimal machining parameter selection considering uncertainty in tool life. Chapter 7 describes the steps for combining uncertainty in tool life and stability of optimal parameter selection in titanium machining. Future scope and conclusions are listed in Chapter 8.

CHAPTER 2: INFERENCE, DECISION AND EXPERIMENTATION

To explain decision theory and Bayesian inference, a marble drawing from a jar example is demonstrated, where the number of blue marbles in a jar containing both red and blue marbles is considered uncertain. The probability of the number of blue marbles in the jar is updated using Bayes' rule and observations about the color of the marble drawn with replacement. The problem is then framed in a decision setting where the user has to guess the number of blue marbles based on a profit function. Observation possibilities are evaluated for the case where the number of observations must be decided *a priori* and for the case where observations follow sequentially and can be stopped at any point.

2.1 Inference

A jar has four marbles, some of which are blue and the rest of which are red. The exact number of blue marbles is not known and is thus uncertain. The goal is to update the beliefs about the number of blue marbles in the jar given discrete observations. In an observation a marble is drawn from the jar, its color is identified, and it is replaced in the jar. For the jar problem, Bayes' rule is given by:

$$P(blue|observation) = \frac{P(observation|blue)P(blue)}{P(observation)} \tag{2.1}$$

where P($blue|observation$) is the posterior probability of the number of blue marbles given an observation, P($observation|blue$) is the likelihood of observing a result given the number of blue marbles, P($blue$) is the prior belief of the number of blue marbles, and P($observation$) is the probability of an observation, which acts as a normalization

constant.

2.1.1 Prior

The first step in Bayesian updating is to decide the prior probability for the uncertain variable of interest. For the prior, it is assumed that all possible values of the number of blue marbles (0, 1, 2, 3 or 4) were equally likely (or have an equal probability). In Bayesian terms, this is called a uniform or a non-informative prior. The uniform prior implies that there is no information available to prefer one value over another. There are five possible outcomes; each outcome is assigned a probability of 0.2. Figure 2.1 shows the prior probability of the number of blue marbles, P(*blue*).

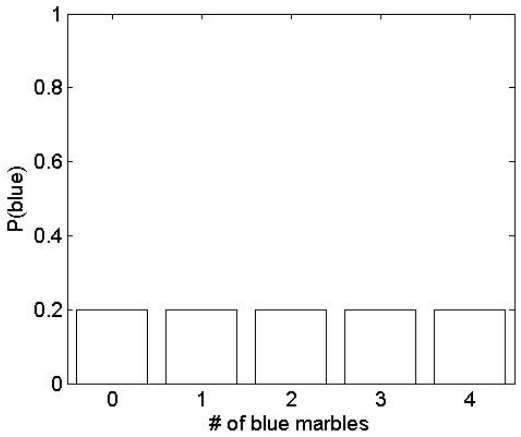

Figure 2.1: Prior probability of the number of blue marbles.

2.1.2 Bayesian Updating Given Discrete Observations

According to the Bayes' rule, the posterior probability is proportional to the product of the prior and the likelihood. Note that the posterior probability should be normalized so that the sum of all probabilities is equal to unity. Bayes' rule (Eq. 2.1) is used to calculate the posterior probability given an observation of the color of the drawn marble. The likelihood is defined as the probability that a blue marble is observed given the number of blue marbles. To illustrate, the likelihood that a blue marble is observed given that there are 0 blue marbles in the jar is zero. The

Table 2.1: Posterior probability given $b = 1$.

x	Prior	Likelihood ($b = 1$)	Posterior (non-normalized)	Posterior (normalized)
0	0.2	0	0	0
1	0.2	0.25	0.05	0.1
2	0.2	0.5	0.1	0.2
3	0.2	0.75	0.15	0.3
4	0.2	1	0.2	0.4
		Σ	0.5	1

Table 2.2: Posterior probability given $b = 0$.

x	Prior	Likelihood ($b = 0$)	Posterior (non-normalized)	Posterior (normalized)
0	0.2	1	0.2	0.4
1	0.2	0.75	0.15	0.2
2	0.2	0.5	0.1	0.2
3	0.2	0.25	0.05	0.1
4	0.2	0	0	0
		Σ	0.5	1

likelihood that a blue marble is observed given that there are 2 blue marbles in the jar is 2/4 or 0.5. In general, the likelihood that a blue marble is observed given that there are x blue marbles in the jar is $x/4$. On the other hand, the likelihood that a red marble is observed given that there are x blue marbles in the jar is 1-$x/4$. Let $b = 1$ denote that a blue marble is drawn, while $b = 0$ indicates that a red marble is drawn. Table 2.1 shows the posterior probabilities given $b = 1$ and Table 2.2 shows the posterior probabilities given $b = 0$. The posterior probabilities were normalized so that the sum was equal to unity. To interpret the right column in Table 2.1, for example, it is seen that by drawing a blue marble, the posterior probability of there being no blue marbles (first row) is now zero. Figure 2.2 shows the posterior probabilities of the number of blue marbles given that a blue marble is drawn (left) and a red marble is drawn (right).

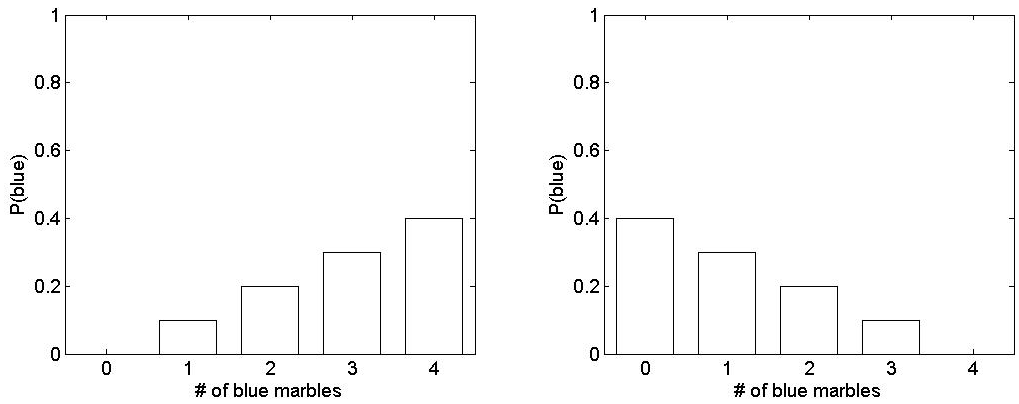

Figure 2.2: Updated posterior probability given an observation; left, blue marble drawn and right, red marble drawn.

If another marble is drawn, the posterior after the first update becomes the prior for the second update and so on. Table 2.3 shows the posterior probability after two observations, where the first is blue and the second is red. The sequence of observation does not matter; the posterior probability would be identical after multiple observations regardless of the order in which they occurred. In addition, multiple observations can be used to update the prior in a single calculation. The posterior is equal to the product of the prior and the likelihood for all observations as shown in Eq. 2.2; note that the normalizing constant is not shown. The observations, b_1, b_2, ..., b_n, are independent and so Eq. 2.2 holds; the equation would not be true for draws without replacement since subsequent observations are not independent of each other.

$$P(blue|observationsb_1, b_2, ...b_n) = \frac{\prod_{i=1}^{n} P(observationb_i|blue)P(blue)}{P(observationb_1, b_2, ...b_n)} \tag{2.2}$$

where b_1, b_2, ..., b_n are the color observations from drawn marbles and n is the number of observations. Figure 2.3 shows the updated posterior probability for different numbers of observations assuming all observed marbles are blue. As the number of consecutive blue marble observations increases, there is more and more data to

Table 2.3: Posterior probability given $b = 1$ followed by $b = 0$

x	Prior	Likelihood ($b = 0$)	Posterior (non-normalized)	Posterior (normalized)
0	0	1	0.2	0
1	0.1	0.75	0.075	0.3
2	0.2	0.5	0.1	0.4
3	0.2	0.25	0.075	0.3
4	0.4	0	0	0
		Σ	0.25	1

support that all the marbles in the jar are blue (see Figure 2.3). When n was very large (>30), the probability that all the marbles in the jar are blue is approximately equal to 1, since there is an overwhelming amount of data to support the belief that all marbles in the jar are blue. Figure 2.4 shows the updated posterior probability for different numbers of observations assuming that 50% of the observed marbles are blue. Bayesian inference makes logical sense for any size of experiments as it combines prior knowledge with observations.

2.2 Decision

In Section 2.1, the Bayesian inference method to update the probability of the number of blue marbles in the jar was demonstrated. It was shown that the Bayesian inference method makes as much sense for no data as for an overwhelming amount. In this section, the situation is framed in a decision setting where a gambler has to guess the number of blue marbles in the jar based on a profit function. The profit function associated with the jar is defined as follows:

$$profit = 500 - 125 \times (B_e - B_a)^2 \tag{2.3}$$

where B_e is the player's guess of the number of blue marbles in the jar and B_a is the actual number of blue marbles in the jar. If the player guesses the number of blue

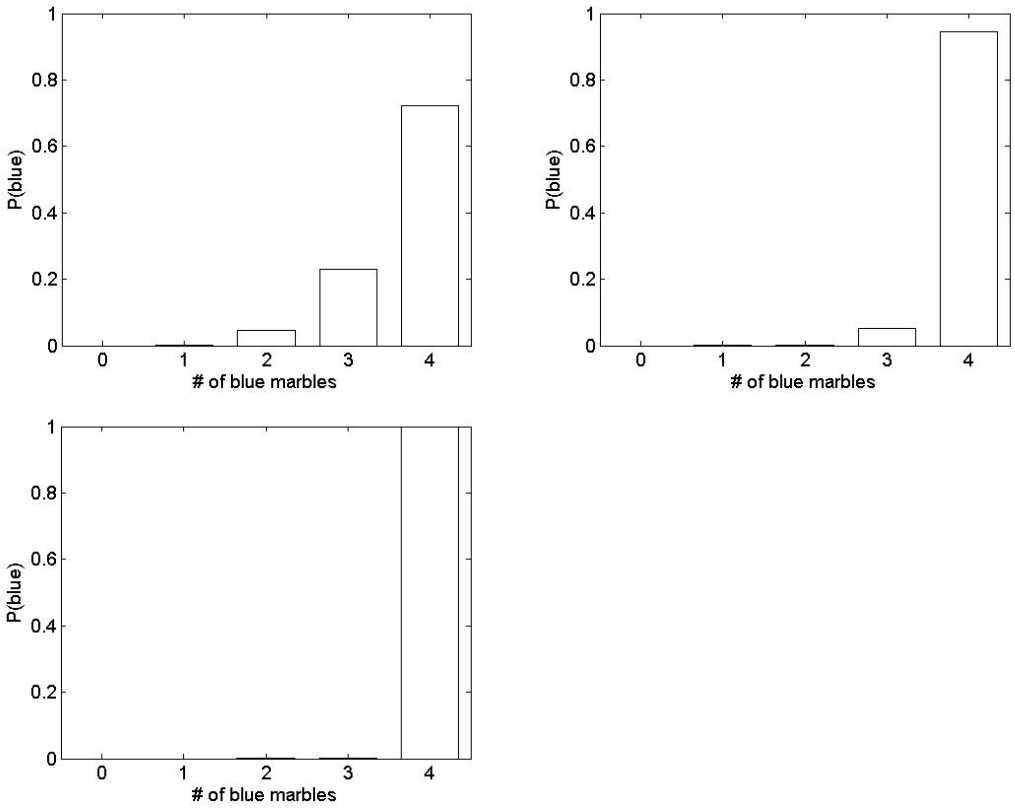

Figure 2.3: Updated posterior probability; four consecutive blue marbles drawn (top left), 10 consecutive blue draws (top right), and 30 consecutive blue draws (bottom left).

marbles correctly, the profit is \$500. If the guess is off by one, the profit is \$375. For a difference of two, the player would break even; higher differences would mean that the player loses money. The profit for different values of (B_e - B_a) is listed in Table 2.4.

The first decision the player must face is whether to enter the gamble or not. It is assumed for the purposes of this exercise that the player is risk neutral, which implies that he/she would play if the expected profit was greater than zero. As a first step towards making the decision to play, an influence diagram, which provides a graphical representation of a decision situation and the corresponding uncertainties, was developed as shown in Figure 2.5. The objective function is to maximize profit which is represented as a value node. The uncertainty node is B_a and the decision

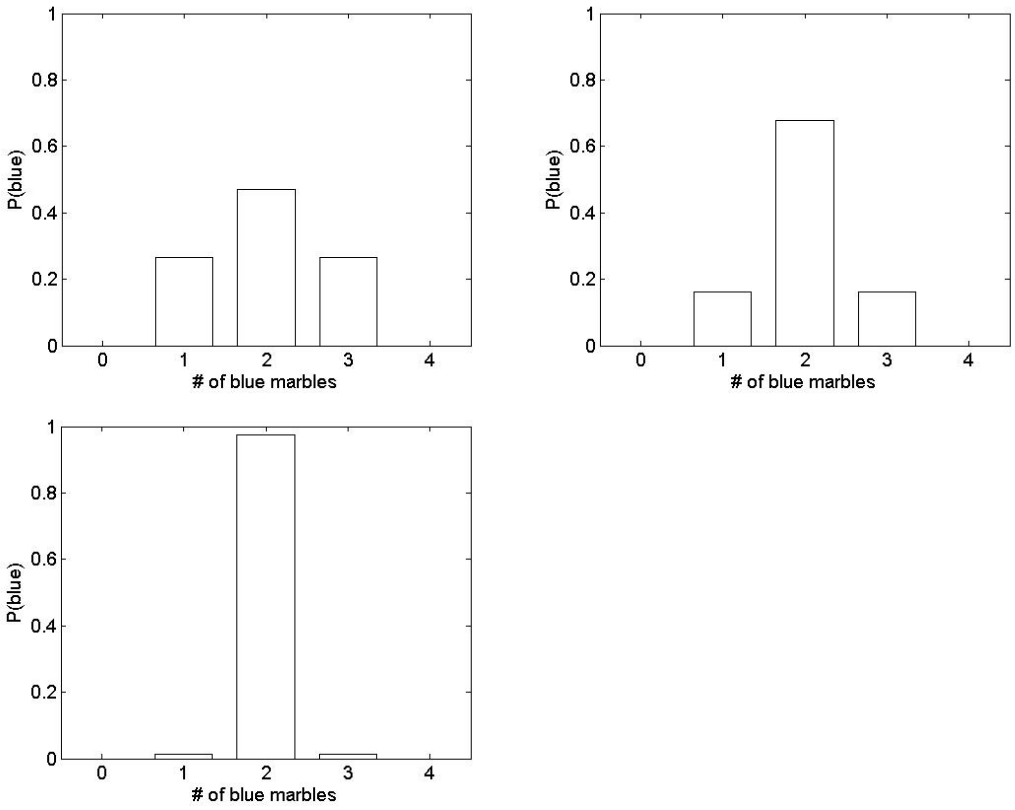

Figure 2.4: Updated posterior probability; two blue draws out of four (top left), five blue draws out of 10 (top right), and 15 blue draws out of 30 (bottom left).

node is B_e. The arrows from B_a and B_e nodes imply that the profit value is relevant to the values of B_a and B_e. There is uncertainty in the profit as a result of the uncertainty in the actual number of blue marbles in the jar. The double hexagon on the profit node denotes that the profit is no longer an uncertainty if the values of B_a and B_e are known with certainty.

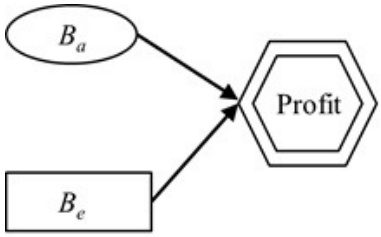

Figure 2.5: Influence diagram for the decision problem.

The data in the uncertain nodes can be represented by distribution trees. The

Table 2.4: Profit for different values of (B_e - B_a).

B_e - B_a	Profit ($)
0	500
1	375
2	0
3	-625
4	-1500

potential outcomes associated with each uncertainty are described using probabilities in a distribution tree. The player has five decision alternatives ($B_e = 0$, 1, 2, 3, or 4). For each alternative, there are five possible outcomes ($B_a = 0$, 1, 2, 3, or 4). Each value of B_e has an expected profit value associated with it given by the sum of the product of the probability of each possible value of B_a and the profit associated with each of the given alternatives. The probability of each outcome was assigned to be 0.2 by the player before any observations; recall that this is the uniform/non-informative prior probability. The expected profit for each alternative was calculated as:

$$E(profit) = \sum_{i=1}^{n} P(B_a = i) \times profit_{(B_a=i)} \tag{2.4}$$

To illustrate, the expected profit for $B_e = 0$ was calculated as:

$$E(profit)_{(B_e=0)} = \$(0.2\times 500+0.2\times 375+0.2\times 0+0.2\times -625+0.2\times -1500) = -\$250 \tag{2.5}$$

Figure 2.6 shows the distribution tree for the decision alternatives. Table 2.5 lists the expected profit for all the alternatives. The expected profit was maximum for $B_e = 2$ and the value was \$250. Therefore, the player would be willing to enter the gamble and the guess is $B_e = 2$. The guess is based on the prior probability assigned by the player to each outcome.

Assume that the player observed a blue marble drawn. The player updates the

Table 2.5: Expected profit for decision alternatives.

B_e - B_a	Profit ($)
0	-250
1	125
2	250
3	125
4	-250

probability of each outcome based on the observation using Bayes' rule as shown in Section 2.1. The updated probabilities (see Table 2.1) were used to calculate the expected profit for all the decision alternatives. To illustrate, the expected profit for $B_e = 0$ after a blue marble observation was calculated as:

$$\begin{aligned} E(profit|b=1)_{(B_e=0)} &= \$(0 \times 500 + 0.1 \times 375 + \\ &\quad 0.2 \times 0 + 0.3 \times -625 + 0.4 \times -1500) = -\$750 \end{aligned}$$

The expected profit was calculated for all the decision alternatives given a blue marble observation; see Table 2.6. The expected profit was maximum for $B_e = 3$ and the value was \$375. Therefore, based on the observation of the blue marble, the player guess is $B_e = 3$ with an expected profit of \$375. Similarly, if the marble drawn was red, the expected profit for $B_e = 0$ was calculated as (see Table 2.2 for posterior probabilities):

$$\begin{aligned} E(profit|b=0)_{(B_e=0)} &= \$(0.4 \times 500 + 0.3 \times 375 + \\ &\quad 0.2 \times 0 + 0.1 \times -625 + 0 \times -1500) = \$250 \end{aligned}$$

Table 2.7 lists the expected profit for the decision alternatives after a red marble observation. In that case, the player guess is $B_e = 1$ with an expected profit of \$375. Figure 2.7 shows the distribution tree given a blue marble observation (left) and red

Table 2.6: Expected profit for alternatives given a blue marble observation.

B_e - B_a	Profit ($)
0	-750
1	-125
2	250
3	375
4	250

Table 2.7: Expected profit for alternatives given a red marble observation.

B_e - B_a	Profit ($)
0	250
1	375
2	250
3	-125
4	-750

marble observation (right). With each succeeding observation, the player updates the probabilities using Bayes' rule and determines his/her guess based on the maximum expected profit among all alternatives.

2.3 Experimentation

In this section, observation possibilities are evaluated for the case where the number of observations must be decided *a priori* and for the case where observations follow sequentially and can be stopped at any point. The player is given an opportunity to purchase the right to observe draws (color of the marble) before submitting a guess. If the player chooses to purchase any observations, it would cost him/her $25 plus $10 per observation. This means that the first observation would cost $35; all subsequent observations would be an additional $10. As shown in Section 2.1, using the observations, the player updates the probabilities of the number of blue marbles and thus increases his/her expected profit. Recall that with no observations, the player's expected profit was $250. However, after 1 observation (either blue or

red), the expected profit increased to $375. Therefore, it is profitable for the player to purchase some observations; however, purchasing too many observations would not be worthwhile since each observation would provide an additional cost and reduce expected profit. The question the player has to answer is: "How many should I purchase?"

Decision analysis combined with Bayesian inference enables a dollar value to be placed on the information gained from an experiment prior to performing it. An experiment is only worthwhile if the value of additional information exceeds the cost of performing that experiment. The value of information (VOI) is defined as the difference between expected profit after observation and expected profit before observation. Note that VOI is calculated before the observation in order to decide whether to purchase the observation (i.e., perform the test) or not [16].

$$VOI = E(\text{profit after observation}) - E(\text{profit before observation}) \tag{2.6}$$

Recall that in the absence of any observations, the best guess is $B_e = 2$ with an expected profit of $250. The maximum profit possible was $500. Therefore, the most a player can expect to increase his/her profit is $250 for this scenario. This places an upper bound on VOI (also called the value of perfect information or value of clairvoyance). The value of perfect information places an upper bound on any information gathering activity. Any observations are only worthwhile if they cost less than the value of perfect information.

2.3.1 Fixed Size Experimentation

First, consider the case where a player has to commit to a certain number of observations beforehand. The opportunity to observe draws costs less than $250 (value of perfect information) and is therefore worth investigating. Before observing any draws, the player assigned an equal probability to the five outcomes (see Figure 2.1).

From the prior probabilities, the probability of observing a blue marble was calculated from the law of total probability as [18]:

$$\begin{aligned} P(blue) &= P(blue \mid B_a = 0) \times P(B_a = 0) + P(blue \mid B_a = 1) \times P(B_a = 1) \\ &\quad + P(blue \mid B_a = 2) \times P(B_a = 2) + P(blue \mid B_a = 3) \times P(B_a = 3) \\ &\quad + P(blue \mid B_a = 4) \times P(B_a = 4) \\ &= 0 \times 0.2 + 0.25 \times 0.2 + 0.5 \times 0.2 + 0.75 \times 0.2 + 1 \times 0.2 \\ &= 0.5 \end{aligned}$$

The probability of observing a red marble, P(red) was also calculated as 0.5. Only two outcomes are possible, the sum of P($blue$) and P(red) should be equal to unity. Based on the prior probabilities, there is a probability of 0.5 of observing a blue marble. In this case the best decision would be to guess the number of blue marbles to be 3, which would yield an expected profit of \$375. Also, there is a probability of 0.5 of observing a red marble. Here, the best decision would be to guess the number of blue marbles as 1, which would also yield an expected profit of \$375 (see Section 2.2). Therefore, the expected profit after observation was calculated as:

$$\begin{aligned} E(\text{profit after observation}) &= P(blue) \times E(profit \mid \text{blue observation}) \\ &\quad + P(red) \times E(profit \mid \text{red observation}) \\ &= \$375 \end{aligned}$$

The expected profit before observation was \$250. The corresponding VOI for the first test is \$125. The cost of the first observation is \$35. Therefore, the expected increase in profit after the first tests is \$90. After some observations, the marginal increase in VOI would be less than the cost of observation at which point the expected increase in profit (calculated as VOI - cost of observations) will start to decrease. The number

of observations to be purchased should be selected so that the expected increase in profit is maximum. Therefore, at least one observation should be purchased. The calculation is summarized in Figure 2.8.

For the second observation, there are four possible outcomes, (blue, blue), (blue, red), (red, blue) and (red, red). Each outcome has a probability; their sum is unity. To illustrate, the probability of observing a blue marble in the first observation is 0.5. If a blue marble is observed, the prior probabilities can be updated as demonstrated in Section 2.1 (see Table 2.1). The probability of observing a blue marble in the second observation given a blue marble in the first observation was again calculated using the law of total probability. Note that the updated posterior probabilities are used to determine the probability of blue marble in the second observation.

$$\begin{aligned} E(blue|b=1) &= 0 \times 0 + 0.25 \times 0.1 + 0.5 \times 0.2 + 0.75 \times 0.3 + 1 \times 0.4 \\ &= 0.75 \end{aligned}$$

Thus, the joint probability of observing two blue marbles in succession is 0.375. The joint probability can also be determined using the law of total probability for both cases combined as:

$$P(blue, blue) = \sum P(blue, blue \mid blue)P(blue) \tag{2.7}$$

Recall that P($blue$) is the prior probability for number of blue marbles which was equal to 0.2. The joint probability of observing two blue marbles is calculated as:

$$\begin{aligned} P(blue, blue) &= 0^2 \times 0.2 + 0.25^2 \times 0.2 + \\ &\quad 0.5^2 \times 0.2 + 0.75^2 \times 0.2 + 1^2 \times 0.2 \\ &= 0.375 \end{aligned}$$

The maximum expected profit after observing two blue marbles was calculated as $406.25. The procedure was repeated for all possible four outcomes. The calculations are summarized in Figure 2.9.

The expected VOI after two observations is $156.25 and the cost of two observations is $45. Therefore, the net expected increase in profit after two observations is $111.50; it is profitable to purchase at least two observations. The procedure was repeated up to ten observations. After each observation, the expected value of information was calculated as demonstrated. Figure 2.10 shows the VOI, cost of observations, and the difference (VOI-cost of observations) as a function of the number of observations. The maximum increase in expected profit occurs after five observations and is equal to $125.10. For more than five observations, the marginal gain from the observation is less than the cost of the observation. Therefore, the expected increase in profit is maximum after five observations; the optimal number of observations to be purchased is five.

2.4 Sequential Sampling

Second, consider the case where the player is given an option to observe sequential draws and stop purchasing the right to observe whenever he/she wishes. The player does not commit to a fixed number of observations beforehand. Again, the cost is $25 plus $10 per observation.

As calculated in Section 2.2, the expected profit after the first draw is $375 and, therefore, the VOI for the first test is $125 (see Figure 2.11). Thus, the first observation is purchased by the player since the VOI is greater than the cost of observation. In the first observation, it is assumed that the drawn marble is blue. The prior probabilities are updated as shown in Section 2.1 (see Table 2.1). The posterior probabilities are again used to determine the probability of observing a blue marble and a red marble and the expected profit for each (see Figure 2.12). The expected profit for the second observation is calculated as $406.25. The VOI for the second observation is

$31.25. The procedure was repeated after observing the draws each time until the VOI of the next observation was less than $10. This means that the experiment costs more than the expected increases in profit after observing the result. Figure 2.13 shows the VOI as a function of the number of observations assuming all marbles drawn are blue. Note that the VOI is not a strictly monotonic decreasing function; it depends on the observation. Figure 2.14 shows the expected profit for each observation. The expected profit tends to $500, which is the maximum achievable profit.

Another way to approach the problem would be to calculate explicitly the value of the updated probability of a decision alternative in order to no longer require any further observations and, hence, determine the possible observational results required to obtain the desired value of the probability of the outcome. The stopping criteria in this case would be a pre-determined confidence in the decision alternative.

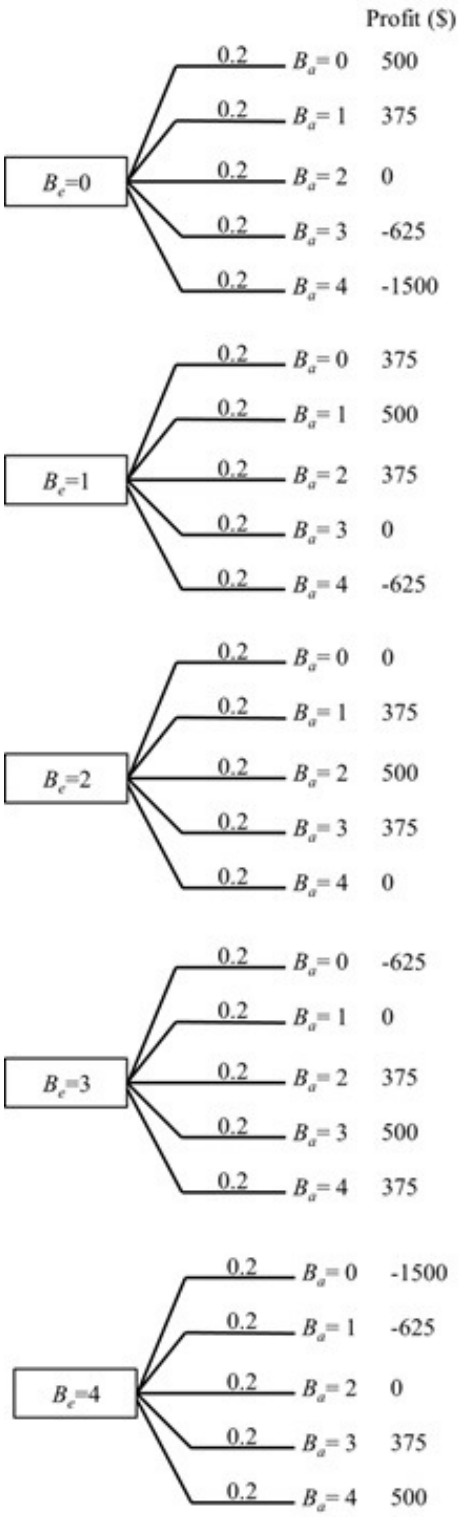

Figure 2.6: Distribution tree for decision alternatives.

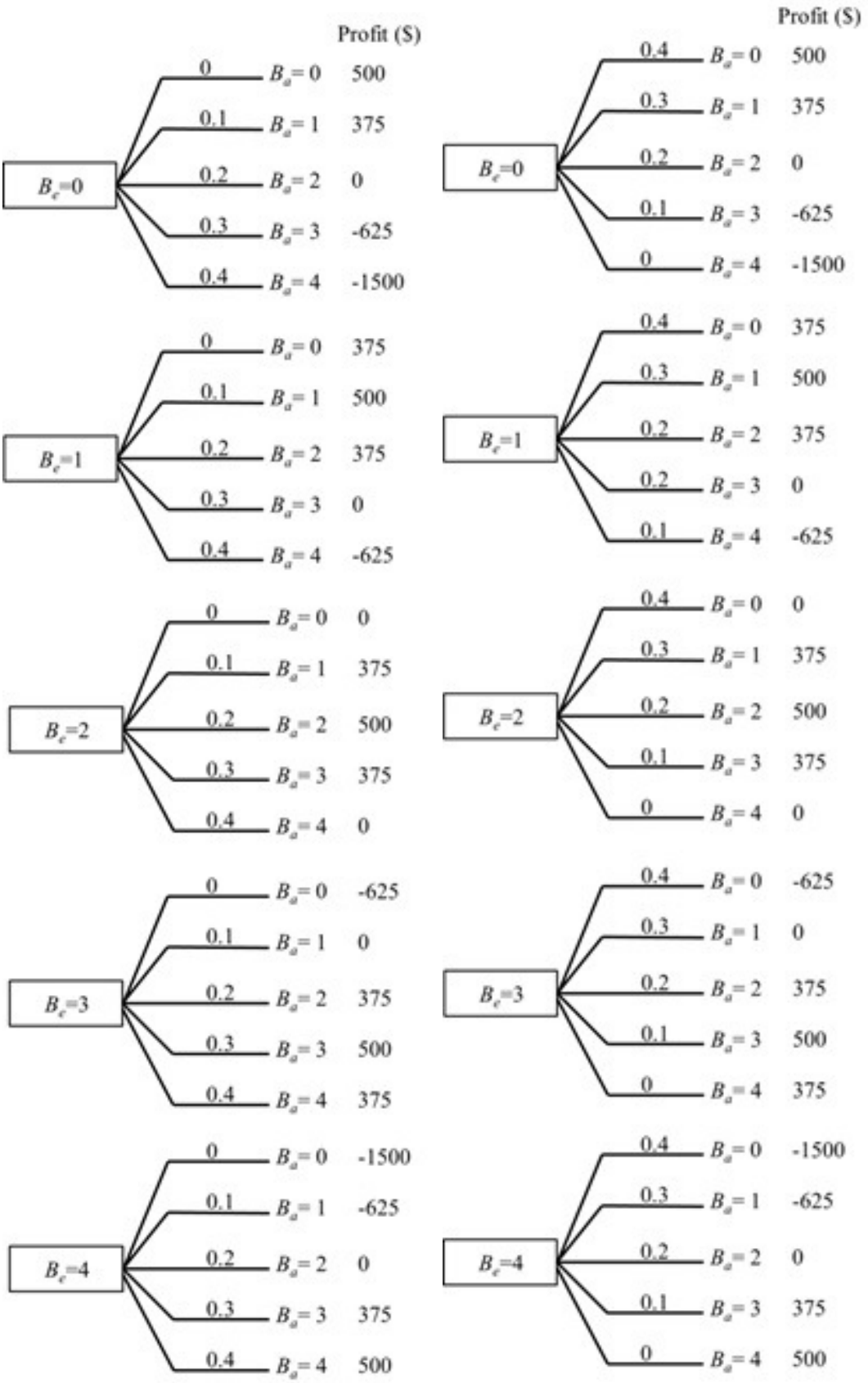

Figure 2.7: Distribution tree for decision alternatives given a blue marble observation (left) and red marble (right).

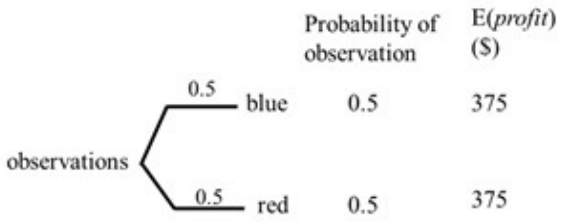

Figure 2.8: Expected profit for the first observation.

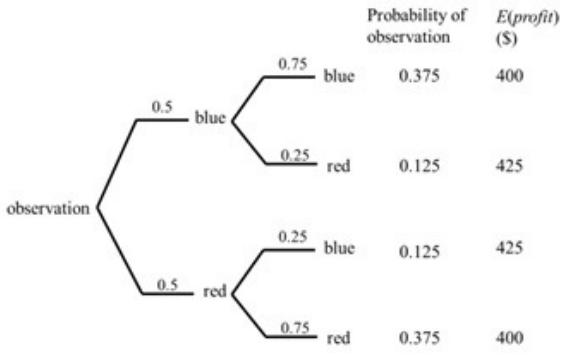

Figure 2.9: Expected profit after second observation

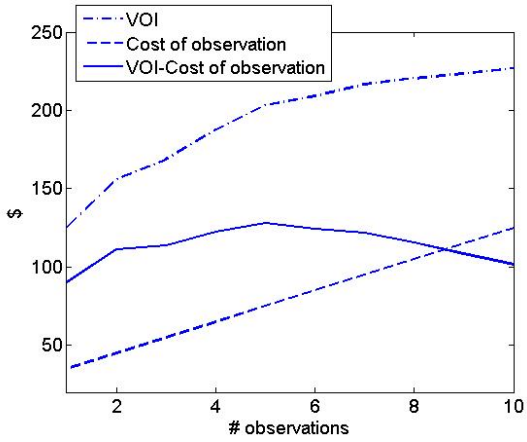

Figure 2.10: Expected increase in profit with number of observations.

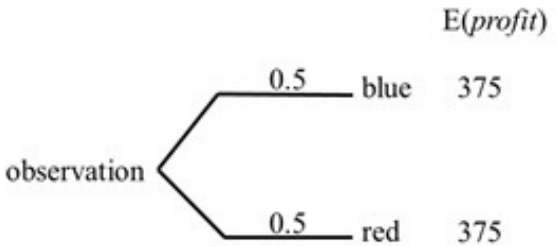

Figure 2.11: VOI as a function of number of observation assuming all the marbles drawn were blue.

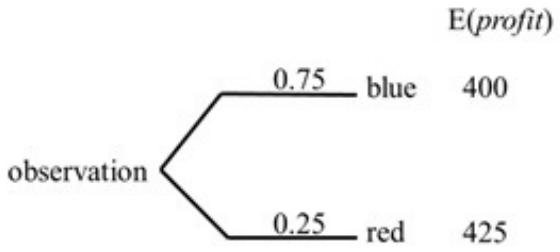

Figure 2.12: VOI as a function of number of observation assuming all the marbles drawn were blue.

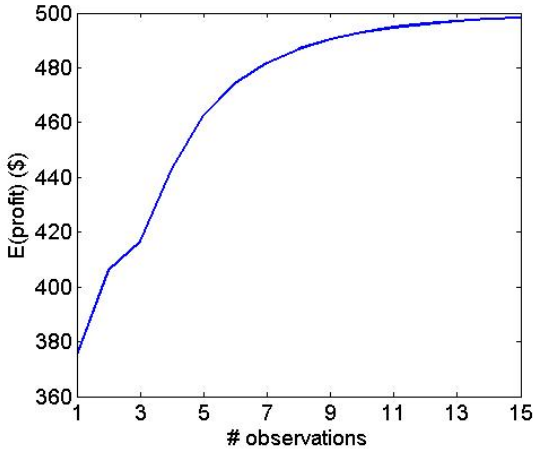

Figure 2.13: VOI as a function of number of observation assuming all the marbles drawn were blue.

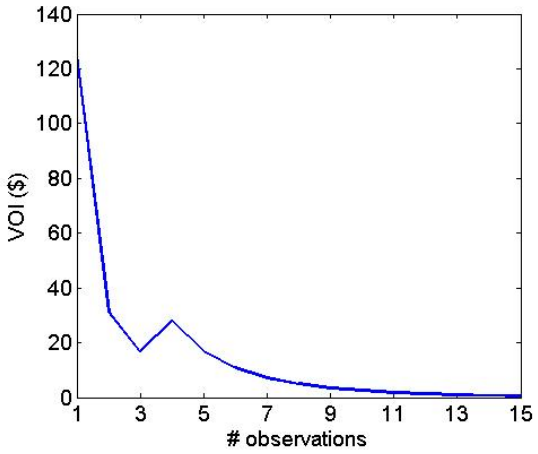

Figure 2.14: Expected profit for every observation assuming all the marbles drawn were blue.

CHAPTER 3: APPLICATION TO MILLING FORCE MODELING

In the modeling of milling operations, a fundamental requirement is the ability to predict the cutting force as a function of cutter angle (or time). Mechanistic force models, that relate the cutting force to the milling parameters using empirical coefficients, are often applied. This chapter describes the application of Bayesian inference to the identification of force coefficients in milling. Mechanistic cutting force coefficients have been traditionally determined by performing a linear regression to the mean force values measured over a range of feed per tooth values. This linear regression method, however, yields a deterministic result for each coefficient and requires testing at several feed per tooth values to obtain a high level of confidence in the regression analysis. Bayesian inference, on the other hand, provides a systematic and formal way of updating beliefs when new information is available while incorporating uncertainty. In this work, mean force data is used to update the prior probability distributions (initial beliefs) of force coefficients using the Metropolis-Hastings algorithm of Markov Chain Monte Carlo approach. Experiments are performed at different radial depths of cut to determine the corresponding force coefficients using both methods and the results are compared.

3.1 Introduction

In metal cutting operations, the cutting force can be modeled using the chip area and empirical constants that depend on the tool-workpiece combination. In milling, the tangential, F_t, and normal, F_n, direction force components can be described using Eqs. 3.1 and 3.2, where b is the chip width (axial depth of cut), h is the instantaneous chip thickness, K_t is the tangential cutting force coefficient, K_{te} is the tangential

edge coefficient, K_n is the normal cutting force coefficient, and K_{ne} is the normal edge coefficient [30].

$$F_t = K_t bh + K_{te} b \tag{3.1}$$

$$F_n = K_n bh + K_{ne} b \tag{3.2}$$

The chip thickness is time-dependent in milling and can be approximated using the feed per tooth, f_t, and time-dependent cutter angle, ϕ, provided the ratio of the feed per tooth to cutter diameter is small [31]. See Eq. 3.3.

$$h = f_t sin(\phi) \tag{3.3}$$

The forces in the x (feed) and y directions, F_x and F_y, are determined by projecting the tangential and normal force components in the x and y directions using the cutter angle as shown in Figure 3.1. See Eqs. 3.4 and 3.5.

$$F_x = K_t b f_t sin(\phi)cos(\phi) + K_{te} b cos(\phi) + K_t b f_t sin^2(\phi) + K_{ne} b sin(\phi) \tag{3.4}$$

$$F_y = K_t b f_t sin^2(\phi) + K_{te} b sin(\phi) - K_n b f_t sin(\phi)cos(\phi) - K_{ne} b cos(\phi) \tag{3.5}$$

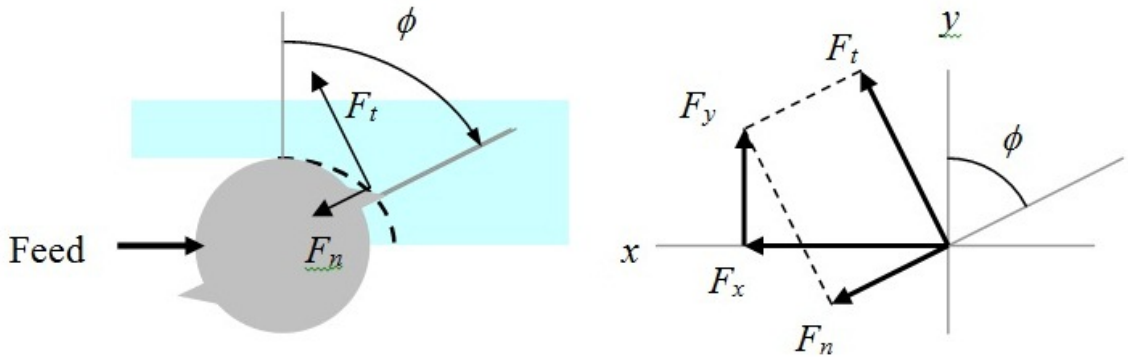

Figure 3.1: Milling force geometry (a 50% radial immersion up milling cut using a cutter with two teeth is depicted).

Expressions for the mean forces in the x and y directions, F_{xm} and F_{ym}, are provided in Eqs. 3.6 and 3.7, where N_t is the number of teeth on the cutter and ϕ_s and ϕ_e are the cut start and exit angles, which are defined by the radial depth of cut [30].

$$F_{xm} = \left[\frac{N_t b f_t}{8\pi}(-K_t cos(2\phi) + K_n(2\phi - sin(2\phi))) + \frac{N_t b}{2\pi}(K_{te} sin(\phi) - K_{ne} cos(\phi))\right]_{\phi_s}^{\phi_e} \tag{3.6}$$

$$F_{ym} = \left[\frac{N_t b f_t}{8\pi}(K_t(2\phi - sin(2\phi)) + K_n cos(2\phi) - \frac{N_t b}{2\pi}(K_{te} cos(\phi) - K_{ne} sin(\phi))\right]_{\phi_s}^{\phi_e} \tag{3.7}$$

In Eqs. 3.6 and 3.7 average force expressions, the first term, which is a function of the feed per tooth, gives the slope of the linear regression to the average force values that correspond to the selected feed per tooth values. The second term, which does not include the feed per tooth, is the intercept of the linear regression. By rearranging Eqs. 3.6 and 3.7, the four force coefficients are determined using Eqs. 3.8- 3.11, where $a_{1,x}$ and $a_{1,y}$ are the slopes of the linear regressions to the x and y direction average force data, and $a_{0,x}$ and $a_{0,y}$ are the intercepts.

$$K_t = \frac{8\pi}{N_t b}\frac{a_{1,y}(2\phi_e - 2\phi_s + sin(2\phi_s) - sin(2\phi_e)) + a_{1,x}(cos(2\phi_s) - cos(2\phi_e))}{(2\phi_e - 2\phi_s + sin(2\phi_s) - sin(2\phi_e))^2 + (cos(2\phi_e) - cos(2\phi_s))^2} \tag{3.8}$$

$$K_t = \frac{8\pi}{N_t b}\frac{a_{1,y}(cos(2\phi_e) - cos(2\phi_s)) + a_{1,x}(2\phi_e - 2\phi_s + sin(2\phi_s) - sin(2\phi_e))}{(2\phi_e - 2\phi_s + sin(2\phi_s) - sin(2\phi_e))^2 + (cos(2\phi_e) - cos(2\phi_s))^2} \tag{3.9}$$

$$K_{te} = \frac{\pi}{N_t b}\frac{a_{0,x}(sin(\phi_e) - sin(\phi_s)) + a_{0,y}(cos(phi_e) - cos(\phi_s))}{(1 - cos(\phi_e - \phi_s)} \tag{3.10}$$

$$K_{ne} = \frac{-\pi}{N_t b}\frac{a_{0,x}(cos(\phi_e) - cos(\phi_s)) + a_{0,y}(sin(phi_e) - sin(\phi_s))}{(1 - cos(\phi_e - \phi_s)} \tag{3.11}$$

3.2 Bayesian Inference

Bayesian inference is applied for force coefficient determination here. Bayesian inference models are used to update beliefs about an uncertain variable when new information becomes available. For the case of updating the four force coefficients in Eqs. 3.8- 3.11 using experimental force data, Bayes' rule is written as:

$$P(K_t, K_n, K_{te}, K_{ne} \mid F_{xm}, F_{ym}) = \frac{P(F_{xm}, F_{ym} \mid K_t, K_n, K_{te}, K_{ne}) P(K_t, K_n, K_{te}, K_{ne})}{P(F_{xm}, F_{ym})} \tag{3.12}$$

where $\mathrm{P}(K_t,\ K_n,\ K_{te},\ K_{ne} \mid F_{xm},\ F_{ym})$ is the posterior distribution of the force coefficients given measured values of the mean forces in the x and y directions, F_{xm} and F_{ym}, $\mathrm{P}(K_t,\ K_n,\ K_{te},\ K_{ne})$ is the prior distribution of the force coefficients, and $\mathrm{P}(F_{xm},\ F_{ym} \mid K_t,\ K_n,\ K_{te},\ K_{ne})$ is the likelihood of obtaining the measured mean force values given specified values of the force coefficients. The posterior (i.e., the new belief after updating) is proportional to the prior multiplied by the likelihood. For multiple measurements, Bayes' rule can incorporate all data in a single calculation. The likelihood functions for each measurement are multiplied together to obtain a total likelihood function. The posterior pdf is calculated by multiplying the prior and the total likelihood function. Note that the posterior distributions must be normalized so that a unit volume under the pdf is obtained; this is the purpose of the denominator in Eq. 3.12.

3.3 Markov Chain Monte Carlo (MCMC) Method

The Markov chain Monte Carlo (MCMC) method is a strategy used to draw samples, x_i, from a random (known) distribution, where i is the sample (or iteration) number. The distribution of interest is referred to as a target distribution and is denoted as $\mathrm{p}(x)$. Using the MCMC method, samples are generated from the state space, X, using a Markov chain mechanism [32]. The Metropolis-Hastings (MH)

algorithm is the most widely used MCMC method [33, 34]. In the MH algorithm, a candidate sample, x^*, is drawn from a proposal distribution, q(x). It is selected given the current value of x according to q($x^* \mid x_i$). The candidate sample is either accepted or rejected depending on an acceptance ratio, A. The acceptance ratio is calculated as shown in Eq. 3.13. At each iteration, the Markov chain moves to x^* if the sample is accepted. Otherwise, the chain remains at the current value of x. The MH algorithm is completed over N-1 iterations as follows.

- Initialize the starting point x_0.
- For $i = 0$ to $i = N$-1 iterations, complete the following four steps:
  - randomly sample x^* from the proposal pdf q($x^* \mid x_i$).
  - randomly sample u from a uniform distribution of values between 0 and 1, U(0, 1).
  - compute the acceptance ratio, A.
  - if $u < A$, then set the new value equal to the new sample, $x_{i+1} = x^*$; otherwise, the value remains unchanged $x_{i+1} = x_i$.

$$A = min\left(1, \frac{p(x^i)q(x^i \mid x*)}{p(x^i)q(x^* \mid x^i)}\right) \tag{3.13}$$

3.3.1 Algorithm Demonstration

To illustrate the algorithm, consider a target pdf described by the bimodal pdf in Eq. 3.14 [32]. Note that the normalization constant of the target pdf does not need to be known.

For this example, a normal proposal distribution, q(x), was chosen with a mean of x_i and a standard deviation of 10, i.e., q(x) = N(x^i,10). The starting point of the chain, x_0, was selected to be zero. At each iteration, i, the following steps were completed. First, a candidate sample, x^*, was randomly drawn from N(x^i, 10). The

candidate sample was drawn given the current value of the chain, q($x^* \mid x_i$). In other words, the proposal distribution is conditioned on the current value of the chain. To illustrate, consider the first iteration. The chain starting point is $x^0 = 0$. Therefore, x^* is a random sample drawn from N(0, 10). Assume the randomly selected value is $x^* = 2$ and it is accepted as x^1. In the second iteration, the random sample is drawn from N(2, 10). If the sample is 12 and it is rejected, then the current value of x^2 remains at 2. In the third iteration the random sample will again be drawn from N(2, 10).

In the second step, p(x^*) and p(x^1) were calculated using Eq. 3.14 for the target distribution. Third, q($x^* \mid x_i$) and q($x_i \mid x^*$) were calculated, where q($x^* \mid x_i$) was the pdf value of the normal proposal distribution at x^* given a mean equal to x_i and a standard deviation of 10. Similarly, q($x_i \mid x^*$) was the pdf value of the normal proposal distribution at x^i given a mean of x^* with a standard deviation of 10. Fourth, the acceptance ratio, A, was calculated. Because normal distributions were used, the equality q($x^* \mid x_i$) = q($x_i \mid x^*$) holds and the acceptance ratio simplified to as shown in Eq. 3.15.

$$p(x) \propto 0.3e^{-0.2x^2} + 0.7e^{-0.2(x-10)^2} \tag{3.14}$$

$$A = min\left(1, \frac{p(x^*)}{p(x^i)}\right) \tag{3.15}$$

Fifth, A was compared to a random sample, u, drawn from a uniform distribution with a range from 0 to 1. Finally, if u was less than A, then the candidate sample was accepted so that $x^{i+1} = x^*$. Otherwise, it was rejected and $x^{i+1} = x^i$. These steps were repeated for N-1 iterations to obtain N samples of x from the target pdf described by Eq. 3.14.

The MH algorithm was carried out for $1{\times}10^4$ iterations. Figure 3.2 shows the histogram of the 10000 samples and target distribution from Eq. 3.14 (left) and x values for each iteration (right). It is observed that the samples approximate the

target pdf quite well. Note that the histogram and target distribution were normalized to obtain a unit area.

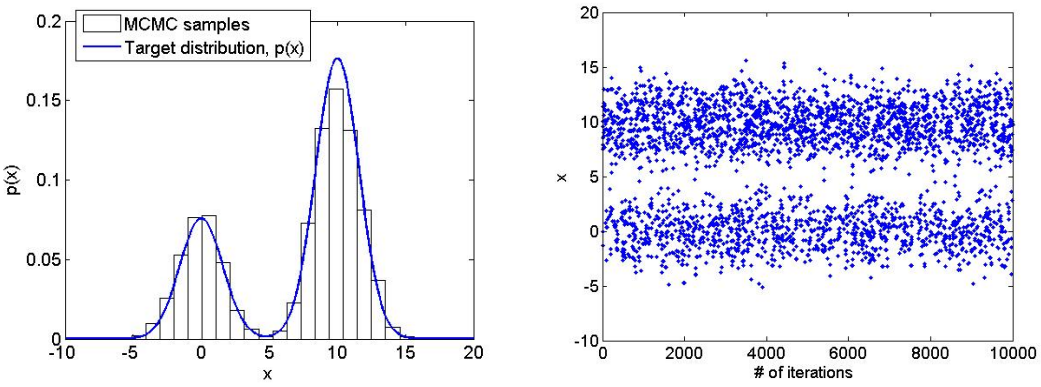

Figure 3.2: Histogram of MCMC samples and target distribution (left) and x values for each iteration (right).

Although the MH algorithm is effective for sampling from any target distribution, there are a number of considerations in its application. The success of the algorithm depends on the choice of proposal distribution. In theory, the chain should converge to the stationary target distribution for any proposal distribution [35]. However, the proposal distribution may affect the convergence and mixing of the chain. In general, the proposal distribution may be selected so that the sampling is convenient. For a normal proposal distribution (that was chosen in this example), the choice of the standard deviation can also affect the results. A larger standard deviation causes greater jumps around the current value. Thus, the candidate sample has a higher probability of being rejected, which yields $x_{i+1} = x_i$. On the other hand, while a smaller variance will tend to accept a higher number of random samples, it results in slower convergence of the chain.

In practice, the initial iterations are typically discarded and the chain subsequently settles to a stationary distribution. This is referred to as the burn-in time of the chain. A practical way to evaluate convergence to the chain's stationary distribution is by observing the traces and histograms of the variables (e.g., see Figure 3.2). The

number of iterations should be large enough to ensure convergence to the statistical moments of the target distribution. The starting value of the chain has no effect for a large number of iterations [35]. The convergence to the true statistical moments can be observed by repeating the algorithm using different starting values and varying the number of iterations. Despite these potential limitations, the MH algorithm (for MCMC) works well and can effectively be used to draw samples from multivariate distributions.

3.3.2 Application to Bayesian Inference

This section describes the application of MCMC to Bayesian inference. As stated, Bayesian inference provides a formal way to update beliefs about the posterior distribution (the normalized product of the prior and the likelihood functions) using experimental results. In the case of updating force coefficients (Eq. 3.12), the prior is a joint pdf of the force coefficients, K_t, K_n, K_{te}, and K_{ne}. As a result, the posterior is also a joint pdf of the force coefficients. In Bayesian inference, the MCMC technique can be used to sample from multivariate posterior distributions. The single-component MH algorithm facilitates sampling from multivariate distributions without sensitivity to the number of variables. The joint posterior pdf is the target pdf for MCMC. The posterior, or target, pdf is the product of the prior and likelihood density functions. Note that the normalizing constant of the posterior pdf is not required for sampling.

The MH algorithm was detailed for a single variable in Section 3.3.1. To sample from a joint pdf, the algorithm samples one variable at a time and then proceeds sequentially to sample the remaining variables. The sequence of variable sampling does not influence the convergence of the algorithm. To illustrate, consider a joint target pdf of n variables: x_1, x_2, x_3, $\cdots$ x_n. To begin, the starting value for all the variables is initialized, $[x_1^0, x_2^0, x_3^0, \cdots x_n^0]$. Let the algorithm proceed in the order, $x_1 \rightarrow x_2 \rightarrow x_3 \rightarrow \cdots x_n$. The sampling for each variable is carried out using a univariate

proposal distribution for that variable. The proposal distribution for each variable can be different or the same. Since the algorithm proceeds one variable at a time, the target and the proposal pdf for each variable is conditioned on the current values of the other variables. For example, consider a candidate sample, x_1^*, drawn from the univariate proposal distribution for x_1. The candidate sample from the joint pdf is then $[x_1^*,\ x_2^0,\ x_3^0,\ \cdots\ x_n^0]$. The candidate sample, x_1^*, is either accepted or rejected given the current values of $x_2,\ x_3,\ \cdots\ x_n$. Thus, the target pdf values of x_1^* and x_1^0 are conditional on the current values of the other variables, $x_2^0,\ x_3^0,\ \cdots\ x_n^0$ and are denoted as $\mathrm{p}(x_1^* \mid x_1^0,\ x_2^0,\ \cdots\ x_n^0)$ and $\mathrm{p}(x_1^0 \mid x_1^*,\ x_2^0,\ \cdots\ x_n^0)$. The proposal univariate pdfs are also conditional on the current values of the chain and are denoted as $\mathrm{q}(x_1^* \mid x_1^0,\ x_2^0,\ \cdots\ x_n^0)$ and $\mathrm{q}(x_1 \mid x_1^*,\ x_2^0,\ \cdots\ x_n^0)$ for x_1^* and x_1, respectively. To summarize, the chain either stays at the current point, $[x_1^0,\ x_2^0,\ x_3^0,\ \cdots\ x_n^0]$ or moves to a neighboring point, $[x_1^*,\ x_2^0,\ x_3^0,\ \cdots\ x_n^0]$, which differs only in one component of the current state (x_1 in this case). The procedure is repeated for all variables in each iteration. The acceptance ratio is:

$$A = min\left(1, \frac{p(x_1^* \mid x_2, x_3, \cdots, x_n)q(x_1^i \mid x_1^**, x_2, x_3, \cdots, x_n)}{p(x_1^i \mid x_2, x_3, \cdots, x_n)q(x_1^* \mid x_1^i, x_2, x_3, \cdots, x_n)}\right) \tag{3.16}$$

where the value of each of the four joint pdfs must each be calculated. The value of A is compared to a random sample, u, from a uniform distribution with a range from 0 to 1 and x_1^* is either accepted or rejected to obtain x_1^{i+1}. The algorithm is repeated using the updated values of each variable continually for the next variable. Thus, x_2^{i+1} is determined using $x_1^{i+1},\ x_2^i,\cdots\ x_n^i$, x_3^{i+1} is determined using $x_1^{i+1},\ x_2^{i+1},$ $\cdots\ x_n^i$, and so on for n variables. The algorithm therefore moves by a small step in the joint pdf by sampling a single variable at a time. A single iteration updates all the variables. The algorithm is then carried out for N iterations to obtain samples from the joint target pdf. An alternative method is to sample from a joint proposal pdf and

Table 3.1: Time-domain simulation parameters.

Parameter	Value
Tool diameter (mm)	19.05
Radial depth (mm)	4.76
Axial depth (mm)	3.00
Spindle speed (rpm)	5000
Feed per tooth (mm/tooth)	0.03, 0.04, 0.05, 0.06 and 0.07
Number of teeth	1
Helix angle (deg)	0
Tangential coefficient (N/mm^2)	2200
Normal coefficient (N/mm^2)	1200
Tangential edge coefficient (N/mm)	50
Normal edge coefficient (N/mm)	50

accept or reject it using the MH algorithm. However, it is much simpler to sample from univariate proposal distributions for each variable and is computationally less expensive.

3.4 Bayesian Updating using the Markov Chain Monte Carlo Method

In this section, MCMC method for Bayesian updating of force coefficients is demonstrated using a numerical example. The effects of the prior and likelihood uncertainties are also evaluated. A milling time-domain simulation was used to obtain the x and y direction mean force values [30]. The tool-material combination was assumed to be a coated carbide tool and 1018 steel. The objective of the simulation was to validate the MCMC method by comparing its solution to the known force coefficients used to define the measured data via the simulation. The parameters used in the down milling simulation are listed in Table 3.1. The simulation was exercised at different feed per tooth values and the mean forces were recorded; see Table 3.2. The mean values listed in Table 3.2 were treated as experimental results and used to update the force coefficients' prior distributions using the MCMC method for Bayesian inference.

Table 3.2: Mean force values obtained from the time-domain simulation.

f_t (mm/tooth)	F_{xm} (N)	F_{ym} (N)
0.03	-15.40	49.01
0.04	-17.58	54.40
0.05	-19.76	59.80
0.06	-21.94	65.19
0.07	-24.12	70.59

As described in Section 3.3.2, a single-component MH algorithm was used to sample from the joint posterior pdf of the force coefficients, K_t, K_n, K_{te}, and K_{ne}. The posterior joint pdf was the target pdf for the MH algorithm. For this analysis, the prior distribution of force coefficients was assumed to be a joint uniform distribution, i.e., it was equally likely to obtain any value within the specified range. The force coefficients were assumed to be independent for the prior. The marginal prior pdfs of the force coefficients were specified as: K_t (N/mm^2) = U(0, 3000), K_n (N/mm^2) = U(0, 3000), K_{te} (N/mm) = U(0, 100), and K_{ne} (N/mm) = U(0, 100), where U represents a uniform distribution and the parenthetical terms indicated the lower and upper values of the range. As noted, this distribution represents a less informative prior than a normal distribution with a mean and standard deviation. The effect of different types of priors on the posterior distributions is discussed in Section 3.4.3.

The single-component MH algorithm proceeds as follows. First, the starting point for the Markov chain, $x^0 = [K_t^0\ K_n^0\ K_{te}^0\ K_{ne}^0]$ was selected to be the midpoints of the uniform K_t, K_n, K_{te}, and K_{ne} distributions, x^0 = [1500 1500 25 25]. The sampling was completed one coefficient at a time in the order K_t, K_n, K_{te}, and K_{ne}. A candidate sample, K_t^*, was drawn from the proposal distribution of K_t. The proposal distribution for each coefficient was selected to be normal. The posterior, or target, pdf values, of each force coefficient were conditional on the values of the other coefficients. The posterior pdf for K_t, denoted as p($K_t^0 \mid K_n^0\ K_{te}^0\ K_{ne}^0$), was the product of the prior and likelihood functions. The prior value for any coefficient was determined

from the marginal prior distributions of each coefficient, which were selected to be uniform. The mean force values were calculated using the current state of the chain, $[K_t^0 \mid K_n^0\ K_{te}^0\ K_{ne}^0]$, together with Eqs. 3.6 and 3.7 for the specified cut geometry. Because there is inherent uncertainty in milling forces, the mean force values calculated using the current state of chain and Eqs. 3.6 and 3.7 were assumed to be normally distributed with a standard deviation of 1 N, which was based on the user's belief regarding experimental uncertainty in measured force values (this value could also be specified as a percent of the nominal value, for example). The effect of the standard deviation on the posterior pdf is discussed in Section 3.4.2. This gave a pdf for both the x and y direction mean forces calculated using the current state of the chain. The likelihood for the x and y directions was the value of each pdf for the experimental mean forces (from the time-domain simulation). Therefore, the likelihood described how likely it was to obtain the experimental mean forces given the current state of the chain. For multiple measurement results, the total likelihood pdf was the product of the likelihood pdfs for all measurements. The same procedure was followed to determine the posterior pdf value for K_t^*, $\mathrm{p}(K_t^* \mid K_n^0\ K_{te}^0\ K_{ne}^0)$. Since the proposal distribution was normal, the acceptance ratio was calculated using Eq. 3.17.

$$A = min\left(1, \frac{p(K_t^* \mid K_n, K_{te}, K_{ne})}{p(K_t^i \mid K_n, K_{te}, K_{ne})}\right) \tag{3.17}$$

The acceptance ratio was compared with a random sample, u, from a uniform distribution (with a range from 0 to 1) to assign the value of K_t^1 to be either K_t^* or K_t^0. To update the four force coefficients, K_t, K_n, K_{te}, and K_{ne}, the algorithm considered one coefficient at a time and then proceeded to sequentially update the remaining coefficients. The updated values for each coefficient were used continually for updating the next coefficient. For the order $K_t \rightarrow K_n \rightarrow K_{te} \rightarrow K_{ne}$, K_t^1 was used to update K_n^0. Next, K_t^1 and K_n^1 were used for K_{te}^0. Finally, K_t^1, K_n^1, and K_{te}^1 were used for

K_{ne}^0. A single iteration provided samples for all the force coefficients. This sequence was repeated for N-1 iterations giving N samples from the joint posterior pdf of the coefficients. Note that the standard deviations of the proposal distributions affect the convergence of the chain. The standard deviations of the force coefficients, K_t, K_n, K_{te}, and K_{ne} were 600 N/mm^2, 600 N/mm^2, 33 N/mm and 33 N/mm respectively. As a rule of thumb, the standard deviation should be large enough to draw adequate samples to explore the domain. However, a very large standard deviation leads to a higher probability of candidate samples being rejected.

3.4.1 Results

The MH algorithm was exercised for 1×10^5 iterations. Figure 3.3 shows the sample traces of the force coefficients for all iterations. It is seen that there is a rapid convergence to the true values for all coefficients. The initial burn-in time was selected as 1×10^3 iterations. Figure 3.4 shows a comparison between the prior marginal pdfs and posterior sample histograms of the force coefficients. The histograms represent the marginal posterior pdfs of the force coefficients and were normalized to obtain a unit area. The distributions in the force coefficients is due to the uncertainty in the mean force values. MCMC gives samples from the joint posterior pdf of the force coefficients, K_t, K_n, K_{te}, and K_{ne}. Since the prior was assumed to be a uniform distribution and the likelihood was normal, the posterior joint distribution was also a joint normal distribution. The mean, μ, and standard deviation, σ, values for the four force coefficient posterior marginal pdfs are listed in Table 3.3; the coefficient mean values show good agreement with the true values. Note that the coefficient distributions are not independent; the correlation coefficients between the force coefficients are listed in Table 3.4. Although the convergence to the true values as a function of number of iterations can be evaluated, 1×10^5 samples was found to be adequate to ensure convergence for this study. Table 3.4 shows that the cutting force coefficients, K_t and K_n, as well as the edge coefficients, K_{te}, K_{ne}, have a small correlation be-

Table 3.3: Comparison of the force coefficient distributions from MCMC to the true values using a uniform prior.

	True value	μ	% error	σ
K_t (N/mm^2)	2200	2201.2	0.05	136.9
K_n (N/mm^2)	1200	1207.2	0.6	139.6
K_{te} (N/mm)	50	50.7	1.2	3.51
K_{te} (N/mm)	50	49.8	-0.6	3.43

Table 3.4: Correlation coefficients between the force coefficients.

	K_t	K_n	K_{te}	K_{ne}
K_t	1.00	-0.11	-0.95	-0.05
K_n	-0.11	1.00	0.25	-0.95
K_{te}	-0.95	0.26	1.0	-0.11
K_{te}	-0.05	-0.95	-0.11	1.00

tween them. However, the cutting force coefficients have a strong negative correlation with the respective edge coefficients (-0.95). The standard deviation of the posterior distributions of the force coefficients is a function of the force uncertainty used to determine the likelihood (1 N was assumed). The effect of the likelihood uncertainty on the posterior distribution is discussed in Section 3.4.2.

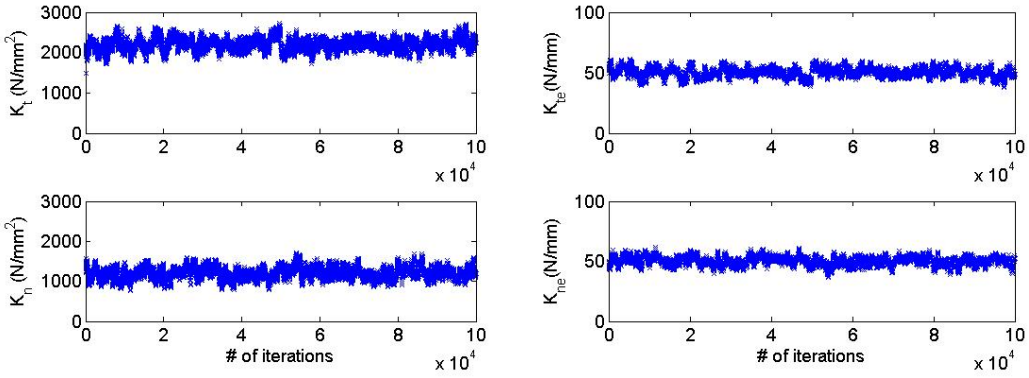

Figure 3.3: Traces of K_t and K_n (left), K_{te} and K_{ne} (right).

Using Bayesian inference, uncertainty in the force data can be propagated to determine uncertainty in the force coefficients. Furthermore, because the Bayesian

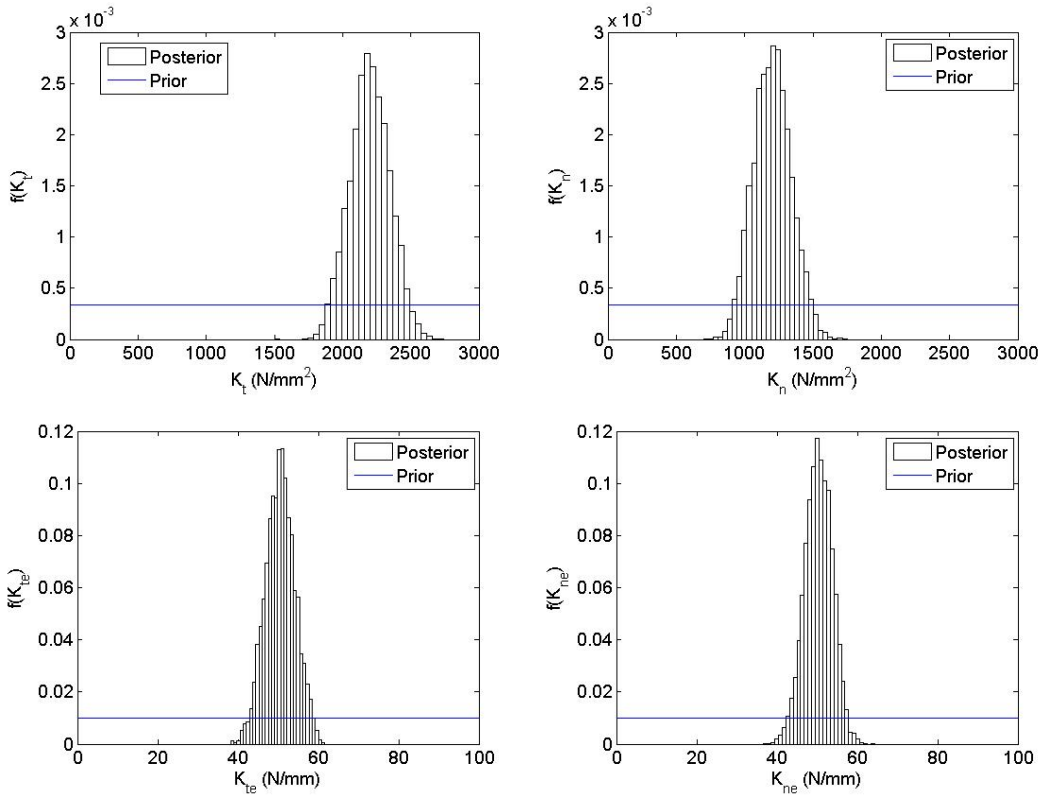

Figure 3.4: Posterior and prior distributions of K_t (top left), K_n (top right), K_{te} (bottom left), and K_{ne} (bottom right) using a uniform prior. Note that the area under the histogram was normalized to unity in each case.

updating approach does not rely on a least-squares curve fit, it eliminates data collection at several feed per tooth values. MCMC is computationally inexpensive and facilitates updating of multiple variables. The posterior samples also provide information regarding the correlation between the coefficients. These samples can be used to propagate the force coefficient uncertainty to quantify the uncertainty in the milling stability boundary, for example [36].

3.4.2 Effect of Likelihood Uncertainty

The standard deviations of the marginal force coefficient distributions listed in Table 3.4 are a function of the force uncertainty level used in the likelihood calculations. To study this effect, the updating procedure was repeated with mean force uncertainties of 0.5 N and 2 N. Figure 3.5 shows the traces of K_t and K_n with stan-

dard deviations of 0.5 N (left) and 2 N (right). Figure 3.6 shows the posterior and prior pdf comparisons of K_t for the 0.5 N (left) and 2 N (right) standard deviations. It is observed in these figures that the standard deviation of the posterior distribution reduces with the likelihood uncertainty. Similar results were obtained for all the force coefficients. The standard deviations of all coefficients at different force uncertainty levels are listed in Table 3.5. Note that the mean converges to the true values in all cases and is not affected by the likelihood uncertainty. The likelihood uncertainty may be selected by the user based on his/her level of confidence in the experimental data.

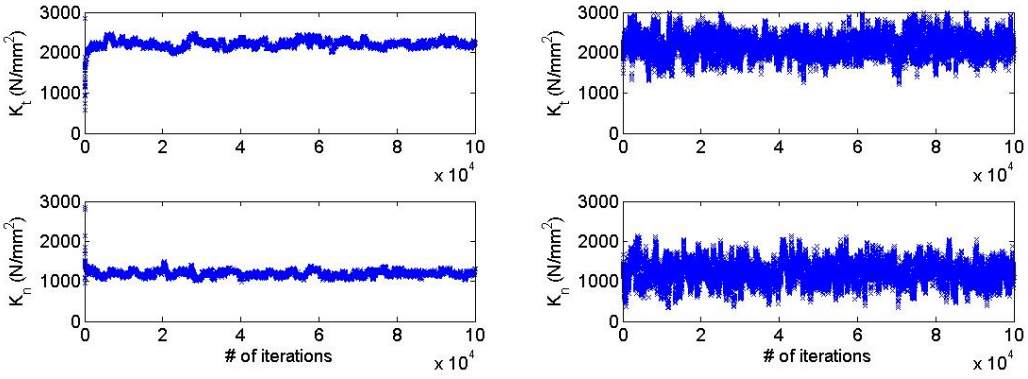

Figure 3.5: Traces of K_t and K_n with 0.5 N force measurement uncertainty (left) and 2 N (right).

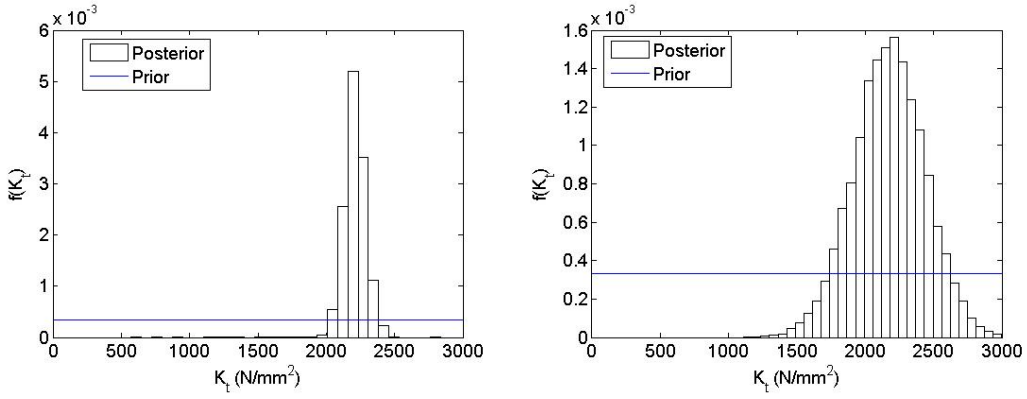

Figure 3.6: Posterior and prior distributions of K_t with a force uncertainty of $\sigma =$ 0.5 N (left) and $\sigma = 2$ N (right).

Table 3.5: Posterior force coefficient distributions with varying uncertainty in the force data.

	Force uncertainty 1σ		
.	0.5 N	1 N	2 N
K_t	N(2192.2, 75.7)	N(2201.2, 136.9)	N(2211.2, 254.0)
K_n	N(1201.2, 67.5)	N(1207.2, 139.9)	N(1197.2, 252.0)
K_{te}	N(50.8, 1.9)	N(50.7, 3.5)	N(49.7, 6.4)
K_{te}	N(49.8, 1.7)	N(49.8, 3.4)	N(50.5, 6.3)

3.4.3 Effect of the Prior Selection

In this section, the effect of the prior on the posterior distribution of force coefficients is studied. For the numerical results presented in Section 3.4.1, a uniform prior was selected. A uniform prior represents a non-informative case, where any coefficient value with the specified range is equally likely to be correct. To evaluate the influence of the prior distribution on the posterior pdf, the algorithm was repeated using normal marginal pdfs as the prior for the force coefficients. The marginal prior pdfs were selected as:

- K_t (N/mm^2) = N(2500, 300)
- K_n (N/mm^2) = N(1200, 300)
- K_{te} (N/mm) = N(100, 33)
- K_{ne} (N/mm) = N(100, 33)

Table 3.6 lists the mean and standard deviation for each of the four force coefficient posterior marginal pdfs. Figure 3.7 provides a comparison between the prior marginal pdfs and posterior sample histograms of the force coefficients. The percent errors in Table 3.6 (normal prior) are larger than those in Table 3.3 (uniform prior). The posterior distribution is clearly sensitive to the choice of the prior.

Table 3.6: Comparison of the force coefficient distributions from MCMC to the true values using a normal prior.

	True value	μ	% error	σ
K_t (N/mm^2)	2200	2240.2	1.8	224.6
K_n (N/mm^2)	1200	1059.6	-8.8	243.7
K_{te} (N/mm)	50	50.2	0.4	5.58
K_{te} (N/mm)	50	55.6	11.2	7.17

For a uniform prior, the posterior is the same as the likelihood and, therefore, the posterior mean force coefficient values converge to the true value. However, for a normal prior which includes a mean and standard deviation, the true values lie within the range of posterior distributions. Note that the posterior pdf takes into account the prior mean and the likelihood function. The prior represents the initial degree of belief about the force coefficients; if the initial belief is far from the true value, this affects the final results. The selection of the prior may be based on previous experience, values reported in the literature, or theoretical considerations. In general, the prior should be chosen to be as informative as possible considering all the available information. If enough data or prior knowledge is not available, a uniform prior may be selected. In the numerical example, the prior was chosen based on beliefs regarding the range of values the force coefficient would most likely take for the selected tool-material combination.

3.5 Experimental Results

This section describes the experimental setup used to perform force coefficient measurements. Cutting tests were performed with a 19 mm diameter inserted end-mill (one square uncoated Kennametal 107888126 C9 JC carbide insert; zero rake and helix angles, 15 deg relief angle, 9.53 mm square x 3.18 mm). The workpiece material was 1018 steel. The cutting force was measured using a table mounted dynamometer (Kistler 9257B). Figure 3.8 shows the experimental setup. The first test

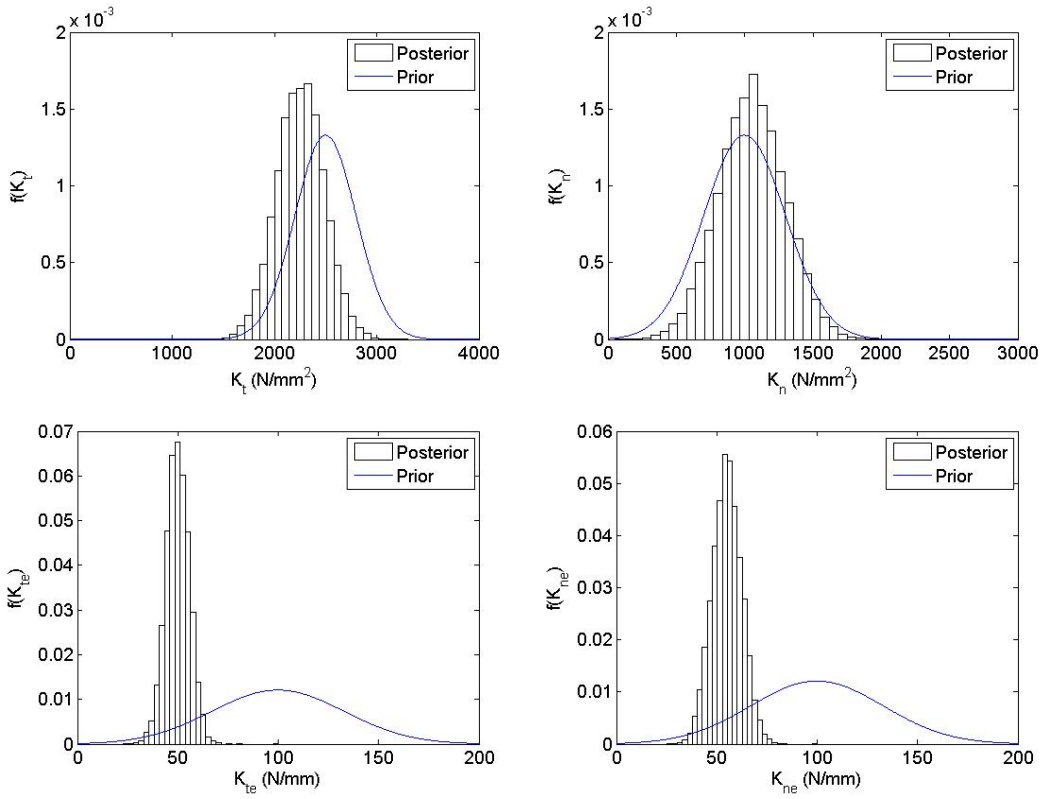

Figure 3.7: Posterior and prior distributions of K_t (top left), K_n (top right), K_{te} (bottom left), and K_{ne} (bottom right) using a normal prior.

was completed at a spindle speed, Ω, of 2500 rpm with a 3 mm axial depth of cut and 4.7 mm radial depth of cut (25% radial immersion, RI). The force coefficients were evaluated by performing a linear regression to the mean x (feed) and y direction forces obtained over a range of feed per tooth values: f_t = (0.03, 0.04, 0.05, 0.06, and 0.07) mm/tooth. Figure 3.9 shows the linear least squares best fit to the experimental mean forces in the x and y directions. The mean forces show a linear increase for both the x and y directions and the quality of fit is good (R^2 = 0.99). The force coefficients were determined using slopes and intercepts from the fit to the data. The values of the mean forces and the force coefficients are provided in Table 3.7.

The experimental force data listed in Table 3.7 was used to perform Bayesian updating on the force coefficients using the MCMC algorithm explained in Section 3.4. An uncertainty of 1 N standard deviation was assumed in the (measured) mean

Figure 3.8: Experimental setup for milling force measurement.

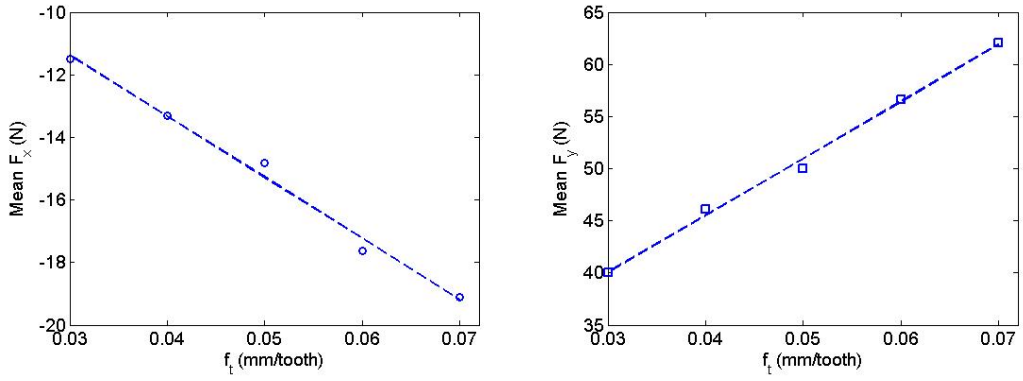

Figure 3.9: Linear regression to the mean forces in x (left) and y (right) direction to determine the force coefficients at 25% radial immersion.

force data. The prior marginal pdfs of the force coefficients were taken as uniform. Figure 3.10 shows the prior and posterior distributions of the force coefficients. The force coefficient values obtained by the linear regression approach are identified by the 'x' symbols. Note that the histograms were normalized to obtain a unit area under the curve. Figure 3.10 shows that the means of the posterior distributions for the force coefficients agree with the values obtained from the linear regression. Table 3.8 lists the correlation coefficients between the force coefficients obtained from the MCMC algorithm; they are similar to the values listed in Table 3.4. The experimental force profile at 0.05 mm/tooth was compared with the simulated force profile calculated

Table 3.7: Experimental mean forces in x and y directions and force coefficients obtained using linear regression at 25% radial immersion.

f_t (mm/tooth)	Mean F_x (N)	Mean F_y (N)	K_t (N/mm^2)	K_n (N/mm^2)	K_{te} (N/mm)	K_{ne} (N/mm)
0.03	-11.50	40.13	2149.0	1290.1	34.7	37.1
0.04	-13.31	46.10				
0.05	-14.83	50.03				
0.06	-17.64	56.63				
0.07	-19.10	62.06				

Table 3.8: Correlation coefficients between the force coefficients at 25% radial immersion.

	K_t	K_n	K_{te}	K_{ne}
K_t	1.00	-0.09	-0.95	-0.08
K_n	-0.09	1.00	0.23	-0.94
K_{te}	-0.95	0.23	1.00	-0.07
K_{ne}	-0.08	-0.94	-0.07	1.00

using the posterior mean values of the force coefficients obtained from MCMC and the least squares values. Figure 3.11 shows the force profiles for F_x (left) and F_y (right). It is observed that the force coefficients from both methods approximate the experimental force profile well.

A second test was completed at 50% RI with all other parameters the same. Figure 3.12 shows the linear least squares fit to the experimental mean forces in the x and y directions. The mean force in x direction does not show a clear linear trend (because it is approximately zero for a 50% RI and near the noise limit) and, therefore, the quality of fit is not good ($R^2 = 0.70$). The least squares fit to the y direction mean forces is very good ($R^2 = 0.99$), however. As shown in Eqs. 3.8 - 3.11, the cutting force coefficients, K_t and K_n, and the edge coefficients, K_{te} and K_{te}, are not decoupled, but depend on the slopes and intercepts of the least squares fits in both the x and y directions. Therefore, a poor fit in the x direction mean forces affects the

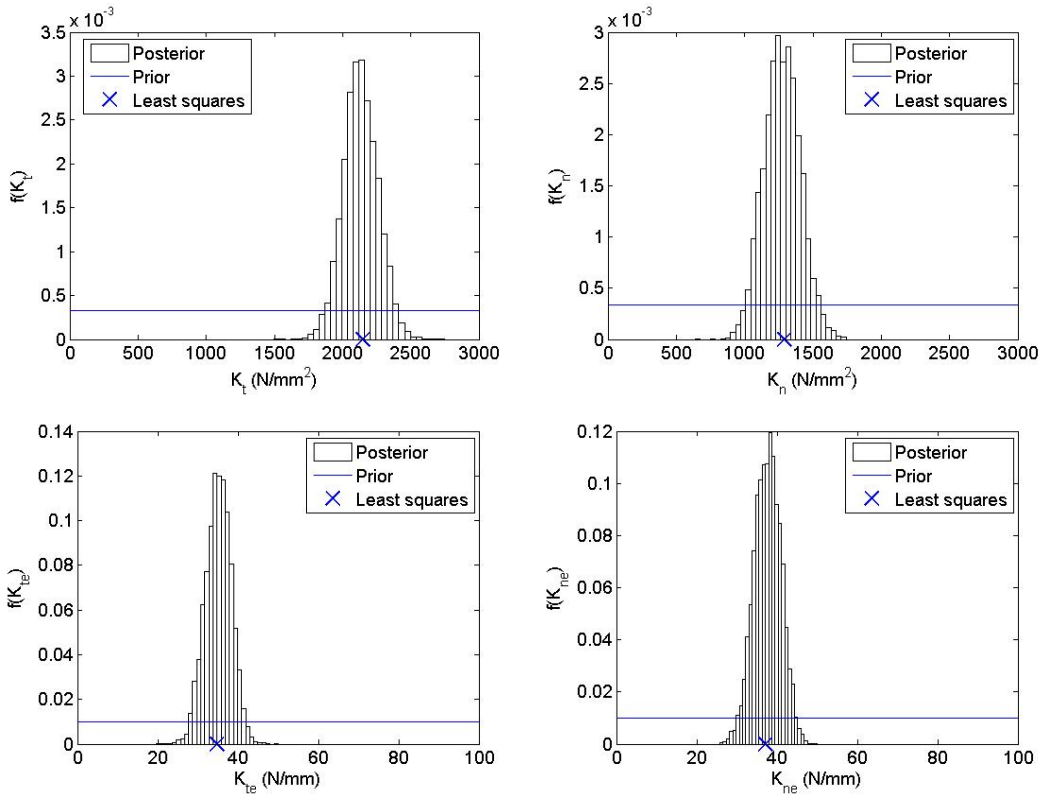

Figure 3.10: Posterior and prior distributions of K_t (top left), K_n (top right), K_{te} (bottom left), and K_{ne} (bottom right). The least squares values are identified by the 'x' symbols.

values of all coefficients. Table 3.9 shows the mean forces in x and y directions and the force coefficients obtained using the linear regression approach.

The mean force data listed in Table 3.9 was used to update the force coefficients distribution by the MCMC algorithm. Figure 3.13 shows the prior and posterior distribution of the coefficients. Table 3.10 lists the correlation coefficients between the force coefficients from the MCMC analysis. As shown in Figure 3.13, the force coefficient posterior distributions do not agree with the values obtained using the linear regression. This is due to poor least square fit for the mean x direction force. However, since the Bayesian updating does not rely on a curve fit, the posterior distributions are not affected by the quality of the fit. Table 3.11 compares the force coefficient posterior distributions at 25% and 50% RI for the MCMC analysis. The

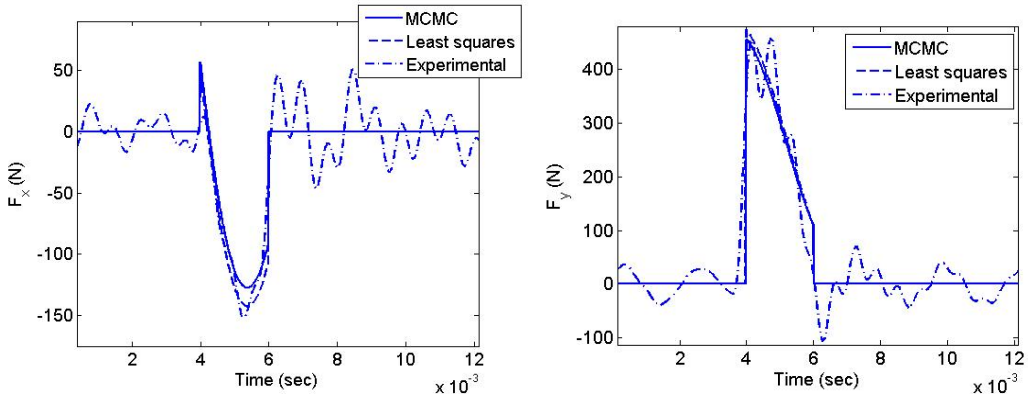

Figure 3.11: Comparison of the experimental and simulated force profiles for F_x (left) and F_y (right). The simulation used the force coefficients determined using the MCMC and least squares methods. Note that the oscillations in the experimental data are due to excitation of the dynamometer dynamics by the cutting force frequency content.

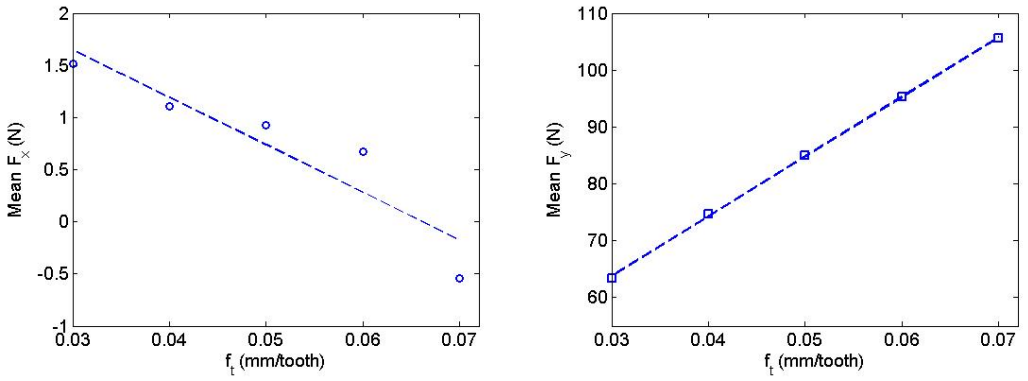

Figure 3.12: Experimental mean forces in the x and y directions and force coefficients obtained using linear regression at 50% radial immersion.

force coefficients are insensitive to the radial immersion (as expected) for Bayesian updating and the posterior distributions obtained at 25% and 50% RI agree closely. Note that the variance of the posterior distribution for the 50% RI result is smaller than for the 25% RI result. The uncertainty in the mean force was assumed to be 1 N in both cases and both the x and y direction mean forces were used for updating. However, the mean y direction force magnitude at 50% RI is greater than 25%, which results in a lower signal to noise ratio for the 50% RI y direction forces and a smaller variance for the corresponding posterior distributions. Figure 3.14 shows

Table 3.9: Experimental mean forces in x and y directions and force coefficients obtained using linear regression at 50% radial immersion.

f_t (mm/tooth)	Mean F_x (N)	Mean F_y (N)	K_t (N/mm^2)	K_n (N/mm^2)	K_{te} (N/mm)	K_{ne} (N/mm)
0.03	1.51	63.35	2504.6	1446.2	37.5	45.2
0.04	1.11	74.71				
0.05	0.93	84.98				
0.06	0.67	95.29				
0.07	-0.54	105.51				

Table 3.10: Correlation coefficients between the force coefficients at 50% radial immersion.

	K_t	K_n	K_{te}	K_{ne}
K_t	1.00	0.08	-0.93	-0.28
K_n	0.08	1.00	0.13	-0.94
K_{te}	-0.93	0.13	1.00	-0.06
K_{ne}	-0.28	-0.94	-0.06	1.00

the comparison between the experimental force profile at 0.05 mm/tooth and the simulated force profile using the posterior mean force coefficient values obtained from the MCMC and the least squares methods. It is seen that the peak force values in the x and y directions for the least squares force coefficient values is not in agreement with the experimental peak values, while the mean posterior force coefficient values agree with the experimental profile. This is because the force coefficient values obtained using the least squares method were higher than the values determined using the MCMC method.

Table 3.11: Comparison of the posterior force coefficient distributions at 25% and 50% radial immersions.

RI (%)	K_t (N/mm^2)	K_n (N/mm^2)	K_{te} (N/mm)	K_{ne} (N/mm)
25	N(2116.7, 137.3)	N(1284.4, 130.2)	N(35.2, 3.2)	N(37.4, 3.2)
50	N(2052.8, 67.8)	N(1187.8, 68.9)	N(30.4, 2.3)	N(36.7, 2.6)

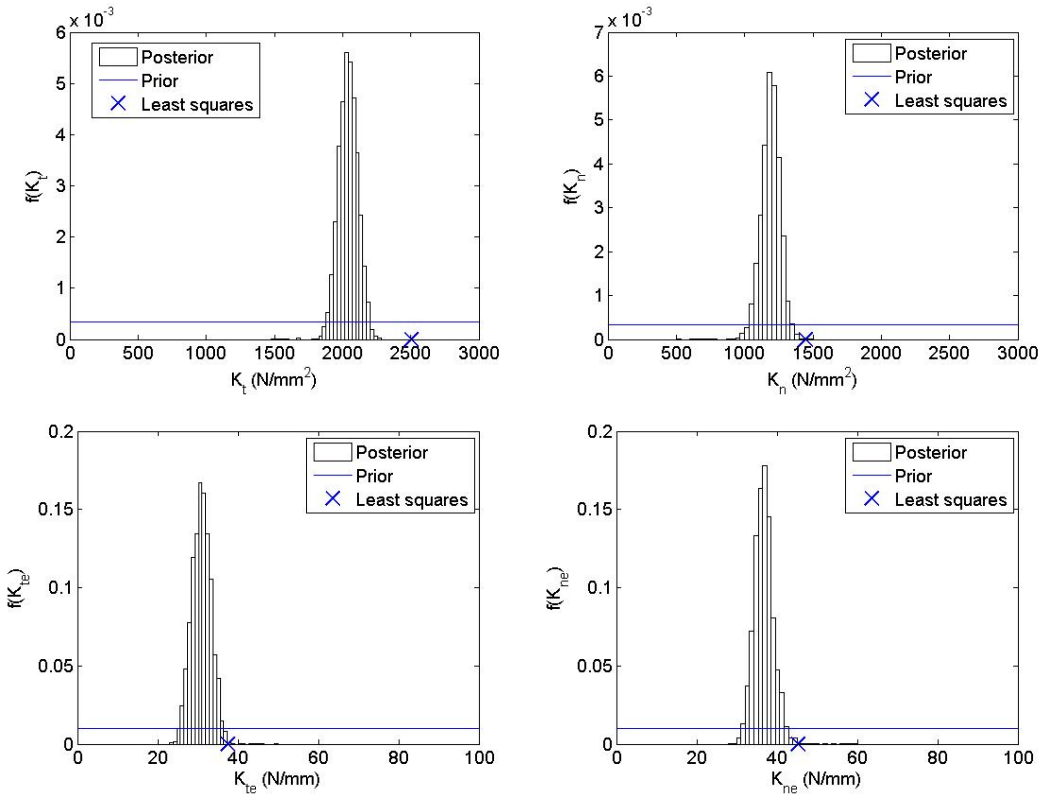

Figure 3.13: Posterior and prior distributions of K_t (top left), K_n (top right), K_{te} (bottom left), and K_{ne} (bottom right).

3.6 Discussion

Bayesian updating using the MCMC Bayesian inference technique to determine force coefficients was presented. The advantage of using a Bayesian approach is that it takes into account both initial beliefs (prior knowledge) and experimental data to update beliefs. The Bayesian inference approach also takes into account the inherent uncertainty in force coefficients. As a result, force coefficients are characterized by a probability density function as opposed to a deterministic value. To validate the posterior force coefficient distributions, five additional tests were completed at radial immersions of 25% and 50%. Figure 3.15 shows the posterior distributions of the force coefficients at 25% (left) and 50% (right). The figure shows that the posterior distributions of force coefficients agree well with the least squares values at 25% RI. However, the force coefficient values obtained by linear regression at 50% RI do not

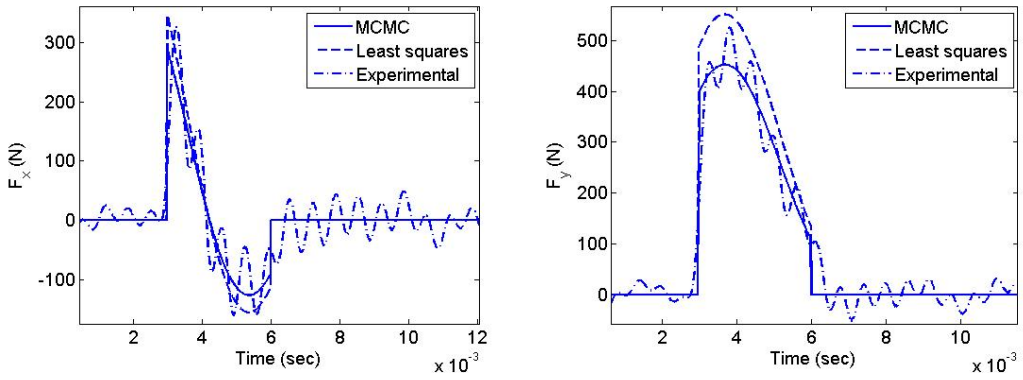

Figure 3.14: Comparison of the experimental and simulated force profiles for F_x (left) and F_y (right).

agree with the posterior distributions. As shown in Figure 3.12, this is due to a poor quality of least squares fit to the mean forces in the x direction.

Bayesian updating was performed using the mean force data from all the six tests (one experimental and five validation tests) at 25% and 50% RI. The values of the force coefficients obtained using the least squares method for the six tests at 25% and 50% RI are listed in Tables 3.12 and 3.13, respectively. The posterior mean and standard deviation value of the force coefficients at 25% and 50% using the MCMC approach are also listed. The mean and standard deviation calculated from the linear regression force coefficient values agree reasonably well with the posterior mean and standard deviation of the force coefficients. However, Bayesian inference reduces the need to perform experiments over multiple feed per tooth values, which can be time consuming and costly, by combining prior knowledge and experimental data. Therefore, the uncertainty in the force coefficients can be evaluated using a single or a few experimental results.

3.7 Conclusions

Bayesian updating of the force coefficients using the Markov Chain Monte Carlo (MCMC) method was presented. The single component Metropolis Hastings (MH) algorithm of MCMC was used. Bayesian inference provides a formal way of belief

Table 3.12: Force coefficient values from the five tests at 25% RI.

Test	K_t (N/mm^2)	K_n (N/mm^2)	K_{te} (N/mm)	K_{ne} (N/mm)
Least squares results				
1	2149.0	1290.1	34.7	37.1
2	2071.2	1159.3	27.1	30.7
3	1973.9	1210.0	34.4	34.7
4	2055.0	1337.5	33.3	32.3
5	2173.0	1370.6	35.1	35.8
6	1972.6	1265.5	33.5	32.0
μ	2065.8	1271.1	33.0	33.8
σ	84.5	78.6	3.0	2.5
MCMC results				
	N(2116.7, 137.3)	N(1284.4, 130.2)	N(35.5, 3.2)	N(37.4, 3.2)

Table 3.13: Force coefficient values from the five tests at 50% RI.

Test	K_t (N/mm^2)	K_n (N/mm^2)	K_{te} (N/mm)	K_{ne} (N/mm)
Least squares results				
1	2504.6	1446.2	37.5	45.2
2	2496.6	1422.7	41.8	51.5
3	2396.6	1310.5	46.7	60.4
4	2025.7	1126.8	29.4	35.1
5	1987.8	1048.4	32.6	41.6
6	2052.5	1268.0	42.1	49.1
μ	2243.9	1270.4	38.3	47.1
σ	246.9	158.51	6.47	8.7
MCMC results				
	N(2052.8, 67.8)	N(1187.8, 68.9)	N(30.4, 2.3)	N(36.7, 2.6)

updating when new experimental data is available. It gives a posterior distribution that incorporates the uncertainty in variables as compared to traditional methods, such as the linear regression which yields a deterministic value. By combining prior knowledge and experimental results, Bayesian inference reduces the number of experiments required for uncertainty quantification. Using Bayesian updating, a single test can provide distributions for force coefficients. The posterior distribution samples provide the covariance of the joint distribution as well. Experimental milling results showed that the linear regression did not give consistent results at 50% RI due to a poor quality of fit in the x direction mean forces, whereas Bayesian updating yielded consistent results at both radial immersions tested. Also, since Bayesian updating does not rely on a least squares fit, mean force data at different feed per tooth values is not required.

Finally, the Metropolis Hastings algorithm is a powerful tool for updating multiple variables. A grid-based method would require N^m computations, where m is the number of variables and N is the size of the grid. To illustrate, for a joint pdf of four variables with a grid size equal to 300, the grid-based method would require at least 8.1×10^9 computations. The MH algorithm would require only approximately 1×10^4 iterations for the value to converge to the posterior pdf mean values. The single component MH algorithm for MCMC facilitates updating of joint distributions without significant computational expensive.

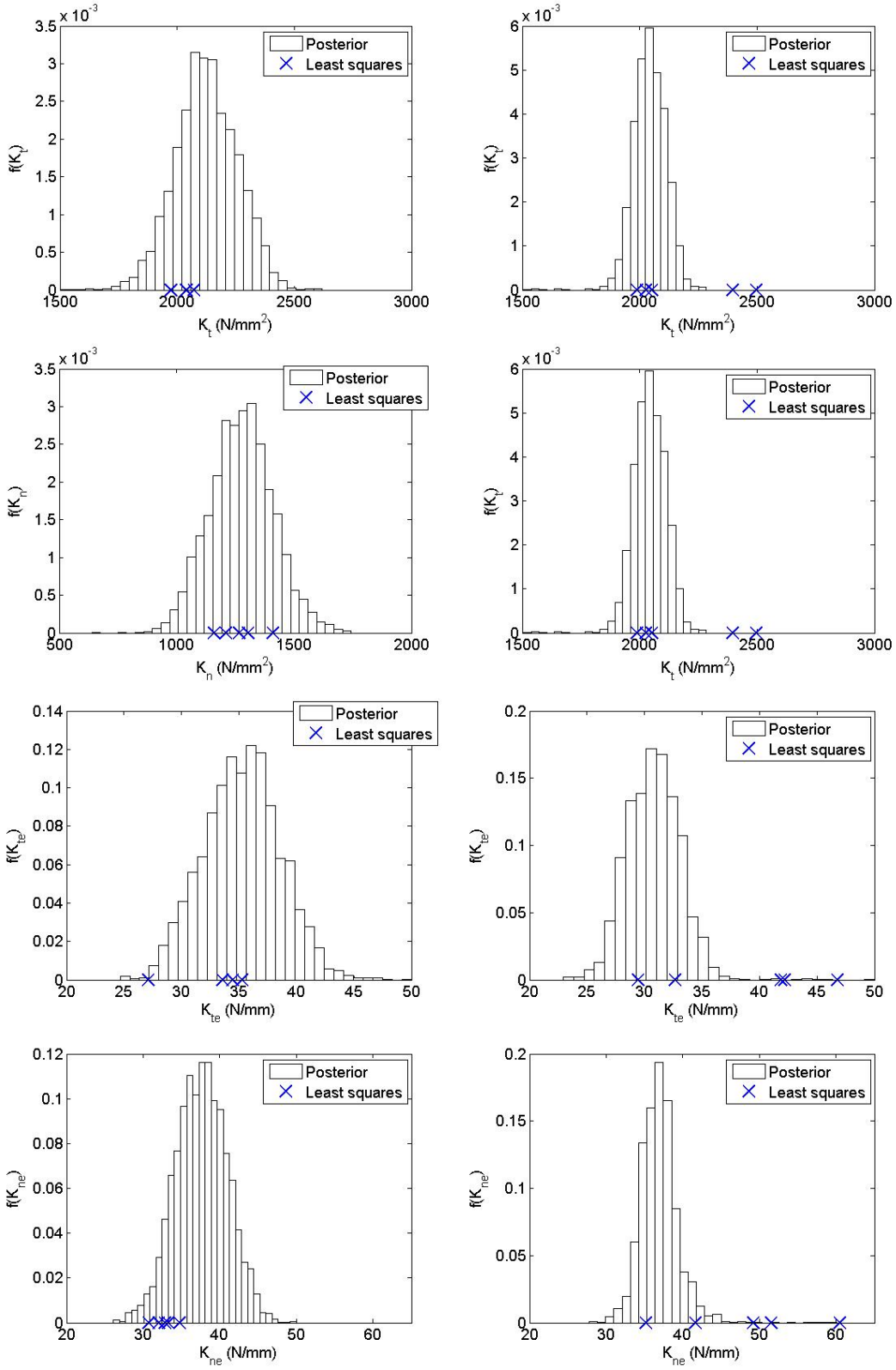

Figure 3.15: Posterior distributions of force coefficients at 25% RI (left) and 50% RI (right)

CHAPTER 4: APPLICATION TO MILLING STABILITY

Unstable cutting conditions, or chatter, limit the profitability in milling. While analytical and numerical approaches for estimating the limiting axial depth of cut as a function of spindle speed are available, they are generally deterministic in nature. Because uncertainty inherently exists, a Bayesian approach that uses a random walk strategy for establishing a stability model is implemented in this work. Bayesian inference offers several advantages: including uncertainty in the model using a probability distribution (rather than deterministic value), updating the probability distribution using new experimental results, and selecting the experiments such that the expected value added by performing the experiment is maximized. Validation of the Bayesian approach is presented.

4.1 Introduction

Discrete part production by machining is an important manufacturing capability in many industries. In these commercial situations, the focus is naturally on producing accurate parts in the required time under conditions of maximized profit. Unfortunately, a number of factors can obstruct the ability to do so. Important contributors to milling process efficiency include:

- tool and part vibrations, including chatter (self-excited vibrations) and part geometry errors due to the cutting forces and resulting dynamic deflections (forced vibrations)
- tool wear and the required tool changes
- coolant management and chip evacuation

- fixturing, including clamping/unclamping the part on the machine
- part loading/unloading from the machine
- part measurement (on-machine or post-process)
- parameter selection, such as spindle speed, depth of cut, and feed rate
- tool path planning strategies
- tooling and holder selection and
- machine accuracy, including geometric, thermal, and dynamic contributors.

A primary building block for modern machining science is Taylor's "On the Art of Cutting Metals" [37]. This study established an empirical basis for the relationships between machining parameters and cutting edge wear; contemporary research efforts still rely on variations of Taylor's tool life model. Later, Merchant's work provided a mechanics-based understanding of cutting forces, as well as the corresponding stresses and strains during material removal [38]. Within the broad view of machining encompassed by these and other early efforts, researchers have subsequently studied such basic aspects of machining as chip geometry, shear stresses, friction, and cutting temperatures [39]. The contributions of chip formation to milling behavior are typically included through the force models, which effectively treat this complex behavior using "process coefficients", or cutting force model coefficients, that relate cutting force levels to the uncut chip area [40].

While advances in computer simulation of machining process dynamics continue, the foundation for much of this work can be traced to papers by Tlusty, Tobias, Polacek and Merrit [1, 2, 3, 4], which, in turn, followed earlier work by Arnold [5] and others. Based on these efforts, an understanding of the regeneration of surface waviness during material removal as a primary mechanism for chatter in machining

was established. Predictions of stable/unstable operating parameter combinations are typically organized in stability lobe diagrams. This diagram plots axial depth of cut versus spindle speed to identify stable and unstable zones. When combined with the effects of forced vibrations during stable cutting, the basis for exploring the role of machining dynamics in discrete part production is established. Comprehensive reviews of subsequent modeling and experimental efforts have been compiled and presented in the literature (e.g., [39, 41, 42, 43, 44, 45, 46, 47]).

Although milling models are typically treated as deterministic, it is often observed in practice that stable points may lie above or below the predicted stability boundary. This is due to inaccuracy in the measured/modeled structural dynamics, cutting force coefficients, and stability model approximations[48, 49]. Existing stability formulations typically do not incorporate uncertainty effects, although some previous work has been done [36]. Here the normative foundations of decision theory are implemented to enable not only a belief representation that captures uncertainty, but also provide a systematic method to select pre-machining experiments and quantify their value. As a first step toward the goal of probabilistic stability modeling, a very basic "model", or initial belief, is applied that does not require knowledge of the system dynamics or force relationships.

For milling stability, the uncertainty that exists in the true limiting axial depth for each spindle speed is modeled using a probability distribution over a set of all possible stability limits. The probability distribution is then updated using experimental results and Bayes' rule (see Eq. 1.1). Using Bayesian inference, the predictive model incorporates uncertainty and updates beliefs as new information is made available (from experiments, for example). An important step in applying Bayes' rule is establishing the initial belief, or prior, for the stability limit. In general, this initial prediction: 1) can be constructed from any combination of theoretical considerations, previous experimental results, and expert opinions; and 2) should be chosen to be as

informative as possible regarding the experimenter's belief. In this study, the prior is determined assuming no knowledge of the system dynamics; it is based on the assumption that it is more likely to get an unstable cut as the axial depth is increased for any spindle speed. This simple prior probability distribution of stability is then updated using experimental results.

Bayesian inference offers several advantages. First, it takes into account the inherent uncertainty in the model by using a probability distribution. Second, the uncertainty (i.e., the probability distribution) can be updated using experimental data. Third, the combination of Bayesian inference and decision theory enables experiments to be selected such that the expected value added by performing the experiment is maximized, which enables the best selection of experiments. The remainder of the chapter is organized as follows. Section 4.2 describes the Bayesian updating for milling stability using a random walk approach. Section 4.3 describes the selection of experimental tests points using the value of information approach. The experimental results and validation are presented in Section 4.4. Section 4.5 details additional considerations when using the proposed method.

4.2 Bayesian Updating of Milling Stability

Bayesian inference provides a rigorous mathematical framework for updating belief about an uncertain variable when new information becomes available. The prior belief is captured using a probability distribution for the variable of interest, where the prior probability distribution about the location of the stability boundary in milling, expressed as a function of spindle speed and axial depth, is assigned by the user. In the case of milling, a joint probability distribution characterizing the probability of stability for all axial depths, b, and spindle speeds, Ω, is required. Since there is a continuum of axial depths and spindle speeds, it is helpful to use some structure in defining the joint distribution. The structure used here incorporates a random walk methodology with a Markov structure. A Markov structure means that the

conditional probability assignment to any future state depends only on the present state and not on the past states.

4.2.1 Random Walk Methodology

A random walk can be described as the probabilistic path, where the change in position at each time increment depends on the current position but is independent of all the past positions of the path. A random walk with a normally distributed step size in the particle position, x, is used in this study. This normally-distributed step size in x states that the change in position at any time is a random value selected from a normal distribution.

To illustrate, let the initial position of x be zero at time $t = 0$. At the next time instant, t_1, the new position of x is sampled from the normal distribution, N(μ, σ), with a mean of μ and standard deviation of σ. Subsequently, the position of x at any arbitrary time, t_i, is the sum of the previous position and a random value:

$$x(t = t_i) = x(t = t_i - 1) + N(\mu, \sigma). \tag{4.1}$$

Note that the value at any future state depends only on the present state, but not on any of the previous states. Figure 4.1 shows 20 sample paths of x starting at $t = 0$ seconds and continuing to $t = 10$ seconds. The time axis was divided into discrete increments of 0.01 seconds and the new position was sampled for each of these increments. The position step size was normally distributed with zero mean and standard deviation equal to 0.1, i.e. N(0, 0.1). At each time increment of 0.01 seconds, the position of x was determined by the addition of its current position and a randomly generated x step size sampled from N(0,0.1). Thus, $x(t = t_i) = x(t = t_i$ - 0.01) + N(0,0.1).

A normally distributed step size ensures that the distribution of x at any time instant is also normal. Additionally, since the step size distribution has zero mean,

the mean of the distribution of x is nominally zero at all time instants. Figure 4.2 shows 5000 sample paths generated using N(0,0.1), starting from $x = 0$ at $t = 0$ seconds. Figure 4.3 shows the distribution of x at $t = 5$ seconds (left) and $t = 10$ seconds (right). As shown in the figure, the distribution of x is normal with a zero mean. It is also observed that the variance increases with time. Since the increments are generated independently, the variance after n steps is equal to the variance of each increment multiplied by n. Comparing the two distributions in Figure 4.3 shows that the uncertainty in x increases with time.

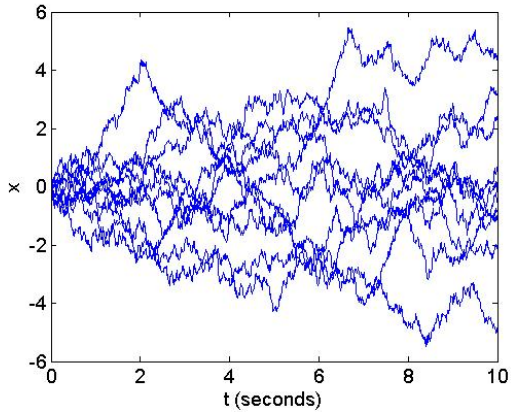

Figure 4.1: Twenty random walks with a normally-distributed position step size described by N(0,0.1).

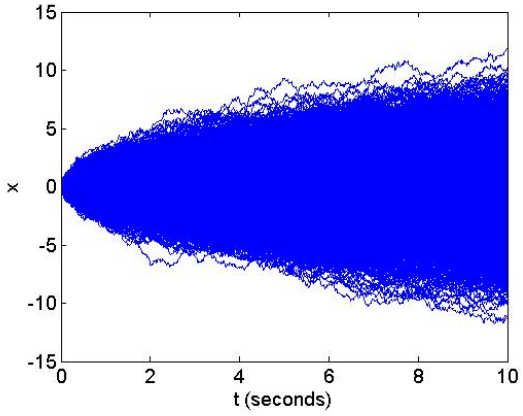

Figure 4.2: 5000 sample paths generated with a normally distributed step size.

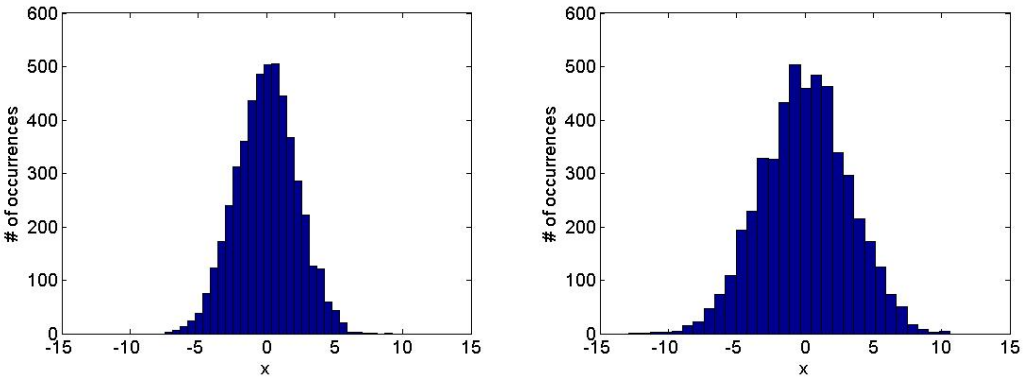

Figure 4.3: Histograms of x at 5 seconds (left) and 10 seconds (right).

4.2.2 Bayesian Inference

The random walk method can be applied to describe the prior belief about the uncertain stability boundary (or limit) in a spindle speed-axial depth of cut domain given knowledge of the limit at a particular point in the domain. The sample paths can be generated in spindle speed increments (instead of time) and the position step size is selected for the axial depth of cut. The stability boundary prediction proceeds by generating N sample paths, each of which may represent the actual stability boundary. The probability that each sample path is the true stability limit based on this model is $1/N$. These sample paths are used as the prior in applying Bayesian inference. This prior shows that the uncertainty in the location of the stability limit increases when moving further away from a point (i.e., a combination of spindle speed and axial depth) where the stability limit is known. The prior probability is then updated by experimental results using Bayes' rule. For each sample path, Bayes' rule can be written as shown in Eq. 4.2.

$$\mathrm{P}(\textit{path} = \textit{true stability limit}|\textit{test result}) \propto$$

$$\mathrm{P}(\textit{test result}|\textit{path} = \textit{true stability limit})\mathrm{P}(\textit{path} = \textit{true stability limit})$$

Here P(*path = true stability limit*) is the prior probability which, before any testing, is equal to $1/N$ for any sample path and P(*test result* | *path = true stability limit*) is the likelihood of obtaining the test result given the true stability limit. Their products yields the posterior stability limit probability given the test result, P(*path = true stability limit* | *test result*). In practice, the probability of the test result, P(*test result*), may be used to normalize the posterior probability (by dividing the right hand side of Eq. 4.2 by this value).

4.2.3 Constructing the Prior Distribution

In Bayesian inference, the prior probability represents the initial degree of belief regarding the stability limit. The sample paths generated using the random walks are used to define a prior probability of stability. To construct the prior, a spindle speed-axial depth of cut domain was first defined. For demonstration purposes, the operating spindle speed was arbitrarily selected to be between 4000 rpm and 10000 rpm. It was assumed that for all spindle speeds within the operating range, the stability limit is between 0 and the maximal axial depth defined by the flute length (selected to be 10 mm). Following the same procedure described in Section 4.2.1, random walks were generated. The starting point was the midpoint of the axial depth range (5 mm). The sample paths were started from $\Omega = 0$ rpm to allow the paths to cross the maximum axial depth of 10 mm by 4000 rpm and continued to $\Omega = 15000$ rpm. The step size in mm was described by N(0,0.5). Figure 4.4 shows many sample paths.

Each sample path represents the true stability limit with some probability. To illustrate how we can incorporate our prior information this way, suppose we would like to confine the stability limit within the spindle speed range 4000 rpm and 10000 rpm to be between within the axial depths 0 and 10 mm. This implies that the paths which cross outside 0 or 10 mm within the spindle speed range of 4000 rpm to 10000 rpm have a zero probability of being the true stability limit since they are outside

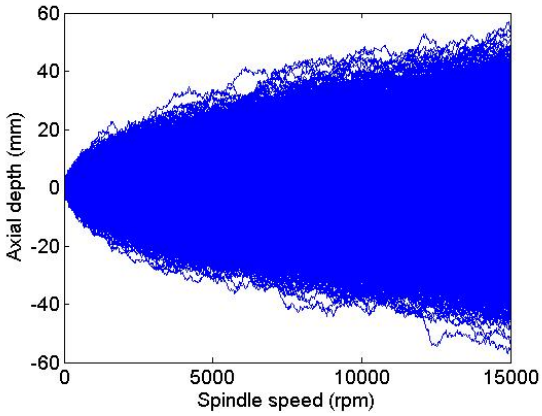

Figure 4.4: Many sample paths generated in the spindle speed-axial depth domain.

the pre-defined stability domain. These sample paths are filtered out or multiplied by zero. The probability that the remaining paths represent the true stability limit is now $1/N$, where N is the number of remaining paths. Figure 4.5 shows 10000 sample paths which have the axial depth within 0 to 10 mm in the spindle speed range of 4000 rpm to 10000 rpm.

Figure 4.6 shows the histogram of axial depths at 4000 rpm at 10000 rpm. Note that the axial depth histograms are confined within 0 mm and 10 mm due to path filtering. The mean is 5 mm at all spindle speeds since the starting point of the walks was selected as 5 mm.

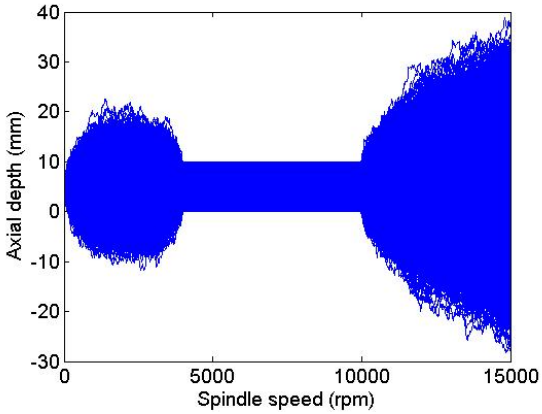

Figure 4.5: 10000 sample paths after filtering. The paths that cross 0 or 10 mm in the spindle speed range of 4000 rpm to 10000 rpm have been removed.

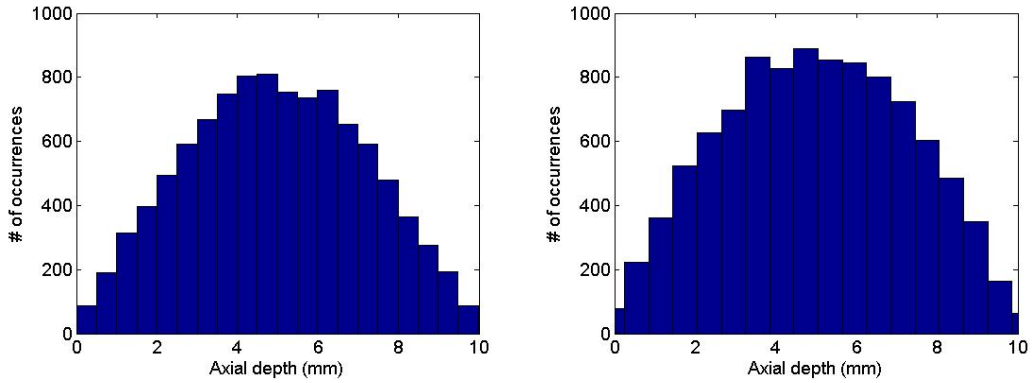

Figure 4.6: Histograms of axial depths at 4000 rpm (left) and 10000 rpm (right).

The cumulative distribution function (cdf) is then calculated at each spindle speed within the domain using the histograms. Figure 4.7 shows the complementary cdf for the axial depth, which is initially the same at each spindle speed. The complementary cdf gives the probability that an axial depth will be stable. As shown in Figure 4.7, the probability is 0 that an axial depth greater than 10 mm will be stable and the probability that an axial depth greater than 5 mm will be stable is 0.5. The cdf therefore states that the probability of obtaining a stable cut increases as the axial depth of cut is reduced. Since machining is not possible at an axial depth of 0, the minimum axial depth is taken to be 0.01 mm. Figure 4.8 shows the complementary cdf over the spindle speed domain. It represents the prior or initial belief, about the stability boundary. In this case, the prior was only based on the assumption that the probability of obtaining a stable cut decreases with higher axial depths.

4.2.4 Updating using Experimental Stability Results

In the case of stability testing, if the true stability limit was known, then it would be known with certainty whether the result of a test would be stable or unstable. The test would be stable with a probability of 1 if the test point was below the stability limit and stable with a probability of 0 (unstable with a probability of 1) if the test point was above the stability limit. For the random walk approach, recall that each

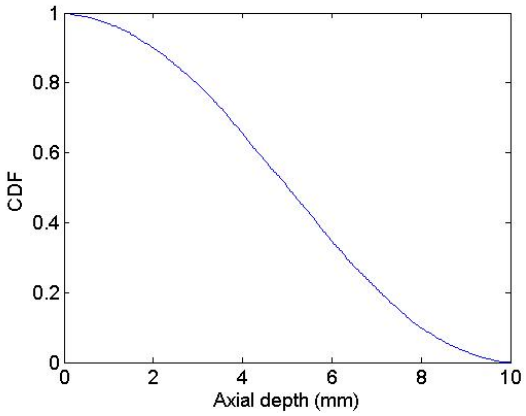

Figure 4.7: Complementary cdf of stability at axial depths from 0 to 10 mm. The probability of stability decreases with increasing axial depth.

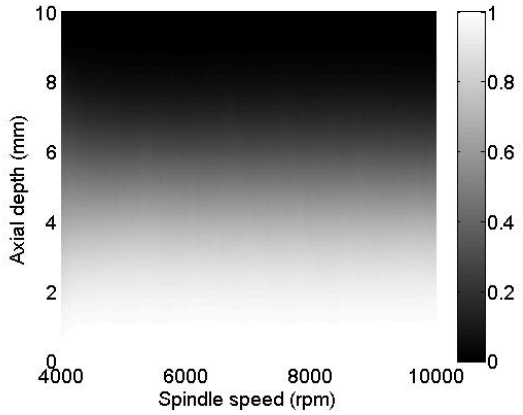

Figure 4.8: Prior cdf for stability in the spindle speed-axial depth domain. The probability of stability is 0 at an axial depth of 10 mm.

sample path represents the true stability limit with a probability of $1/N$. Suppose a test is performed at some spindle speed-axial depth combination and the result is stable. This implies that all paths with axial depths below the test point at the selected spindle speed cannot be the true stability limit (according to linear stability theory and the traditional Hopf bifurcation behavior [1, 2, 3, 4, 7]. Similarly, for an unstable test result, all paths with a higher axial depth at the test spindle speed cannot be the true stability limit. Therefore, for a stable test, the likelihood for each path with a higher axial depth than the test point is 1 and the likelihood for each path with a lower axial depth is 0. Similarly, for an unstable test, the likelihood for

each path with a higher axial depth is 0 and the likelihood for each path with a lower axial depth than the test point is 1.

Because the likelihood for every path is always either 0 or 1, the updating procedure proceeds by filtering out paths after each test result. After any number of tests, all paths which have not been filtered out (i.e., multiplied by a likelihood of 0) will have a probability equal to the reciprocal of the remaining number of paths. When updating the prior using a test result, the paths which do not agree with the test result are filtered out and the remaining paths represent the updated stability prediction.

To illustrate, consider a stability test completed at $\Omega = 7000$ rpm and $b = 5$ mm. A stable test implies that all axial depths below 5 mm would be stable at $\Omega = 7000$ rpm. As a result, the likelihood that any path that with an axial depth less than 5 mm at $\Omega = 7000$ rpm is the true stability limit is zero. All such paths are filtered out, or multiplied by zero, to obtain the updated prediction. Similarly, if the test at $\Omega = 7000$ rpm and $b = 5$ mm was unstable, the likelihood that any path with an axial depth greater than 5 mm at $\Omega = 7000$ rpm is the true stability limit is zero and all such paths are filtered out. Figure 4.9 shows the remaining paths after filtering given a stable test result (left) and an unstable test result (right). As seen in Figure 4.9, all paths that are below 5 mm at 7000 rpm are filtered out for a stable test result while the paths above 5 mm at 7000 rpm are filtered out for an unstable test result. Note that Figure 4.9 only shows the path in the spindle speed range from 4000 rpm to 10000 rpm.

The updated probability distributions can then be calculated using the data from the histograms of axial depths at each spindle speed within the domain. As noted, all paths which have not been filtered out (those with a likelihood of 1) will have a probability equal to the reciprocal of the remaining number of paths. For a stable result at $\Omega = 7000$ rpm and $b = 5$ mm, the remaining number of paths is 4970 while

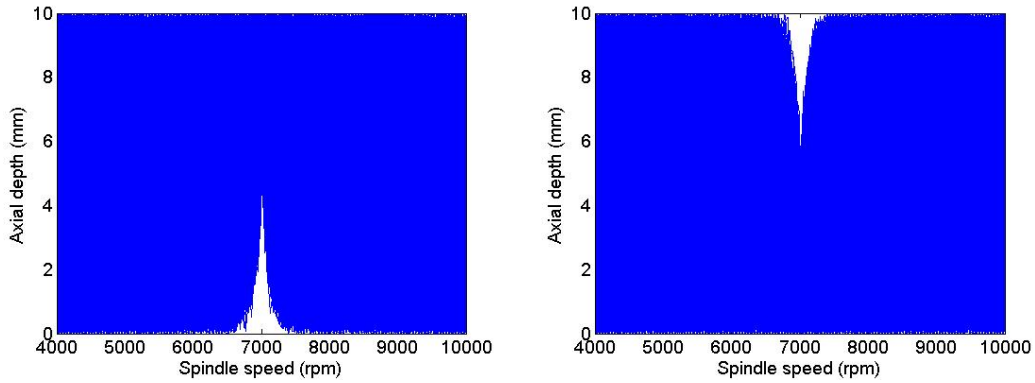

Figure 4.9: Sample paths remaining after filtering given a stable test result (left) and an unstable test result (right) at and axial depth of 5 mm and spindle speed of 7000 rpm.

an unstable result gives 5030 remaining paths for this example. Figure 4.10 shows the updated complementary cdf at the test speed given a stable result (left) and an unstable result (right). Figure 4.11 shows the updated posterior cdf of stability given a stable (left) and unstable (right) result at $\Omega = 7000$ rpm and $b = 5$ mm. As seen from the posterior cdf, the single test updates the distribution at all spindle speeds. The extent to which a test at one spindle speed updates the distribution at all speeds depends on the standard deviation of the step size for the random walk. This dependence is evaluated in Section 4.5.

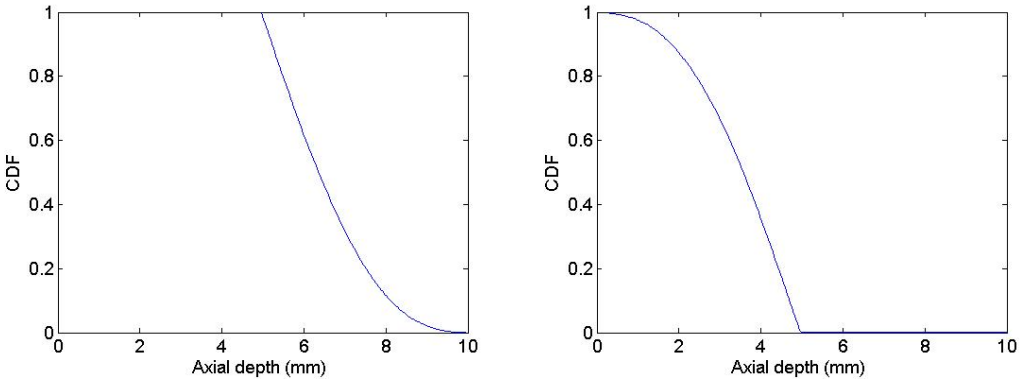

Figure 4.10: Updated cdf at 7000 rpm given a stable test result (left) and an unstable test result (right) at a test axial depth of 5 mm.

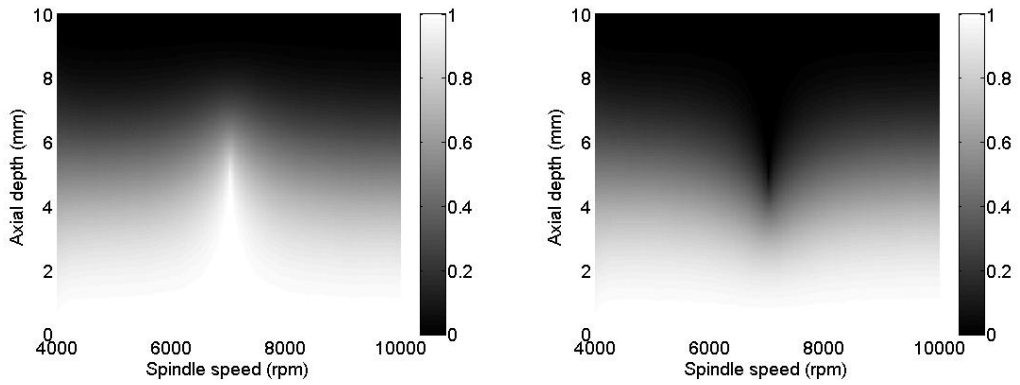

Figure 4.11: Posterior cdf for milling stability given a stable test result (left) and an unstable test result (right) at an axial depth of 5 mm and spindle speed of 7000 rpm.

4.3 Value of Information for Experiment Selection

Bayesian inference combined with decision analysis models enables a dollar value to be placed on the information gained from an experiment prior to performing it. This value is referred to as the value of information. It may be defined as the expected profit before testing minus the profit after testing or, in terms of cost, the expected cost prior to testing minus the cost after testing. Note that while the value of information uses expected value after testing, it is calculated before actually performing the test.

The primary motivation for defining the value of information is to optimize the selection of experiments. The experimental test point is selected which adds the most (expected) value to the profit. In addition, if the expected cost of performing an experiment is more than the expected value gained from the experiment, it is not recommended that the experiment be completed. This is a major advantage over statistical design of experiments, which typically does not consider profit in test point selection. In the value of information approach to milling stability modeling, a test is performed at a point where the maximum information/value about the stability limit is obtained.

To illustrate this point, consider a simple situation where only three spindle speed-

axial depth combinations are available (A, B, and C). Suppose it is initially predicted that A is definitely stable, while B and C each have a 50% chance of being stable. In addition, suppose that the cost of machining (assuming the cut is stable) is $100 using A, $50 using B, and $30 using C and that only stable operating points will be used (based on the assumption that the cost of performing an unstable cut is very large due to the subsequent rework or scrap). Prior to performing the stability test, only A can be chosen as the operating point and, therefore, if no testing is performed the cost of machining will be $100. However, suppose the option of performing a single stability test at either A, B, or C was given. How can the proper test be selected? Because it is already known that a test at A will have a stable result, no test should be completed at A because no new information will be obtained. However, if it was possible to test at B, there is a 50% chance that the result is unstable, in which case the choice will still be A and the cost will be $100. On the other hand, there is also a 50% chance that the test will be stable, in which case B will be selected and the cost will only be $50. The expected cost of machining given the result of a test at B is therefore $75. The value gained by testing at B (defined as the cost prior to testing minus the expected cost after testing) is $25. Similarly, the value gained by testing at C can also be calculated. There is a 50% chance that the result will be unstable, in which case machining will be completed at A and the cost will be $100. There is also a 50% chance that the test will be stable and then machining will be completed at C and the cost is only $30. Thus, the expected cost given the result of a test at C is $65 and the value gained by testing at C is $35. Now (assuming the goal is to maximize profit), the question of which test to perform has a straightforward answer: choose the test which adds the most value. For this example, testing would be completed at C.

4.3.1 Cost Formulation

Before calculating the value of information, it is necessary to determine the cost of performing the operation given the selected operating conditions. To calculate the cost, a the feature to be machined was specified as a pocket with dimensions of 150 mm in the x direction, 100 mm in the y direction, and 25 mm deep. The tool path is shown in Figure 4.12.

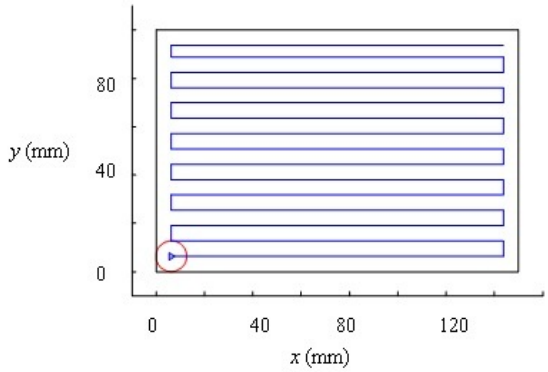

Figure 4.12: Tool path for pocket milling.

The cost function does not include the effects of tool wear; it was neglected for the 6061-T6 workpiece/TiCN-coated carbide tool combination considered in this study. The simplified cost, C, shown in Eq. 4.2 is based on the machining cost per minute, $r_m = \$2$, and machining time, t_m, which depends on the part path geometry and machining parameters. The parameters used to calculate the cost for machining the pocket are listed in Table 4.1. Due to the nature of the part path, for any selected spindle speed the cost function is stepped; see Figure 4.13. These steps occur at an integer fraction of the pocket depth.

$$C = t_m r_m \tag{4.2}$$

Table 4.1: Parameters used to determine the reference stability limit for the simulated testing scenario.

Parameter	Value	Units
Radial depth	19.0	mm
Feed per tooth	0.06	mm/tooth
Tool radius	9.5	mm
Number of teeth	1	teeth
Helix angle	0	deg

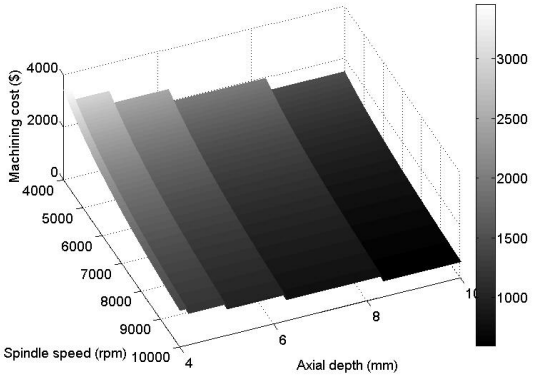

Figure 4.13: Cost of machining at axial depth-spindle speed combinations given that the resultant cut is stable. Notice the steps in the cost function at integer fractions of the pocket depth.

4.3.2 Selecting the Test Points

The revenue generated by machining the selected pocket is assumed to be $2000 for this example. Profit is defined as the revenue generated minus the machining cost. For constant revenue (generated in machining the feature), maximizing profit is equivalent to minimizing the expected cost. Since each point has a probability of stability, the expected profit a given pair of operating parameters, (Ω_{op}, b_{op}), is given by:

$$\begin{aligned} V_{prior}(\Omega_{op}, b_{op}) = P_{stable}(\Omega_{op}, b_{op}) V_{stable}(\Omega_{op}, b_{op}) + \\ (1 - P_{stable})(\Omega_{op}, b_{op}) V_{unstable}(\Omega_{op}, b_{op}) \end{aligned} \tag{4.3}$$

where the subscript op denotes operating point, P_{stable} is the prior probability of stability at the operating point (see Figure 4.7), V_{stable} is the profit given that the cut is stable, $V_{unstable}$ is the profit given that the cut is unstable, and V_{prior} is the expected profit for machining the pocket at (Ω_{op}, b_{op}) prior to performing any further test. Unstable operating points are considered infeasible since it is assumed that the cost added by reworking the part and the cost associated with potential damage to tooling are substantially higher than the revenue generated in machining the pocket. Thus, the operating point would be the one which is stable with certainty ($P_{stable} = 1$) and provides the highest profit within the domain (according to Eq. 4.3). This implies that the cost of instability is negative infinity. Recall that it was assumed that a 0.01 mm axial depth is stable at all spindle speeds within the domain. Therefore, before performing any test, the profit would be highest at an axial depth of 0.01 mm and spindle speed of 10000 rpm since the machining time would be minimized at the maximum spindle speed. The maximum profit before performing any test, V^*_{prior}, is therefore the profit at (10000, 0.01).

The expected value of performing a test at any point (Ω_{test}, b_{test}) is calculated as follows (the subscript test indicates a test point). Each test is assumed to be either stable or unstable. The resultant posterior cdf is different for a stable result at the test point than it is for an unstable result (see Figure 4.11). Subsequently, the profit after the test, calculated using the posterior cdf, is also different for a stable test than for an unstable test. Assume that a test at (Ω_{test}, b_{test}) is stable. The maximum profit would be at (Ω_{test}, b_{test}), since that operating point is known to be stable with certainty. The maximum profit would be equal to V_{stable} (Ω_{test}, b_{test}). However, if the cut is unstable, the maximum expected profit would be equal to the maximum profit before performing the test, V^*_{prior}. This is the case because with an unstable test cut, no additional point is known to be stable with certainty and the cost of an unstable cut is negative infinity. Thus, the expected profit, V_{test}, after performing a test at

any (Ω_{test}, b_{test}) is given by Eq. 4.4.

$$V_{test}(\Omega_{test}, b_{test}) = P_{stable}(\Omega_{test}, b_{test})V_{stable}(\Omega_{test}, b_{test}) + (1 - P_{stable})(\Omega_{test}, b_{test})V^*_{prior}) \tag{4.4}$$

The value of information, or the value obtained by performing an experiment, is defined, for an expected value maximize, as the expected profit given the test results minus the profit before testing as shown in Eq. 4.5.

$$\begin{aligned} \text{VOI} &= V_{test}(\Omega_{test}, b_{test}) - V^*_{prior} \\ &= P_{stable}(\Omega_{test}, b_{test})V_{stable}(\Omega_{test}, b_{test}) \\ &= P_{stable}(\Omega_{test}, b_{test})V_{stable}(\Omega_{test}, b_{test}) - V^*_{prior} \end{aligned} \tag{4.5}$$

A test is only performed where the value of information is the highest. Therefore, the test parameters are selected using Eq. 4.6.

$$(\Omega_{test}, b_{test}) = max(P_{stable}(\Omega_{test}, b_{test})V_{stable}(\Omega_{test}, b_{test}) - V^*_{prior}) \tag{4.6}$$

The expected value of the test is based on the prior probability of stability. After a test is performed, the prior cdf is updated using the test result. This updated posterior distribution is the prior distribution used to determine the next test point. This process is repeated for a selected number of tests. Once a stable result from a test is obtained (and for all further stable test results), V^*_{prior} is the maximum profit from all points known to be stable with certainty.

4.4 Experimental Results

Using the value of information approach, a sequence of 20 tests was completed. The operating conditions for each test point were selected to maximize the value of information at that time. Note that when using this value of information approach,

Table 4.2: Experimental test point and results

Test number	Spindle speed (rpm)	Axial depth (mm)	Stability result
1	10000	0.54	stable
2	10000	2.51	stable
3	10000	4.18	stable
4	10000	6.25	stable
5	10000	8.36	unstable
6	9819	8.36	unstable
7	9639	8.36	unstable
8	9920	8.36	unstable
9	9398	8.36	unstable
10	9117	8.36	unstable
11	9719	8.36	unstable
12	8916	8.36	unstable
13	9960	8.36	unstable
14	8595	8.36	unstable
15	9498	8.36	unstable
16	9880	8.36	unstable
17	9278	8.36	unstable
18	8294	8.36	unstable
19	9779	8.36	unstable
20	8776	8.36	unstable

each test is treated separately. For multiple tests, each test point is selected assuming that no additional tests will be completed. The random walk prior for this example was composed of 1×10^5 sample paths. Figure 4.14 shows the test points selected using the value of information approach, where stable test results are marked as 'o' and unstable as 'x'. The results are also summarized in Table 4.2.

The stability was evaluated by observing the frequency content of the acceleration signal obtained by attaching a low-mass accelerometer to the flexure test platform; see Figure 4.15. The sidewall surface was also used to identify unstable cuts. Figure 4.16 shows the frequency content of the acceleration signal and the machined surface for a test cut at (10000 rpm, 6.25 mm). For this stable result, content is observed only at the tooth passing frequency (166.66 Hz) and its harmonics and the surface is

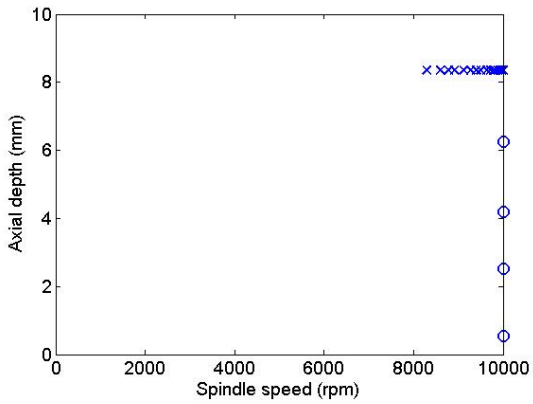

Figure 4.14: Stability results for the value of information testing.

smooth. Figure 4.17 provides the same information for a cut at 8294 rpm, 8.34 mm. Frequency content exists at frequencies other than the tooth passing frequency and its harmonics. Also, the surface has distinctive chatter marks indicating an unstable cut. Figure 4.18 shows the posterior stability cdf of stability after the 20 tests. Based on these results, the optimum operating point is (10000 rpm, 6.25 mm) with a profit of $1206.50 per part.

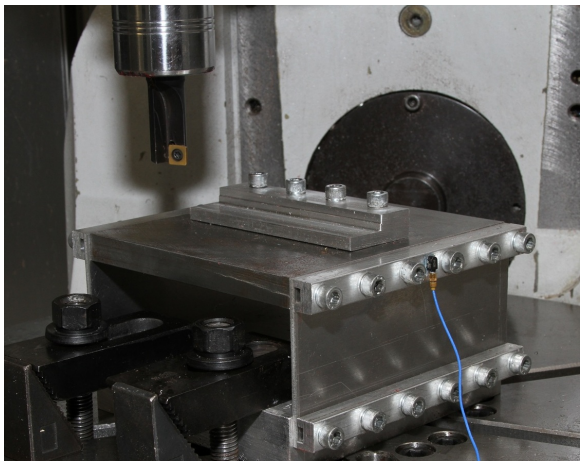

Figure 4.15: Experimental setup for stability testing.

To validate the performance of the algorithm, the analytical stability boundary was evaluated using a frequency-domain analytical approach [30]. The force model coefficients and the frequency response function (FRF) of the flexure on which the tests were performed were measured. The force model coefficients for the 6061-T6

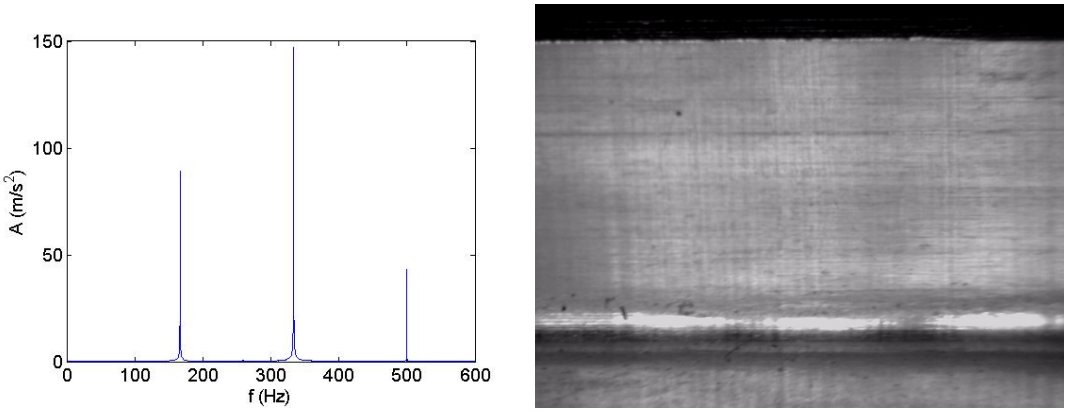

Figure 4.16: Frequency content of the acceleration signal (left) and the machined surface (right) at 10000 rpm, 6.25 mm. Content is seen only at the tooth passing frequency (167 Hz) and its harmonics.

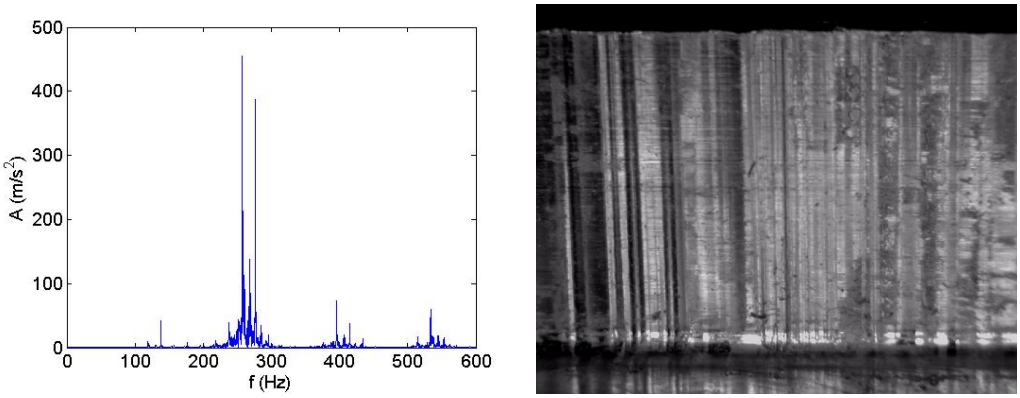

Figure 4.17: Frequency content of the acceleration signal (left) and the machined surface (right) at 8294 rpm, 8.34 mm. This unstable cut exhibits content other than tooth passing frequency and its harmonics (left) and chatter marks are observed (right).

workpiece material-tool combination were calculated using a linear regression to the mean values of x (feed) and y direction cutting forces measured over a range of feed per tooth values [30]. The FRFs of the flexure in the x (feed) and the y directions were also measured using impact testing; see Figure 4.19. The force coefficients are listed in Table 4.3. Figure 4.20 shows the stability lobes calculated along with the test points.

Note that from the analytical stability boundary, the optimum operating point is (7870 rpm, 8.34 mm) with a profit of \$1220.00 per part. The operating point (10000

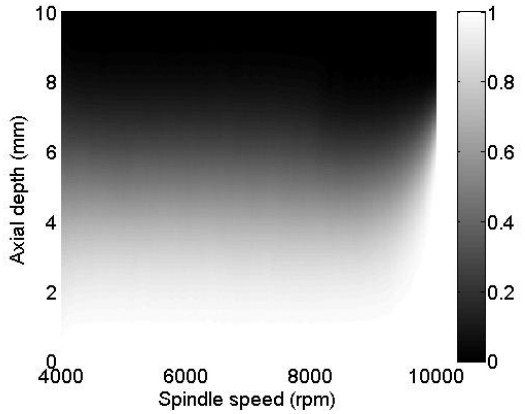

Figure 4.18: Posterior stability cdf after 20 tests.

Table 4.3: Parameters used to determine the reference stability limit for the simulated testing scenario.

Parameter	Value	Units
Tangential coefficient	853.0	N/mm^2
Normal coefficient	310.0	N/mm^2
Tangential edge coefficient	10.0	N/mm
Normal edge coefficient	8.0	N/mm

rpm, 6.25), which gives a profit of \$1206.5, would not have been chosen based on the analytical boundary. However, the stability boundary obtained using the analytical is deterministic and uncertainty exists in the measured cutting force coefficients and FRFs, so some disagreement with experiment is anticipated. Even without knowledge of the system dynamics, the value of information approach was successful in locating the optimal operating point. The analytical stability lobes shown in Figure 4.20 were also validated experimentally. Figure 4.21 shows the analytical prediction and the test results, where 'o' denotes a stable cut and 'x' denotes an unstable cut. The testing locations were selected only to verify the lobe shape; the value of information approach was not applied.

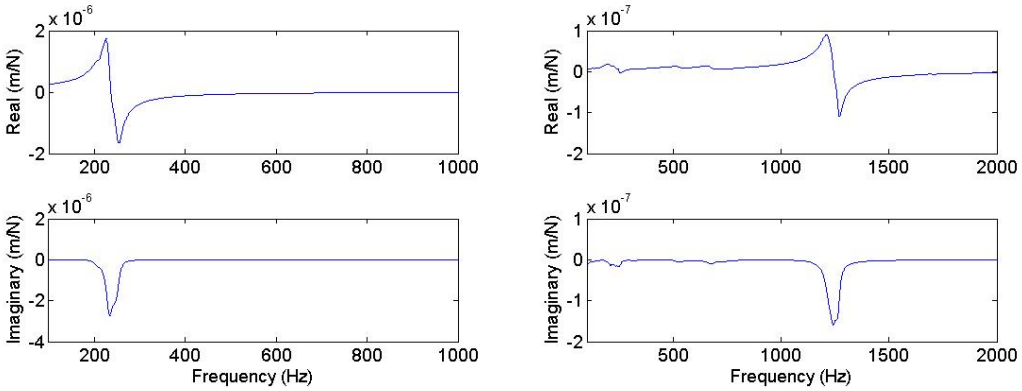

Figure 4.19: FRFs for the flexure in the x (left) and the y (right) directions used in the experiments. Note that the dynamic stiffness is an order of magnitude higher in the y direction.

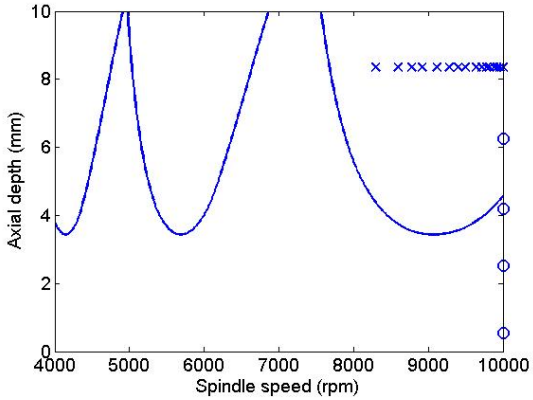

Figure 4.20: Test point selections compared with the analytical stability lobes.

4.5 Discussion

In this section, the effect of the standard deviation for the random walk step size on the posterior cdf and the test points is evaluated. The effect of the spindle speed-axial depth of cut domain on the posterior stability and test points is also explored.

Using the random walk approach, a test at any spindle speed updates the distribution at all spindle speeds. The extent to which a test at a spindle speed updates the distribution at spindle speeds other than the test speed depends on the standard deviation of the step size. To evaluate this dependence, random walks were generated

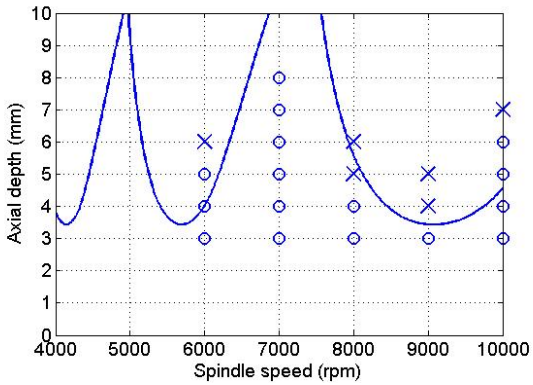

Figure 4.21: Experimental validation of the stability lobes.

using a normally distributed step size with zero mean and a standard deviation equal to 0.25 mm, N(0,0.25). The random walks in Section 4.2 were generated using a standard deviation equal to 0.5 mm, N(0,0.5). Consider that the updating was performed based on a stable test result at 7000 rpm and 5 mm. Figure 4.22 shows the updated cdf at 6500 rpm for both the standard deviations. As shown in the figure, the selected test does not affect the cdf at 6500 rpm for a standard deviation equal to 0.5 mm. The cdf is the same as the prior cdf as shown in Figure 4.8. However, for the standard deviation of 0.25 mm, the cdf at 6500 rpm shows a probability of stability equal to unity at 2 mm. Figure 4.23 shows the updated posterior cdf given a stable test result at 7000 rpm, 5 mm using random walks generated using a standard deviation of 0.5 mm (left) and 0.25 mm (right). The algorithm for selection of test points was repeated using the random walks generated with a standard deviation of 0.25 mm. Figure 4.24 shows a comparison of the updated posterior cdf after 20 tests for both cases. The algorithm converges to the same optimum operating point in both instances.

A specific criterion for selecting the standard deviation of the step size is not presented here. However, trends have been observed. A higher standard deviation yields walks that are more volatile in the domain. This increases the number of remaining walks after each update (i.e., path filtering) using a test result and reduces

the extent to which a test affects the cdf at all speeds in the domain. As shown in Figure 4.22, a standard deviation of 0.5 mm does not change the cdf at 6500 rpm given a stable test at (7000 rpm, 5 mm). Therefore, a higher standard deviation provides a more conservative representation of the stability boundary.

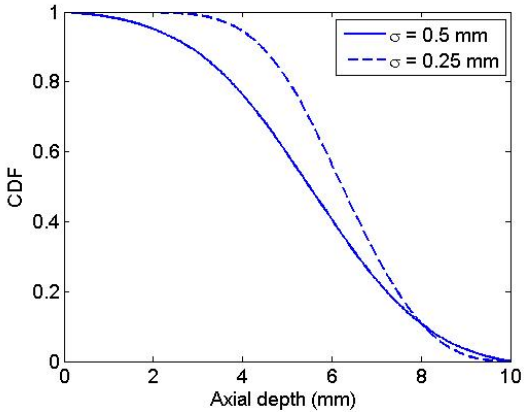

Figure 4.22: The updated cdf at 6500 rpm given a stable test at 7000 rpm, 5 mmwith standard deviations of 0.5 mm and 0.25 mm for the random walk generation.

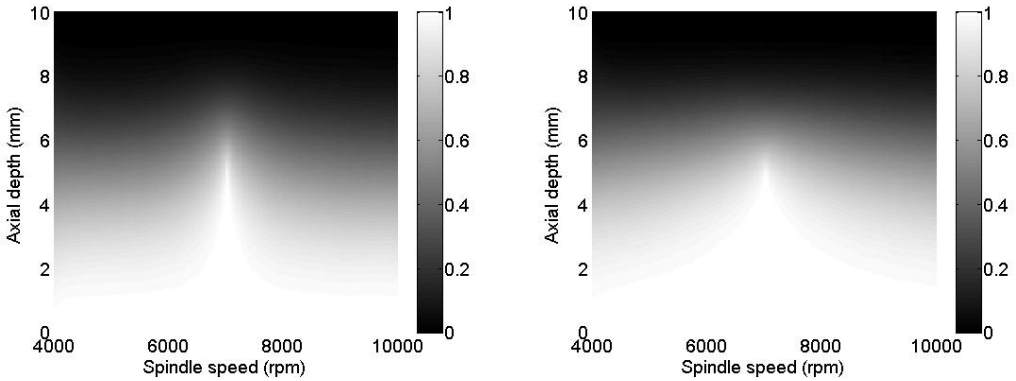

Figure 4.23: Updated posterior cdf given a stable test result at 7000 rpm, 5 mm for random walks generated using standard deviations of 0.5 mm (left) and 0.25 mm (right).

The effect of the spindle speed-axial depth domain on the test point selection was also evaluated. The Bayesian updating procedure using random walks was repeated with a spindle speed domain from 4000 rpm to 8000 rpm. The test point selection was based on the value of information approach. Eight experiments were performed and

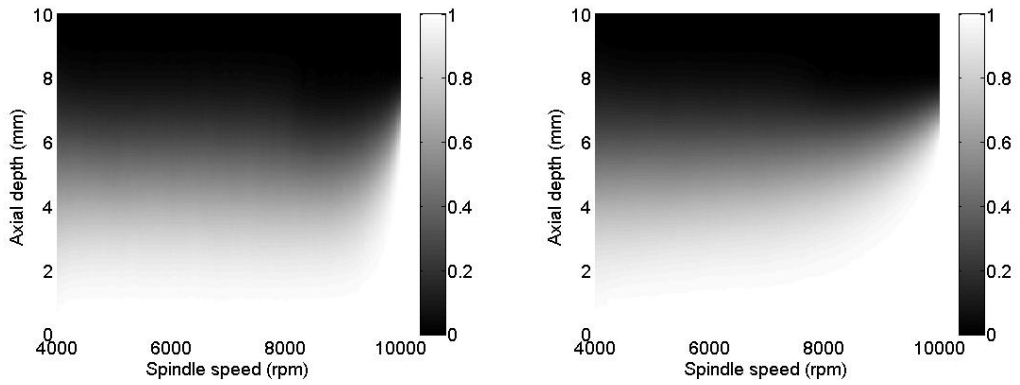

Figure 4.24: Updated posterior cdf after 20 tests using random walks generated with standard deviations of 0.5 mm (left) and 0.25 mm (right).

the test result, stable or unstable, was determined based on the analytical stability lobe shown in Figure 4.21. Table 4.4 shows the test points determined using the value of information approach. Figure 4.25 shows the test point selection and the analytical stability lobes; 'o' represents a stable cut and 'x' represents an unstable cut. Figure 4.26 shows the updated posterior cdf after eight tests. Using the value of information approach, the random walk method is robust and insensitive to the selected spindle speed - axial depth of cut domain. Although the nature of cdf is discrete, it does not affect the optimal operating point selection. Note that the optimal operating point was decided as the one which is known to be stable with certainty and the profit is the highest.

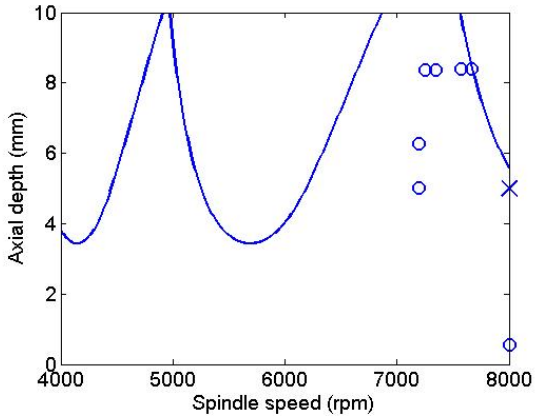

Figure 4.25: Test point selection compared with the analytical stability lobes.

Table 4.4: Experimental test points and results for spindle speed range of 4000 rpm to 8000 rpm.

Test number	Spindle speed (rpm)	Axial depth (mm)	Stability result
1	8000	0.54	stable
2	8000	5.01	unstable
3	7197	5.01	stable
4	7197	6.25	stable
5	7250	8.36	stable
6	7334	8.36	stable
7	7571	8.36	stable
8	7665	8.36	stable

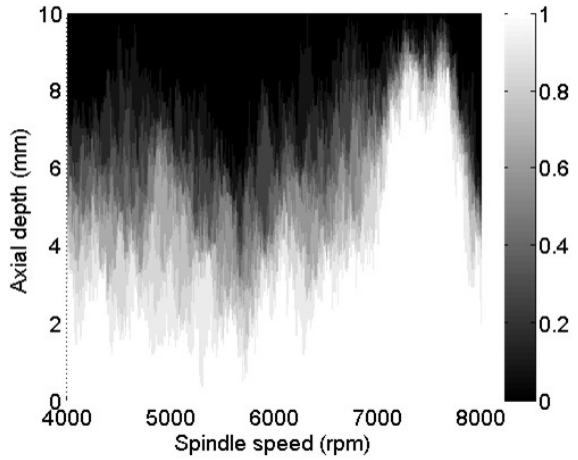

Figure 4.26: Posterior cdf of stability after eight tests at a spindle speed range of 4000 rpm to 8000 rpm.

4.6 Conclusions

Bayesian inference using a random walk approach for stability prediction in milling was presented. The optimal test point selection was based on the value of information method. The motivation for implementing a Bayesian inference model was: 1) a Bayesian inference model enables a prediction which considers both theory and experimental results; and 2) when using a Bayesian inference model, experiments can be chosen such that the expected value added by performing the experiment is maximized.

For the study presented here, no prior knowledge of the machining dynamics was assumed. Only stability test results were considered and the optimal experimental test point was selected using the value of information approach. Bayesian inference combined with decision analysis enables a dollar value to be placed on the information gained from an experiment prior to performing it. The stability updating was completed using random walks generated in the spindle speed - axial depth of cut domain. The feature to be machined was taken to be a pocket. The value of information approach selects a test point which adds maximum value to profit taking into account the cost of machining the selected feature. The test points converged to the optimal operating point even without knowledge of the system dynamics. The approach is robust and insensitive to the spindle speed - axial depth of cut domain.

CHAPTER 5: APPLICATION TO PROCESS DAMPING IN MILLING

This chapter describes a value of information-based experimental design method that uses Bayesian inference for belief updating. The application is process damping coefficient identification in milling. An analytical process damping algorithm is used to model the prior distribution of the stability boundary (between stable and unstable cutting conditions). The prior distribution is updated using experimental results via Bayesian inference. The updated distribution of the stability boundary is used to determine the posterior process damping coefficient value. A value of information approach for experimental test point selection is then demonstrated which minimizes the number of experiments required to determine the process damping coefficient. Subsequent experimental parameters are selected such that the percent reduction in the standard deviation of the process damping coefficient is maximized. The method is validated by comparing the process damping posterior values to residual sum of squares results using a grid-based experimental design approach. Results show a significant reduction in the number of experiments required for process damping coefficient parameter determination. The advantages of using the value of information approach over the traditional design of experimental methods are discussed.

5.1 Introduction

Traditional design of experiment (DOE) approaches, such as factorial design, response surface methodology, and Taguchi orthogonal arrays, find widespread applications in engineering testing. DOE is used to reduce input parameter uncertainty, evaluate the effects and interactions of input parameters on the output, and test hypotheses [50, 51]. The goal is to optimize the number of experiments required

to achieve a desired output. In this chapter, a value of information method for experimental selection using Bayesian inference is described to reduce input parameter uncertainty. The selected application is experimental identification of the process damping coefficient in milling. Value of information is defined as the expected profit before testing minus the profit after testing or, in terms of cost, the cost prior to testing minus the expected cost after testing.

The fundamental principle governing the value of information method is that an experiment is only worthwhile if the value gained from the experiment is more than the cost of performing the experiment [16]. Therefore, the experimental test point is selected which adds the most (expected) value. Note that, while the value of information uses expected value after testing, it is calculated before actually performing the test. The approach considers the importance of uncertainty reduction to the decision maker by assigning a value to the information gained from an experiment [17]. Experimental design using value of information takes into account the probabilistic nature of the uncertainties along with their effect on the output [13].

In this study, the value of information method is used to design experiments for model parameter uncertainty reduction. Therefore, the value of information is modified as parameter uncertainty, expressed in terms of the standard deviation, before testing minus the expected uncertainty after testing. Note that the value after testing calculation depends on the current state of information. Therefore, the value of information cannot be determined by any method which does not explicitly take into account the state of information [16]. To this effect, Bayesian inference is a formal and normative method of combining experimental evidence with the current state of information to determine updated beliefs regarding an uncertain variable. Coupling Bayesian inference with models enables a value to be placed on the information gained from an experiment prior to performing it.

The value of information method for experimental design has two distinct advan-

tages over the traditional (statistical) DOE. First, statistical DOE does not consider the value of uncertainty reduction in experimental point selection. As noted, the experimental design can be optimized based on maximum value added to the current state of information. Second, the value of information can be used as a stopping criterion for performing additional experiments. If the expected cost of performing an experiment is more than the expected value to be gained from the experiment, it is not recommended that the experiment be completed. For example, the user can decide that an experiment is worthwhile only if there is at least a 10% reduction in the standard deviation of the input parameter, which is the cost of performing the experiment. This implies that if the value of information for an experiment is less than 10%, it is not worthwhile to perform the experiment. Traditional DOE typically requires a fixed number of experiments which are decided prior to any testing.

The remainder of the chapter is organized as follows. Section 5.2 describes the process damping phenomenon in milling. Section 5.3 summarizes a grid-based experimental design approach to identify the process damping coefficient using a residual sum of squares (RSS) method. The experimental setup and results are provided. Section 5.4 describes the contrasting Bayesian inference procedure for updating process damping coefficient distributions. Section 5.5 describes the value of information method for experimental design. Section 5.6 provides conclusions.

5.2 Process Damping in Machining Stability Analysis

The analytical stability lobe diagram offers an effective predictive capability for selecting stable chip width-spindle speed combinations in machining operations [1, 2, 52, 53]. However, the increase in allowable chip width provided at spindle speeds near integer fractions of the system's dominant natural frequency is diminished substantially at low spindle speeds where the stability lobes are closely spaced. For these low speeds, the process damping effect can serve to increase the chatter-free chip widths. This increased stability at low spindle speeds is particularly important for hard-to-

machine materials that cannot take advantage of the higher speed stability zones due to prohibitive tool wear at high cutting speeds. Many researchers have investigated process damping in turning and milling operations. Seminal studies were carried out by Wallace and Andrew [54], Sisson and Kegg [55], Peters et al. [56], and Tlusty [41]. It was suggested by this early work that interference contact between the flank of the cutting tool and wavy cutting surface contributes to the process damping phenomenon. The increased use of hard-to-machine alloys has driven recent efforts to accurately predict process damping behavior. Wu developed a model in which plowing forces present during the tool-workpiece contact are assumed to be proportional to the volume of interference between the cutter flank face and undulations on the workpiece surface in turning [57]. Elbestawi and Ismail [58], Lee et al. [59], Huang and Wang [60], and Ahmadi and Ismail [61] extended Wu's force model to milling operations. Budak and Tunc [62] and Altintas et al. [63] experimentally identified different dynamic cutting force models to include process nonlinearities and incorporate process damping. Tyler and Schmitz [64] described an analytical approach to establish the stability boundary that includes process damping effects in turning and milling operations using a single process damping coefficient. These studies described process damping as energy dissipation due to interference between the cutting tool clearance face and machined surface during relative vibrations between the tool and workpiece. It was shown that, given fixed system dynamics, the influence of process damping increases at low spindle speeds because the number of undulations on the machined surface between revolutions/teeth increases, which also increases the local slope of the wavy surface. This, in turn, leads to increased interference and additional energy dissipation.

5.2.1 Process Damping Description

To describe the physical mechanism for process damping, consider a tool moving on a sine wave while shearing away the chip [10]; see Figure 5.1. Four locations are

identified: 1) the clearance angle, γ, between the flank face of the tool and the work surface tangent is equal to the nominal relief angle for the tool; 2) γ is significantly decreased and can become negative (which leads to interference between the tool's relief face and surface); 3) γ is again equal to the nominal relief angle; and 4) γ is significantly larger than the nominal value.

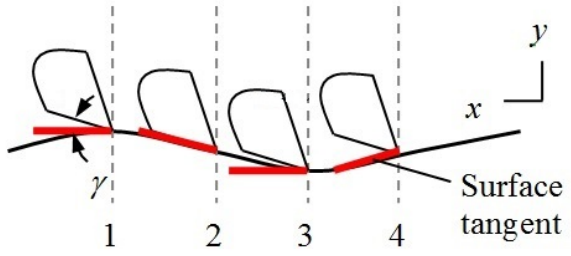

Figure 5.1: Physical description of process damping. The clearance angle varies with the instantaneous surface tangent as the tool removes material on the sinusoidal surface.

At points 1 and 3 in Figure 5.1, the clearance angle is equal to the nominal value so there is no effect due to cutting on the sinusoidal path. However, at point 2 the clearance angle is small (or negative) and the thrust force in the surface normal direction is increased. At point 4, on the other hand, the clearance angle is larger than the nominal and the thrust force is decreased. Because the change in force caused by the sinusoidal path is 90 degree out of phase with the displacement and has the opposite sign from velocity, it is considered to be a viscous damping force (i.e., a force that is proportional to velocity). Given the preceding description, the process damping force, Fd, in the y direction can be expressed as a function of velocity, $\dot{y}$, chip width, b, cutting speed, V, and a process damping constant C [64]. See Eq. 5.1

$$F_d = -C\frac{b}{V}\dot{y} \tag{5.1}$$

Because the new damping value is a function of both the spindle speed-dependent limiting chip width and the cutting speed, the b and Ω vectors must be known in order

to implement the new damping value. This leads to a converging stability analysis that incorporates process damping. The following steps are completed for each lobe in the stability lobe diagram:

- the analytical stability boundary is calculated with no process damping ($C = 0$) to identify initial b and Ω vectors
- these vectors are used to determine the corresponding new damping coefficient vector (which includes both the structural damping and process damping, $C \neq 0$)
- the stability analysis is repeated with the new damping coefficient vector to determine the updated b and Ω vectors
- the process is repeated until the stability boundary converges.

The automated algorithm description and validation are described in [64]. Figure 5.2 illustrates a comparison between stability lobes diagrams developed with and without process damping for a selected C value.

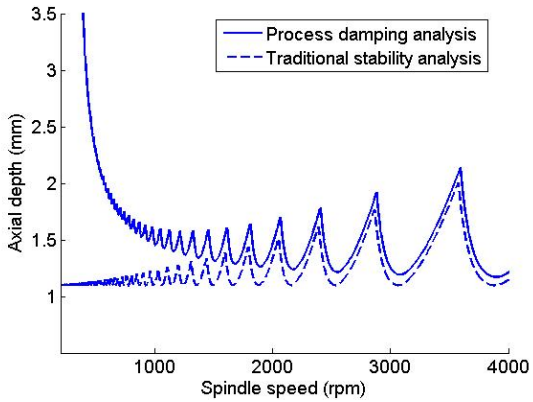

Figure 5.2: Comparison between stability lobes with and without process damping.

5.3 Grid-based Experimental Design

As a first step in this study, the objective was to determine the process damping coefficient for milling with a particular tool-workpiece pair. Note that the experimental results were binary in nature; an experiment at an axial depth-spindle speed combination were either stable or unstable. Based on the stable/unstable cutting test results, a single variable residual sum of squares (RSS) estimation was applied to identify the process damping coefficient that best represented the experimental limiting axial depth of cut, b_{lim}. The spindle-speed dependent experimental stability limit, b_i, was selected to be the midpoint between the stable and unstable points at the selected spindle speed. The sum of squares of residuals is given by Eq. 5.2, where f(Ω_i) is the analytical stability boundary and j is the number of test points. A range of process damping coefficients was selected and the RSS value was calculated for each corresponding stability limit. The C value that corresponded to the minimum RSS value was selected to identify the final stability boundary for all test conditions [64].

$$RSS = \sum_{i=1}^{j} \left(b_i - f(\Omega_i)\right)^2 \tag{5.2}$$

A first step in traditional DOE is to select the factors and number of levels. The factors influencing stability are axial depth and spindle speed for a given radial depth of cut. The process damping zone is identified here as the region where spindle speed is less than 1200 rpm. The spindle speed range extended from 200 rpm to 1100 rpm and was divided into 10 levels. The axial depth range for experiments was divided in five levels from 1 mm to 3 mm. Therefore, a grid of test points at low spindle speeds was selected to investigate the process damping behavior. The experimental design used here was full factorial; an experiment was performed at every grid point (for a total of 50 experiments). Note that alternative methods, such as randomized or Latin hypercube experimental design, will not work in this case because the RSS

method requires both a stable and unstable result at each spindle speed. The number of experiments can be reduced by decreasing the number of levels in the spindle speed and axial depth range. However, since the process damping behavior in the range selected is not known, the preselected levels were deemed appropriate.

5.3.1 Results

In order to provide convenient control of the system dynamics, a single degree-of-freedom, parallelogram leaf-type flexure was constructed to provide a flexible foundation for individual AISI 1018 steel workpieces; see Figure 5.3. Because the flexure compliance was much higher than the tool-holder-spindle-machine, the stability analysis was completed using only the flexure's dynamic properties. A radial immersion of 50% and a feed per tooth of 0.05 mm/tooth was used for all conventional (up) milling tests. An accelerometer (PCB Piezotronics model 352B10) was used to measure the flexure's vibration during cutting. The frequency content of the accelerometer signal was used in combination with the machined surface finish to establish stable/unstable performance, i.e., cuts that exhibited significant frequency content at the flexure's compliant direction natural frequency, rather than the tooth passing frequency and its harmonics, were considered to be unstable.

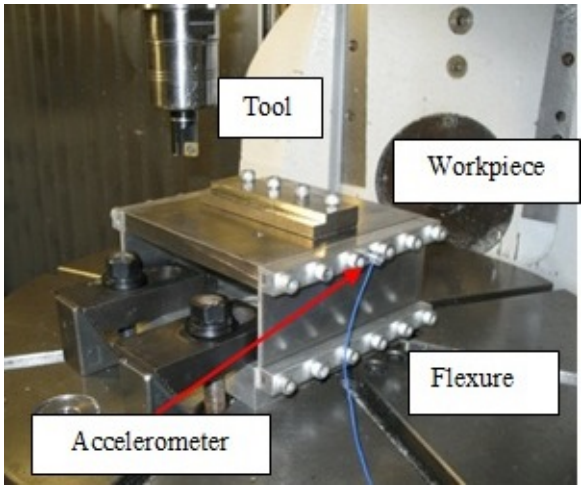

Figure 5.3: Setup for milling stability tests. An accelerometer was used to measure the vibration signal during cutting.

Table 5.1: Comparison of process damping and cutting force coefficients for different relief angle cutters.

Releif angle (degree)	C N/m	K_t N/mm^2	K_n N/mm^2
11	2.5×10^5	2111.2	1052.6
15	3.3×10^5	2234.9	1188.2

As noted, stability tests were performed at all 50 grid points. The results of the coefficient identification method are depicted in Figure 5.4 for an 18.54 mm diameter, single-tooth inserted endmill with a 15 degree relief angle. For the same milling conditions and system dynamics, the process was repeated for a 19.05 mm diameter, single-tooth inserted endmill with an 11 degree relief angle. The stability boundary for this experiment is provided in Figure 5.5. The corresponding process damping coefficients and cutting force coefficients in the tangential, t, and normal, n, directions (as defined in [10]) are provided in Table 5.1.

The cutting force coefficients were identified using a linear regression on the mean forces in the x (feed) and y directions at different feed per tooth values. The cutting force was measured under stable cutting conditions using a cutting force dynamometer (Kistler model 9257B). For these tests, the insert wear was monitored using in-process optical flank wear measurements and the insert was replaced if the wear exceeded a predetermined value. From Figures 5.4 and 5.5 it can be observed that numerous cutting tests were used to identify the process damping coefficient for a particular cutting operation. This can be costly if there are multiple cutter geometries or workpiece materials for which stability boundaries need to be constructed. The following section details a Bayesian updating method for optimizing the experimental test selection and determining the process damping coefficient more efficiently.

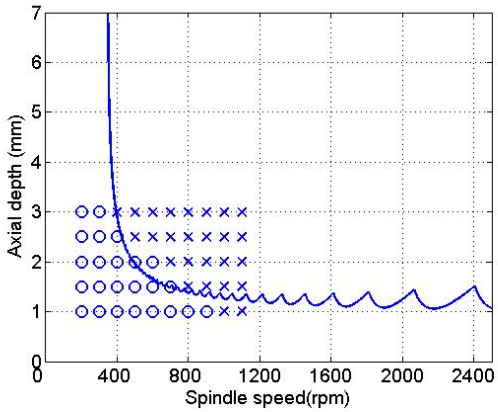

Figure 5.4: Up milling stability boundary for 50% radial immersion, 18.54 mm diameter, 15 degree relief angle, low wear milling tests using the 228 Hz flexure setup ($C = 2.5 \times 10^5$ N/m).

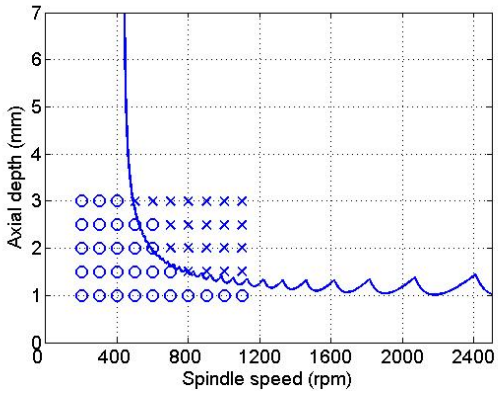

Figure 5.5: Up milling stability boundary for 50% radial immersion, 19.05 mm diameter, 11 degree relief angle, low wear milling tests using the 228 Hz flexure setup ($C = 3.3 \times 10^5$ N/m).

5.4 Bayesian Updating of the Process Damping Coefficient

This section describes the Bayesian updating method for process damping coefficient identification. The updating was performed using the experimental results shown in Figures 5.4 and 5.5. In these figures, uncertainty exists in the true location of the stability boundary due to the uncertainties/assumptions in the process damping model and its parameters as well as factors that are not known. Therefore, the stability boundary may be modeled as a cumulative probability distribution rather than a deterministic boundary. From a Bayesian standpoint, an uncertain variable

is treated as random and is characterized by a probability distribution. Bayesian inference is a normative and formal method of belief updating when new information (e.g., experimental stability results) is made available. The stability boundary prediction proceeds by generating n sample paths, each of which may represent the actual stability boundary with some probability. For the prior (or initial belief), each path is assumed to be equally likely to be the true stability limit. Therefore, the probability that each sample path is the true stability limit is $1/n$. These sample paths are used as the prior in applying Bayesian inference. Bayesian updating was used to update the prior probability of sample paths given experimental result, and therefore, the process damping coefficient distribution. The entire methodology is defined as Bayesian updating using a random walk approach. Bayes' rule is given by Eq. 5.3.

$$\mathrm{P}(\textit{path} = \textit{true stability limit} | \textit{test result}) \propto$$
$$\mathrm{P}(\textit{test result} | \textit{path} = \textit{true stability limit}) \mathrm{P}(\textit{path} = \textit{true stability limit})$$

Here P(*path = true stability limit*) is the prior probability which, before any testing, is equal to $1/N$ for any sample path and P(*test result | path = true stability limit*) is the likelihood of obtaining the test result given the true stability limit. Their products yields the posterior stability limit probability given the test result, P(*path = true stability limit | test result*). In practice, the probability of the test result, P(*test result*), may be used to normalize the posterior probability (by dividing the right hand side of Eq. 5.3 by this value). The sample paths are generated by randomly sampling from the prior distributions of the K_t, K_n, and C values and calculating a stability boundary for each set.

5.4.1 Establishing the Prior

The random sample stability limits were generated by sampling from the prior distributions of K_t, K_n, and C. To demonstrate the approach, the 18.54 mm diameter, 11 degree relief angle tool is considered. The distribution of C is not known and has to be determined. The prior marginal distribution of C was selected to be the uniform distribution U(0.5×10^5, 10×10^5) N/m, where the values in the parenthesis specify the lower and upper limits on C, respectively. A uniform distribution denotes that it is equally likely for the value of C to take any value between 0.5×10^5 N/m and 10×10^5 N/m and represents a non-informative case where little prior knowledge of the variable is available. Recall that the value of C for the 18.54 mm diameter, 15 degree relief angle tool was found to be 2.5×10^5 N/m using the RSS method (see Figure 5.4). The values of K_t and K_n were calculated using a linear least squares fit to the mean forces in the x (feed) and y directions at different feed per tooth values. The mean and standard deviation of the force coefficients were calculated from three measurement sets. Based on this data, the marginal prior distributions of the force coefficients were K_t = N(2111.2, 78.3) N/mm^2 and K_n = N(1052.6, 27.9) N/mm^2, where N denotes a normal distribution and the terms in parenthesis specify the mean and standard deviation, respectively. The prior distributions of K_t, K_n, and C were assumed to be independent of each other. Although, K_t and K_n are most likely correlated, an independent assumption is chosen because it is conservative. Random samples (1×10^4) are drawn from the prior distributions and the stability limit was calculated for each sample. The probability that each sample stability limit is the true stability limit is 1×10^-4. Recall that for the prior, each stability limit was assumed to be equally likely to be the true limit. Figure 5.6 shows the prior cumulative distribution function (cdf) for probability of stability. The maximum possible axial depth of cut possible was defined as 7.5 mm based on the tool's cutting edge length. Figure 5.7 and 5.8 show the probability of stability, p(stability), as a function of

axial depth at 400 rpm and 1000 rpm, respectively. As expected, the probability of stability decreases at higher axial depths at a given spindle speed. For example, the probability of stability at 1 mm is 1 at both speeds, while the probability of stability for an axial depth of 4 mm is 0.7 at 400 rpm and only 0.25 at 1000 rpm.

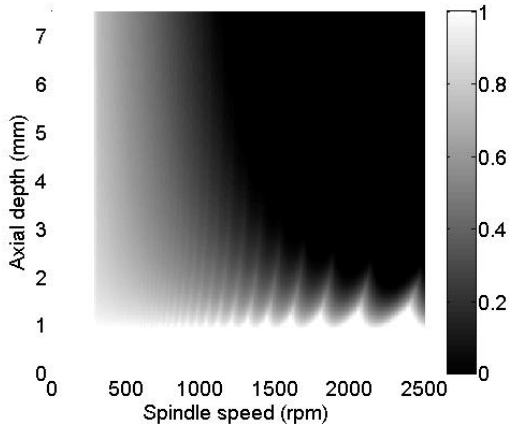

Figure 5.6: Prior cdf of stability. The gray color scale represents the probability of stability for any spindle speed, axial depth combination (1/white is likely to be stable, while 0/black is unlikely to be stable).

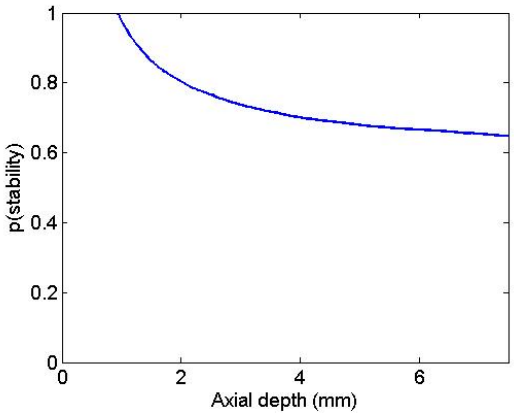

Figure 5.7: Probability of stability at 400 rpm.

5.4.2 Likelihood Function

The likelihood function describes how likely the test result is given that the sample path is the true stability limit. The likelihood function incorporates the uncertainty

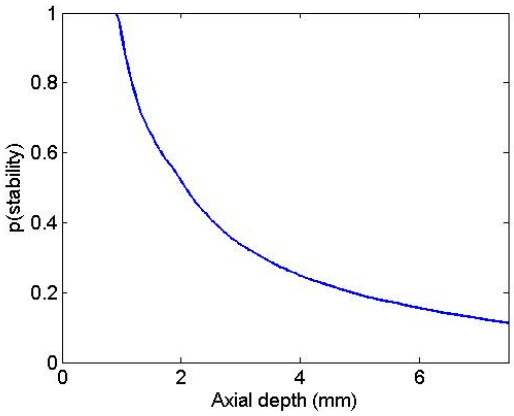

Figure 5.8: Probability of stability at 1000 rpm.

in the process damping model and, therefore, the stability boundary. To illustrate, consider an experiment completed at a spindle speed of 1000 rpm and an axial depth of 3 mm. A stable result indicates that the test result is equally likely for all paths that have an axial depth greater than 3 mm at 1000 rpm; they are assigned a likelihood of unity. On the other hand, a stable result at 3 mm is unlikely for all paths with an axial depth less than 3 mm at 1000 rpm. Note that the stable result is unlikely, but not impossible for such paths, giving a nonzero likelihood. As shown in Figures 5.4 and 5.5, stable points may lie above the boundary and unstable points may lie below the boundary since there is uncertainty in the stability boundary location. Note that the test result is increasingly unlikely for values less than 3 mm at 1000 rpm. For example, the test result is more unlikely for a path that has a value of 1 mm at 1000 rpm relative to a path that has a value of 2.5 mm at 1000 rpm. Therefore, the likelihood is a one-sided function. The likelihood function for a stable result is described by Eq. 5.4.2.

$$l = \begin{cases} e^{\frac{-(b-b_{test})^2}{k}} & b < b_{test} \\ 1 & b \geq b_{test} \end{cases}$$

The likelihood function is expressed as a non-normalized normal distribution,

where the parameter $k = 2\sigma^2$ and σ is the standard deviation in the axial depth due to the model uncertainty. The value of σ was taken to be 0.5 mm. Similarly, an unstable cut indicates that test result is likely for all paths that have an axial depth value less than 3 mm at 1000 rpm, while it is unlikely for all paths that have a value greater than 3 mm. Although a Gaussian kernel is used in this study, it can be any function defined by the user based on his/her beliefs. The likelihood function for an unstable result is provided in Eq. 5.4.2. Figure 5.9 displays the likelihood function for a stable result at 3 mm and Figure 5.10 shows the likelihood for an unstable result.

$$l = \begin{cases} e^{\frac{-(b-b_{test})^2}{k}} & b \geq b_{test} \\ 1 & b < b_{test} \end{cases}$$

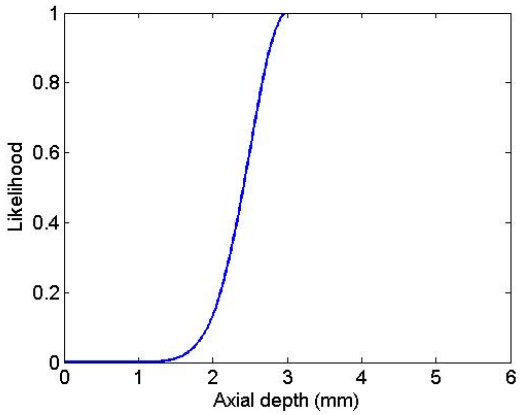

Figure 5.9: Likelihood given a stable result at 3 mm.

5.4.3 Bayesian Updating

The posterior probability of each path is obtained by multiplying the prior and likelihood and normalizing such that the sum of all probabilities is equal to unity. The posterior probabilities of sample paths are used to calculate the posterior distribution of the process damping and cutting force coefficients. The experimental results shown in Figure 5.4 were used to update the prior cdf of stability. For each experiment, the

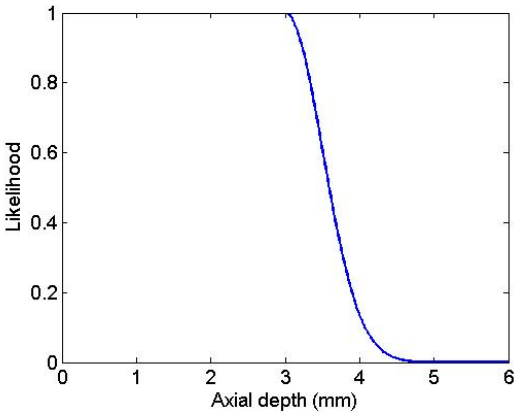

Figure 5.10: Likelihood given a unstable result at 3 mm.

likelihood function was calculated using Eqs. 5.4.2 and 5.4.2 for a stable and unstable result, respectively. For multiple updates, the prior after the first update becomes the posterior after the second update and so on. Figure 5.11 shows the posterior cdf given the experimental results. Stable results are denoted as 'o' and unstable results as 'o'. Figure 5.12 and Figure 5.13 shows the prior and posterior probability of stability at 400 rpm and 1000 rpm, respectively.

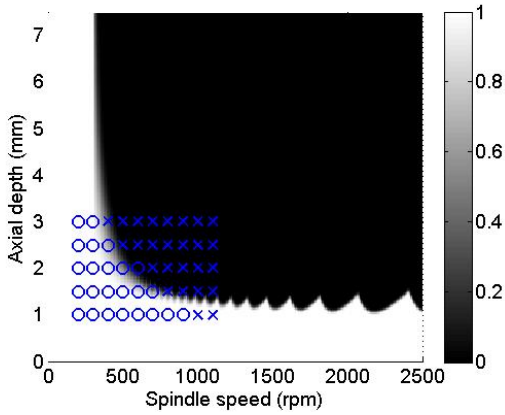

Figure 5.11: Posterior cdf of stability. Stable results are denoted as 'o' and unstable results as 'x'.

After each update, the posterior mean and standard deviation of C was calculated using Eqs. 5.3 and 5.4.

$$\mu_C = \sum CP(C) \tag{5.3}$$

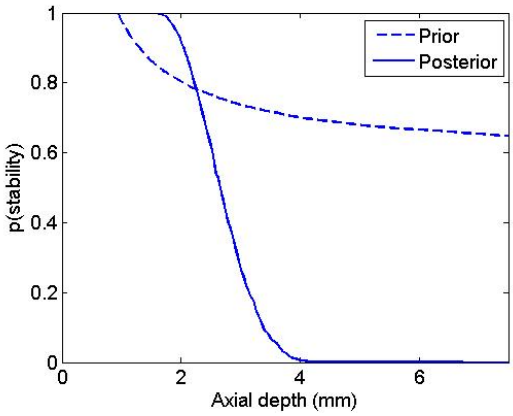

Figure 5.12: Prior and posterior probability of stability at 400 rpm.

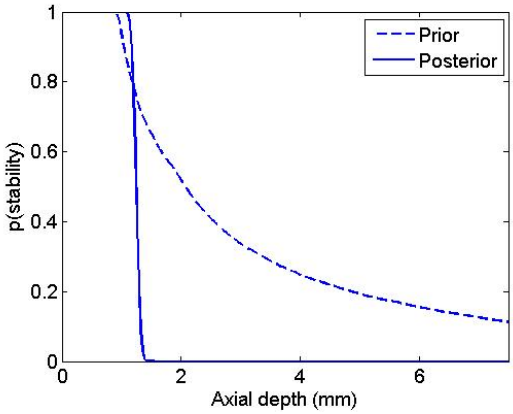

Figure 5.13: Prior and posterior probability of stability at 1000 rpm.

$$\sigma_C = \sum (C - \mu_C)^2 P(C) \tag{5.4}$$

In these equations, μ_C and σ_C are the mean and standard deviation of C, respectively, and P(C) is the probability of the sample stability limit. Recall that each sample stability limit is generated from a sample of (K_t, K_n, C). The probability of a sample stability limit is equal to the probability that the sample corresponds to the true limit.

For the prior, each sample stability limit was assumed to be equally likely to be the true limit; this implies that each (K_t, K_n, C) sample was equally likely to be the true combination. The updated probability of each sample stability limit gives the updated probability of the underlying (K_t, K_n, C) sample to be the true combination. The

updated posterior probabilities of sample paths were used to calculate the posterior mean and standard deviation of C using Eqs. 5.3 and 5.4, respectively. Figures 5.14 and 5.15 show the progression of μ_C and σ_C as a function of the number of tests. The μ_C and σ_C values after 50 tests were 2.49×10^5 N/m and 0.30×10^5 N/m, respectively. The value of C from the RSS method was 2.5×10^5 N/m. Figures 5.14 and 5.15 show a convergence in μ_C and σ_C to the final values after the 18th test. The μ_C and σ_C values after the 18th test were 2.41×10^5 N/m and 0.34×10^5 N/m, respectively. This is due to the first unstable result at 400 rpm, 3 mm axial depth preceded by a stable result at 400 rpm, 2.5 mm axial depth. A stable result at a 2.5 mm axial depth and an unstable result at a 3 mm axial depth imply that there is a high probability that the true stability limit is between the two values. Also, note that the values remain approximately constant after subsequent updates.

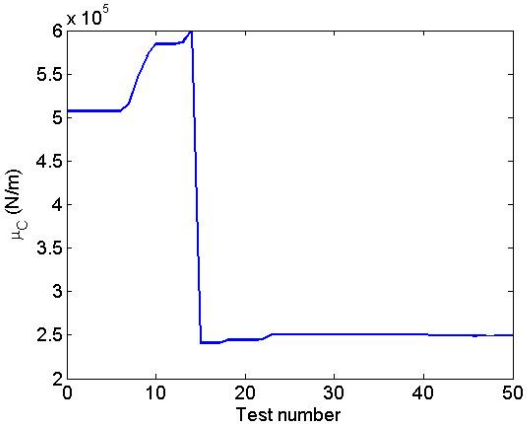

Figure 5.14: μ_C as a function of the number of tests.

The updating procedure was repeated for the 19.05 mm diameter, 11 degree relief angle tool. The prior marginal distribution of the force coefficients were K_t = N(2234.9, 107.0) N/mm^2 and K_n = N(1188.2, 40.5) N/mm^2. The prior marginal distribution of C was again selected to be uniform, U(0.5×10^5, 10×10^5) N/m, and the coefficients were assumed to be independent of each other. The updating procedure was performed using the experimental results shown in Figure 5.5. Figure 5.16

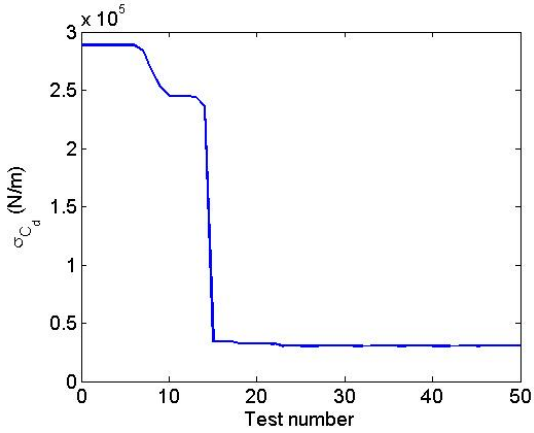

Figure 5.15: σ_C as a function of the number of tests.

shows the posterior cdf given experimental results. Figures 5.17 and 5.18 show the progression of μ_C and σ_C as a function of the number of tests. The μ_C and σ_C values after 55 tests were 3.63×10^5 N/m and 0.38×10^5N/m, respectively. The C value from the RSS method was 3.3×10^5 N/m. These results show good agreement between the posterior mean C and the value obtained using the RSS method. The advantage of using Bayesian inference over RSS is that the uncertainty in C can also be calculated. As a result, the stability boundary is not deterministic, but characterized by a cumulative probability distribution. In addition, Bayesian inference enables the value to be gained from performing an experiment to be calculated; this is described in the next section.

5.5 Experimental Design using a Value of Information Approach

Bayesian updating of the probability of stability and the process damping coefficient was demonstrated. Using experimental results, the probability of each sample stability limit being the true limit was updated. These probabilities were, in turn, used to determine the posterior distribution of the process damping coefficient. The posterior mean agreed with the deterministic value calculated using the RSS method. Note that additional experimental results reduce the uncertainty (or the standard deviation) in the C value. This section describes a value of information approach

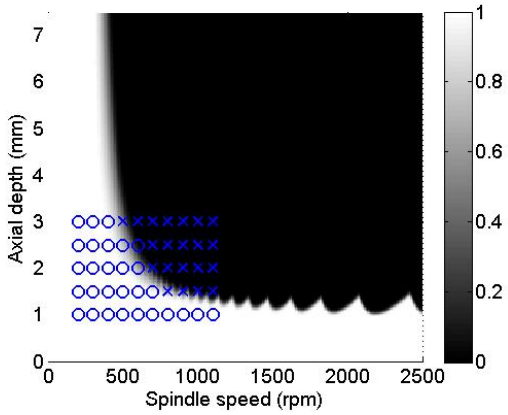

Figure 5.16: Posterior cdf of stability. Stable results are denoted as 'o' and unstable results as 'x'.

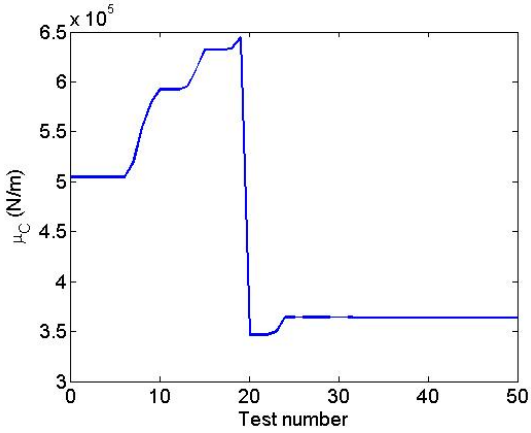

Figure 5.17: μ_C as a function of the number of tests.

for optimal experimental parameter selection. The objective of the experiments is to reduce the uncertainty in the C value. Note that no new information (or reduction in uncertainty) is achieved by obtaining a stable result at a spindle speed, axial depth combination which has a prior probability of stability equal to one. A probability of stability equal to one indicates that all sample paths have a value of axial depth greater than the test axial depth at the test spindle speed. A stable result assigns a likelihood of one to all the sample stability limits, which results in no reduction in the value of σ_C. This is observed in Figures 5.15 and 5.18 for the first five tests. On the other hand, a test at a combination which has a non-zero probability of stability

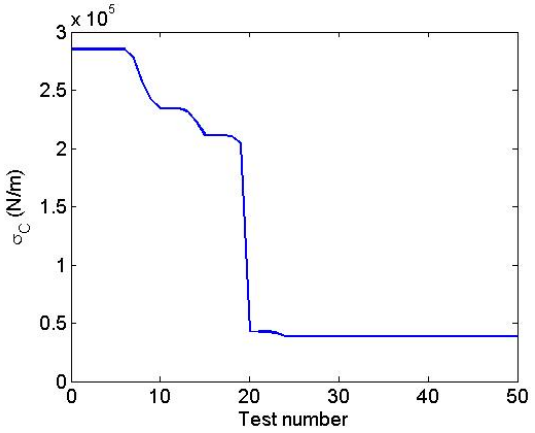

Figure 5.18: σ_C as a function of the number of tests.

will cause a reduction in σ_C due to the small likelihood value assigned to some sample paths.

The information from a test is characterized as an expected percent reduction in the value of σ_C. The experimental parameters are selected where the expected percent reduction in σ_C is maximum. To illustrate, consider four possible experimental (spindle speed, axial depth) combinations: A = (400 rpm, 1.28 mm), B = (1000 rpm, 2.68 mm), C = (1500 rpm, 2.04 mm) and D = (2000 rpm, 1.36 mm). The probability of stability for test points A, B, C and D are 0.9, 0.5, 0.1, and 0.52, respectively (see Figure 5.18).

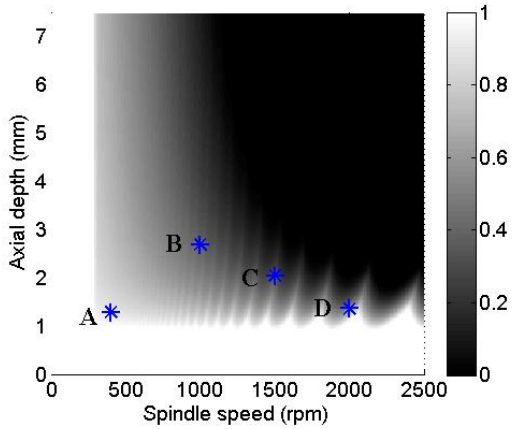

Figure 5.19: Four possible test points.

Table 5.2: Expected percent reduction at test points.

Test	p(stability)	Expected reduction in σ_C
A	0.9	13.8
B	0.51	45.6
C	0.1	14.6
D	0.52	24.9

Consider test point A. Given a stable or unstable result at point A, the posterior probabilities of the sample stability limits is updated using the procedure described previously. The posterior probabilities are used to calculate the values of μ_C of and σ_C via Eqs. 5.3 and 5.4. If the result at point A is stable, the value of σ_C would be 2.72×10^5 N/m. Note that the value of σ_C before any testing was 2.87×10^5 N/m. Therefore, the percent reduction in σ_C would be 5.60. On the other hand, if the result at point A was unstable, the value of σ_C would be 3.47×10^4 N/m giving a percent reduction of 87.9. Recall that point A has a 0.9 probability of being stable. The expected percent reduction in σ_C for point A is calculated as:

(% reduction in σ_C)A = $0.9\times5.60 + 0.1\times87.9 = 13.8$.

The procedure was repeated for points B, C and D. The results are summarized in Table 5.2. As noted, points A and C have a high prior probability of being stable and unstable, respectively. As a result, the expected percent reduction in σ_C for testing at these points is low. On the other hand, points B and D have maximum uncertainty regarding the result, p(stability) 0.5. Also, the distribution (or the uncertainty) in axial depth at point B (1000 rpm) is higher as compared to point D (200 rpm) as seen from Figure 5.19. Therefore, the expected percent reduction is greater for testing at point B than point D.

The (spindle speed, axial depth) domain was divided into a grid with increments of 50 rpm and 0.15 mm. The expected percent reduction in σ_C was calculated at all grid points using the procedure described. The maximum expected percent reduction

was 49.6 at (550 rpm, 7.5 mm) with a probability of stability equal to 0.51. The test result was selected to be unstable based on the stability limit displayed in Figure 5.4. The purpose of using the stability limit in Figure 5.4 to determine the test result was to validate the convergence of the posterior mean and standard deviation of C to the values determined using the original 50 tests. The values of μ_C and σ_C after the first update were 2.53×10^5 N/m and 1.42×10^5 N/m, respectively. The posterior after the first update becomes the prior for the second update. The procedure to calculate value of information was repeated for the second test. The maximum expected percent reduction was 48.3 at (550 rpm, 3.0 mm) with a probability of stability equal to 0.54. The values of μ_C and σ_C after the second update were 3.63×10^5 N/m and 0.79×10^5 N/m, respectively. With each update using experimental result, there is reduction in the σ_C values as seen from the first two experimental results. Therefore, the maximum expected reduction in σ_C will also reduce for every subsequent test. The maximum percentage reduction in the process damping coefficient uncertainty was used as a stopping criterion for doing experiments. It was decided that an experiment is only worthwhile if the expected reduction in σ_C is at least 10.

The procedure was repeated till the maximum expected reduction in σ_C was less than 10. The test results were all based on the stability limit shown in Figure 5.4. As noted, the test points were selected where the expected percent reduction in C was maximum. Figure 5.20 shows the maximum expected percent reduction in C for each test. As seen in the figure, the percent reduction in σ_C is 8.3 for the seventh test. The seventh experiment was performed and the procedure was terminated. Figure 5.21 shows the posterior cdf after seven updates. Stable results are denoted as 'o' and unstable results as 'x'. Table 5.3 lists the experimental test points and the stability results for all seven tests. Figure 5.22 and Figure 5.23 show the progression of μ_C and σ_C as a function of the number of tests. Note that the mean converges to 2.5×10^5 N/m in seven tests as compared to 50 tests as shown in Figure 5.14. An alternate criterion

for stopping is to calculate the percentage reduction in σ_C from the prior (before any testing) value. If the location of the boundary was known with certainty, the value of σ_C would be zero. Therefore, the maximum percentage reduction in σ_C achievable by testing is 100. This value is also referred to as the value of perfect information. The value of perfect information implies that any experimentation is not worthwhile if the cost of experiments exceeds the value of perfect information [16, 17]. The value of perfect information can be calculated *a priori* to decide if any experiments should be performed. However, the user can decide that no additional experimentation is required after a certain percentage reduction in the prior σ_C value (such as 90) is achieved. Figure 5.24 shows the percentage reduction in σ_C from the before testing value as a function of number of tests.

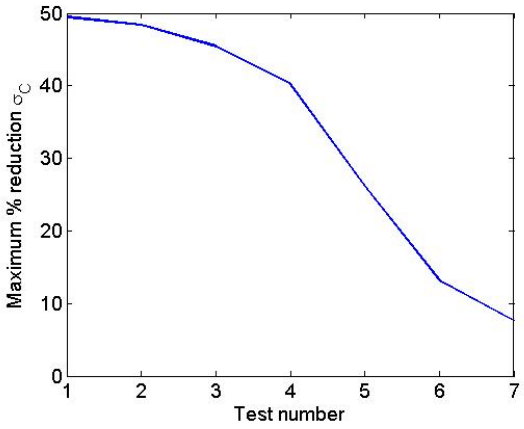

Figure 5.20: Maximum expected percent reduction for each test.

The experimental selection procedure was repeated for the 19.05 mm diameter, 11 degree relief angle tool. Seven tests were performed at points where the expected percent reduction in σ_C was maximum. Figure 5.25 shows the posterior cdf. Stable results are denoted as 'o' and unstable results as 'x'. Figures 5.26 and 5.27 display the progression of μ_C and σ_C as a function of the number of tests. Note that the mean converges to 3.6×10^5 N/m in seven tests.

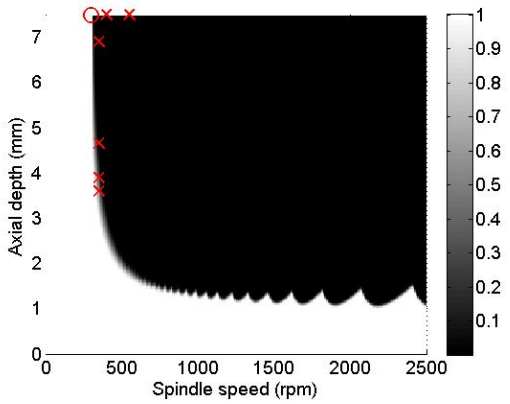

Figure 5.21: Posterior cdf of stability. Stable results are denoted as 'o' and unstable results as 'x'.

Table 5.3: Experimental results

Spindle speed (rpm)	Axial depth (mm)	Result
550	7.5	unstable
300	7.5	stable
400	7.5	unstable
350	6.9	unstable
350	4.65	unstable
350	3.9	unstable
350	3.6	unstable

5.6 Conclusions

A random walk method of Bayesian updating was demonstrated for process damping coefficient identification. The prior sample paths were generated using an analytical process damping algorithm. For the prior, each sample stability limit was assumed to be equally likely to be the true stability limit. The probability of the sample stability limit was then updated using experimental results. The updated probabilities of the sample paths were used to determine the posterior process damping coefficient distribution. A value of information was used to select experimental test points which maximized the expected reduction in the process damping coefficient uncertainty. Results show a significant decrease in the number of tests required.

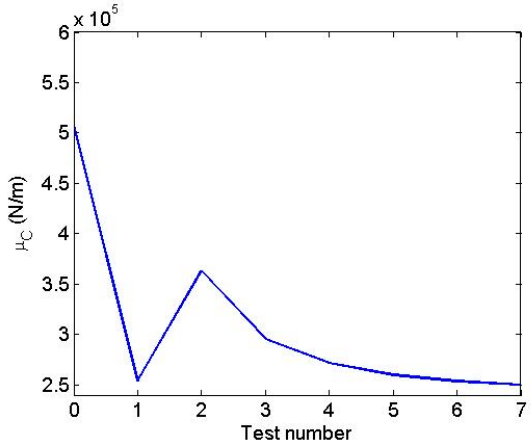

Figure 5.22: μ_C as a function of the number of tests.

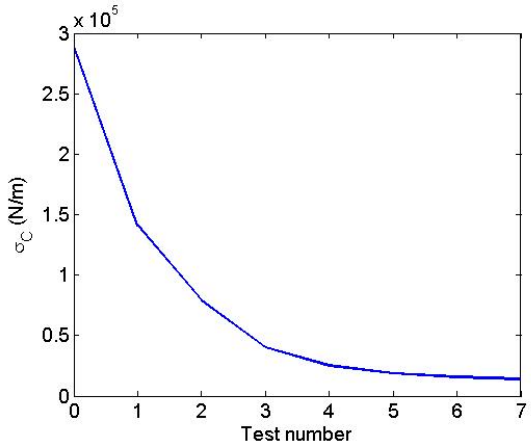

Figure 5.23: σ_C as a function of the number of tests.

The value of information considers the value on uncertainty reduction in selecting the experimental parameters, in addition to serving as a stopping criterion for additional testing.

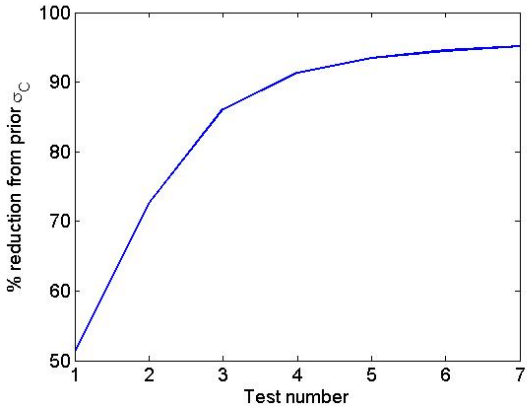

Figure 5.24: Percent reduction in σ_C from the prior value.

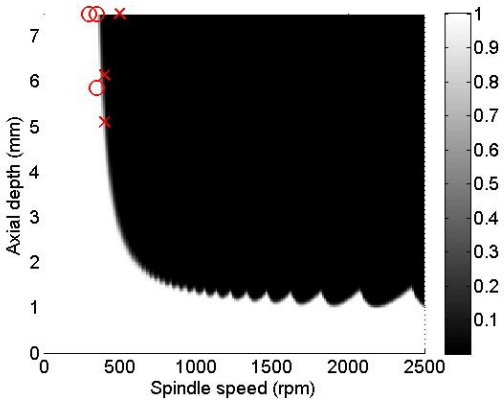

Figure 5.25: Posterior cdf of stability. Stable results are denoted as 'o' and unstable results as 'x'.

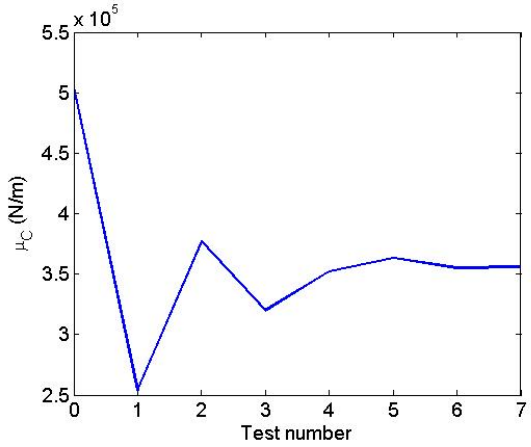

Figure 5.26: μ_C as a function of the number of tests.

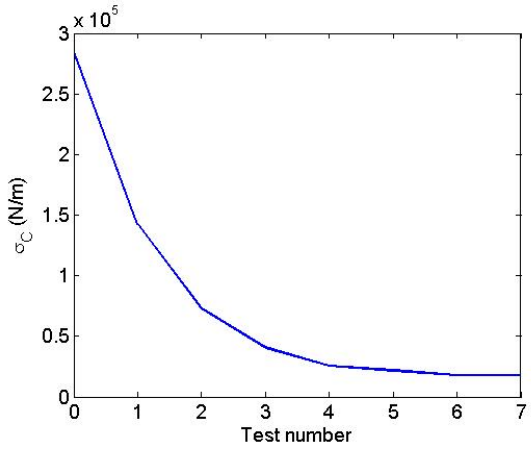

Figure 5.27: σ_C as a function of the number of tests.

CHAPTER 6: APPLICATION TO TOOL LIFE PREDICTIONS

According to the Taylor tool life equation, tool life reduces with increasing cutting speed. The influence of additional factors, such as feed, can also be incorporated in deterministic models. However, tool wear is generally considered a stochastic process with uncertainty in the model empirical constants. In this chapter, Bayesian inference is applied to predict tool life for milling/turning operations using the random walk/random surface methods. For milling, Bayesian inference using a random walk approach is applied to the Taylor tool life model. Tool wear tests are performed using an uncoated carbide tool and AISI 1018 steel work material. Test results are used to update the probability distribution of tool life. The updated beliefs are then applied to predict tool life using a probability distribution. For turning, an extended form of the Taylor tool life equation is implemented that includes the dependence on both cutting speed and feed. Bayesian updating is performed using the random surface technique. Turning tests are completed using a carbide tool and AISI 4137 chrome alloy steel work material. The test results are again applied to update the probability distribution of tool life and the updated beliefs are used to predict tool life.

6.1 Introduction

Tool wear can impose a significant limitation on machining productivity, particularly for hard-to-machine materials. Taylor (1906) first defined an empirical relationship between tool life and cutting speed using the power law [37]:

$$VT^n = C \tag{6.1}$$

where V is the cutting speed in m/min, T is the tool life in minutes, and n and C are constants which depend on the tool-workpiece combination. The constant C is defined as the cutting speed required to obtain a tool life of 1 minute. Tool life is typically defined as the time required to reach a predefined level of wear for a selected feature, such as flank wear width, crater depth, or notch depth depending on the nature of the tool wear. The Taylor tool life equation can be modified to include other effects, such as feed rate [10]:

$$V^p f_r^q C = T \tag{6.2}$$

where f_r is the feed per revolution in mm/rev for turning and C, p, and q are constants which depend on the tool-workpiece combination. The Taylor tool life model is deterministic in nature, but uncertainty exists due to: 1) factors that are unknown or not included in the model; and 2) tool-to-tool performance variation. For these reasons, tool wear is often considered to be a stochastic and complex process and, therefore, difficult to predict.

The remainder of the chapter is organized as follows. Section 6.2 describes Bayesian updating of tool life in milling using the random walk method for the Taylor tool life model given by Eq. 6.1. The experimental setup and tool life predictions are also provided. Section 6.3 describes the random surface method of Bayesian updating for tool life in turning using the Taylor-type tool life model defined by Eq. 6.2. Section 6.4 discusses the influence of the prior and likelihood on tool life predictions. Conclusions are provided in Section 6.6.

6.2 Bayesian Inference of the Taylor Tool Life Model

Bayesian inference provides a rigorous mathematical framework of belief updating about an unknown variable when new information becomes available. In the Taylor tool life model (Eq. 6.1), there is uncertainty in the values of the exponent, n, and

the constant, C. Subsequently, there is uncertainty in the tool life, T. The Taylor tool life curve can be predicted by generating N sample tool life curves, or sample paths, each representing the true tool life curve with an equal probability of $1/N$. The sample paths generated in this way may be used as the prior for Bayesian inference. The prior can then be updated by applying Bayes' rule to experimental test results. For each sample path, Bayes' rule can be written as the following product.

$$\mathrm{P}(\textit{path = true tool life curve}|\textit{test result}) \propto$$
$$\mathrm{P}(\textit{test result}|\textit{path = true tool life curve})\mathrm{P}(\textit{path = true tool life curve})$$

Here P(*path = true tool life curve*) is the prior probability which, before any testing, is equal to $1/N$ for any sample path and P(*test result* | *path = true tool life curve*) is the likelihood of obtaining the test result given the true stability limit. Their products yields the posterior stability limit probability given the test result, P(*path = true tool life curve* | *test result*). In practice, the probability of the test result, P(*test result*), may be used to normalize the posterior probability (by dividing the right hand side of Eq. 6.1 by this value). In this study, the prior sample paths were generated using random samples from an (n, C) joint probability density function (pdf). The initial (prior) n and C distributions were selected based on a literature review. In general, the decision maker should try to use all available information to generate the sample paths. Bayes' rule was then used together with experimental results to update the probability that each sample path was the true tool life curve.

According to Bayes' rule, the posterior distribution is proportional to the (normalized) product of the prior and the likelihood. For multiple experimental results, the posterior after the first update becomes the prior for the second update and so on, where the posterior probabilities of each sample path must be normalized so that the sum of the probabilities for all paths is one. In a milling operation, other factors, such as feed rate and axial/radial depths of cut, may also affect tool life in addition

to the cutting speed. However, since cutting speed is typically the strongest factor, Bayesian updating was performed using Eq. 6.1.

6.2.1 Establishing the Prior

Tool wear experiments were performed using an uncoated carbide (inserted) tool to mill AISI 1018 steel. As noted, a literature review was completed to determine the prior distributions of the Taylor tool life model values, n and C. Stephenson and Agapiou reported the value of n to be in the range of 0.2 to 0.25 for uncoated carbide tools and C to be around 100 m/min for rough finishing of low carbon steels [65]. Kronenberg (1966) reported values of n and C to be in the range of 0.3 to 0.5 and 160 m/min to 200 m/min, respectively, for machining steel with a carbide tool [66]. Creese (1999) reported typical n and C values for machining medium carbon steel with a carbide tool to be 0.32 and 240 m/min, respectively [67]. Cui et al. (2009) performed wear experiments using a carbide insert and 1018 steel workpiece. Values of n and C were reported to be 0.3 and 341 m/min, respectively [68]. In a separate study conducted by the authors, the mean n and C values for the given tool-work piece combination were found to be 0.33 and 600 m/min [69].

Based on these values, the priors for n and C were selected to be uniform distributions with minimum values of 0.3 and 400, respectively, and maximum values of 0.35 and 700, respectively. A uniform distribution implies that it is equally likely for the true n and C value to be anywhere in the selected range. This is expressed as:

$n = \mathrm{U}(0.3,0.35)$ and $C = \mathrm{U}(400,700)$,

where U denotes a uniform distribution and the values in the parentheses identify the minimum and maximum values, respectively.

The relatively large prior distributions of n and C were chosen to improve the probability that the true tool life curve existed within the prior sample paths. The prior n and C distributions were taken as a joint pdf, where the two constants were independent of each other. Random samples were drawn from the prior joint pdf

of n and C and the Taylor tool life curve was calculated for each (n, C) pair; this exercise was repeated 1×10^5 times. The cutting speed was calculated using $V = \pi d\Omega$, where d is the tool diameter (19.05 mm for this study) and Ω is the spindle speed in rev/min (a range of 1500 rpm to 7500 rpm was selected). The prior probability that any sample paths is the true tool life curve for this case is 1×10^{-5}. The collection of prior sample paths could then be used to determine the cumulative density function (cdf) of tool life at any spindle speed in the domain.

To demonstrate the approach, consider a scenario where the (n, C) values can take only 10 different combinations (see Table 6.1). For the prior, it is assumed that any combination is equally likely to be the true combination. This gives a probability of 0.1 for each (n, C) pair since there are 10 possible pairs. The Taylor tool life values are calculated for all spindle speeds in the domain for the 10 (n, C) pairs. Figure 6.1 shows the 10 tool life curves. These are the sample paths or random walks, each generated using a different (n, C) sample. Table 6.1 includes the tool life values for each (n, C) sample at 2500 rpm, 5000 rpm, and 7500 rpm. Figure 6.2 displays the discrete tool life cdf at the three spindle speeds. These cdfs give the probability of tool failure as a function of tool life, p(T). For example, the probability of tool failure for a required tool life of 10 min is effectively zero at 2500 rpm, it is approximately 0.9 at 5000 rpm, and 1 for 7500 rpm. These results match the trend of reduced tool life with increased cutting speed

This procedure was completed for 1×10^5 sample paths that were generated by drawing random samples from the prior joint (n, C) distribution. Figure 6.3 shows the prior cumulative distribution of tool life as a function of spindle speed. The color bar gives the probability of tool failure at a selected tool life for any spindle speed in the domain. As expected, the probability of failure decreases with spindle speed for a particular tool life value.

Table 6.1: Prior probabilities and tool life for sample (n, C) pairs.

Sample	(n, C)	T (2500 rpm) (min)	T (5000 rpm) (min)	T (7500 rpm) (min)	Prior
1	(0.3, 500)	55.8	5.5	1.4	0.1
2	(0.3, 525)	65.7	6.5	1.7	0.1
3	(0.3, 550)	76.7	7.6	2.0	0.1
4	(0.3, 575)	88.9	8.8	2.3	0.1
5	(0.3, 600)	102.5	10.2	2.6	0.1
6	(0.35, 500)	31.4	4.3	1.4	0.1
7	(0.35, 525)	36.1	5.0	1.6	0.1
8	(0.35, 550)	41.2	5.7	1.8	0.1
9	(0.35, 575)	46.8	6.5	2.0	0.1
10	(0.35, 600)	52.9	7.3	2.3	0.1

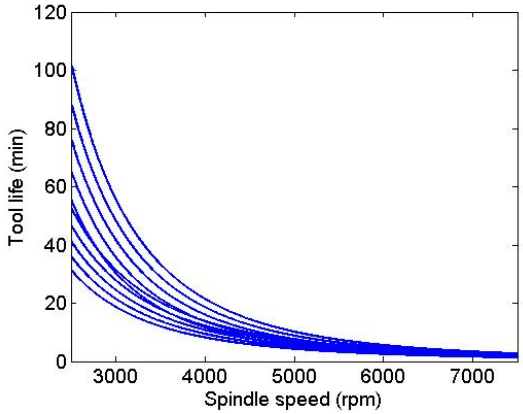

Figure 6.1: Sample tool life curves for the (n, C) pairs listed in Table 6.1.

6.2.2 Likelihood Function

Tool life is generally considered to be stochastic in nature. If a tool life experiment is repeated under the same conditions, it is unlikely that exactly the same tool life would be obtained over multiple trials. The likelihood function is designed to account for this behavior. To illustrate, consider that a tool life of 55.8 min was obtained at 2500 rpm. The user might believe that a tool life between 45 min and 65 min is therefore very likely if the experiment was to be repeated. The user may also believe that it is not very likely that the tool will last less than 35 min or greater than 75 min

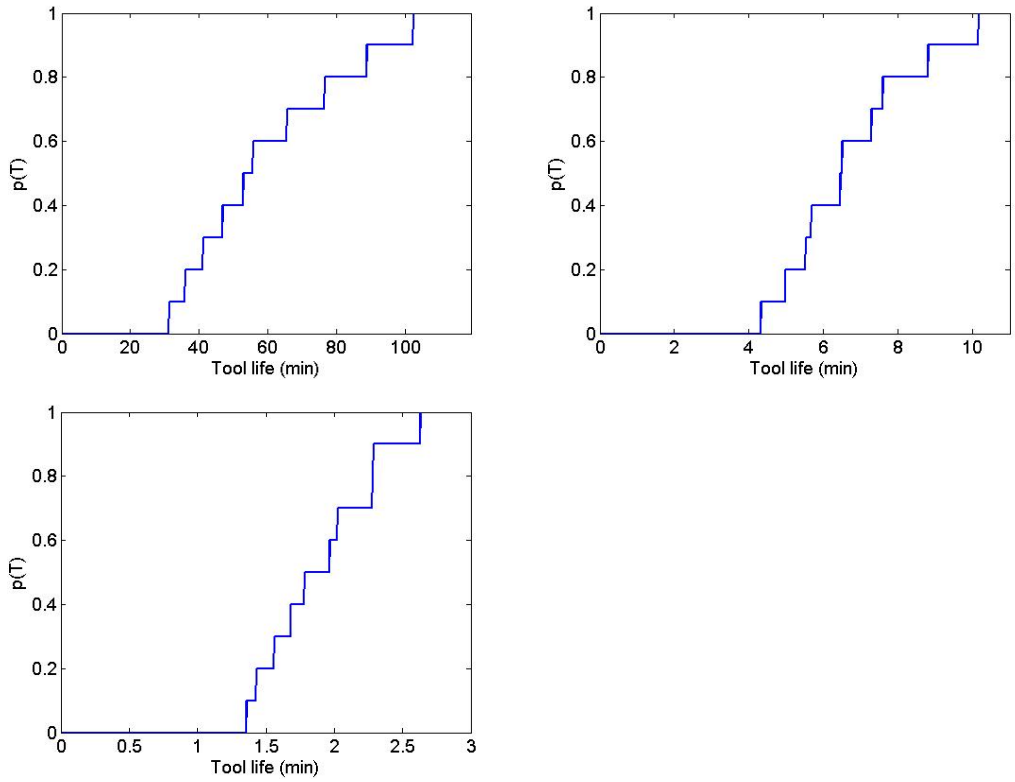

Figure 6.2: Prior cdf of tool life at 2500 rpm (top left), 5000 rpm (top right) and 7500 rpm (bottom left).

based on the initial result. This information is taken into account using the likelihood function provided in Eq. 6.3:

$$l = e^{\frac{-(T-T_m)^2}{k}} \tag{6.3}$$

where l is the likelihood function, T_m is the measured tool life, T is the tool life value for a sample curve at the experimental spindle speed, and k depends on the tool life distribution. The likelihood function is expressed as a non-normalized normal distribution, where $k = 2\sigma^2$ and σ is the standard deviation of tool life. This likelihood function describes how likely is the measurement result at a particular spindle speed given that the sample tool life curve is the correct curve. If the tool life curve value is near the measurement result, then the likelihood value is high. Otherwise, it is low. The likelihood function defined in Eq. 6.3 does not completely reject paths which differ significantly from the experimental result; it simply yields a small value

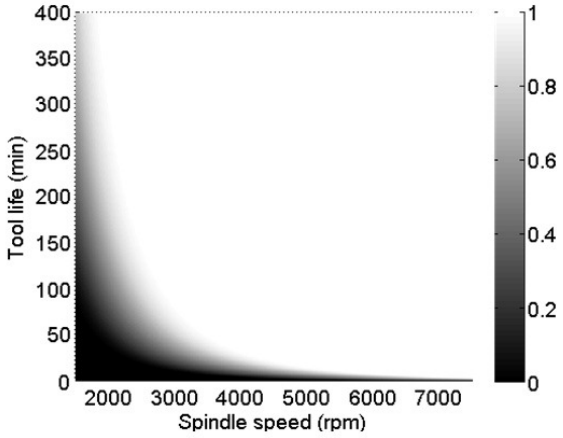

Figure 6.3: Prior cumulative distribution of tool life as a function of spindle speed.

for these paths. To illustrate, again consider the 10 possible (n, C) pairs listed in Table 6.1. Assume an experimental tool life of 55.8 min was obtained at 2500 rpm. At 2500 rpm, each sample tool life curve will have a value of tool life value depending on the (n, C) combination used to generate that sample path. The likelihood function can be interpreted as assigning weights to sample paths from zero to unity, where zero indicates that the selected combination is not likely at all and unity identifies the most likely combination. The likelihood for each sample tool life curve was calculated using Eq. 6.3 with a measured tool life of 55.8 min. The parameter T in the equation is the tool life at the experimental spindle speed (in this example, 2500 rpm) for a particular sample tool life curve. The value of k is selected by the user based on his/her beliefs about the experimental uncertainty. For this study, the standard deviation for an experimental result was assumed to be 20% of the measured value. Table 6.2 lists the likelihood values for each possible (n, C) pair. The likelihood values listed in Table 6.2 imply that 0.30,500 is most likely to be the correct (n, C) combination, whereas (0.30,600) is the least likely. Figure 6.4 shows the likelihood function for T_m = 55.8 min at 2500 rpm for different σ values (and, therefore, k values). As seen in the figure, increased uncertainty (higher σ) widens the likelihood function so that comparatively higher weights are assigned to sample curves far from the experimental

Table 6.2: Likelihood probabilities for sample (n, C) pairs given experimental tool life of 55.8 min at 2500 rpm. The likelihood values are rounded to three significant digits.

Sample	(n,C)	T (2500 rpm) (min)	T (5000 rpm) (min)	T (7500 rpm) (min)	Prior	Likelihood
1	(0.3, 500)	55.8	5.5	1.4	0.1	1.000
2	(0.3, 525)	65.7	6.5	1.7	0.1	0.677
3	(0.3, 550)	76.7	7.6	2.0	0.1	0.174
4	(0.3, 575)	88.9	8.8	2.3	0.1	0.012
5	(0.3, 600)	102.5	10.2	2.6	0.1	0.000
6	(0.35, 500)	31.4	4.3	1.4	0.1	0.009
7	(0.35, 525)	36.1	5.0	1.6	0.1	0.211
8	(0.35, 550)	41.2	5.7	1.8	0.1	0.427
9	(0.35, 575)	46.8	6.5	2.0	0.1	0.724
10	(0.35, 600)	52.9	7.3	2.3	0.1	0.966

result. Subsequently, larger uncertainty yields a more conservative estimate of tool life. Although the value of σ is considered constant in this study, it could also be expressed as a function of spindle speed.

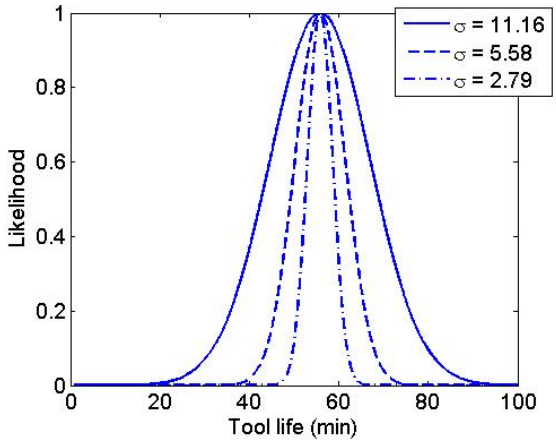

Figure 6.4: Likelihood for various uncertainty levels based on a measured tool life of 55.8 min at 2500 rpm.

6.2.3 Bayesian Updating

As noted, the likelihood function (Eq. 6.3) describes how likely it is that that the sample tool life curve is the correct curve given the measurement result at a particular spindle speed. The prior probability for each path is $1/N$, where N is the number of sample paths. According to Bayes' rule, the posterior distribution is obtained from the product of the prior and the likelihood. The posterior probability for each path is then normalized so that the sum is equal to unity (see Table 6.3). At each spindle speed, the updated probabilities of sample tool life curves provide an updated distribution of tool life. Thus, a tool life experiment at any spindle speed updates the tool life distribution at all spindle speeds. Figure 6.5 displays updated posterior distributions at 2500 rpm, 5000 rpm, and 7500 rpm given an experimental result of $T_m = 55.8$ min at 2500 rpm. Figure 6.5 also shows the prior tool life cdfs for comparison. For the posterior cdf calculation, the updated probabilities, or weights, of the sample paths must be considered.

For multiple experimental results, the posterior after the first update becomes the prior for the second update and so on. For example, consider a second experimental tool life of 5 min at 5000 rpm. The posterior probabilities of the sample paths shown in Table 6.3 are now the prior probabilities for the second update. The updating procedure is repeated to obtain the posterior probabilities of the sample pairs (see Tables 6.4 and 6.5). Figure 6.6 displays updated posterior distribution at 2500 rpm, 5000 rpm, and 7500 rpm after the second update. The mean, standard deviation, and correlation coefficient can be determined from the posterior probabilities using the following relations.

$$\mu_n = \sum nP(n) \tag{6.4}$$

$$\mu_C = \sum CP(C) \tag{6.5}$$

$$\sigma_n = \sum (n - \mu_n)^2 P(n) \tag{6.6}$$

Table 6.3: Posterior probabilities for sample (n, C) pairs after the first update.

Sample	(n, C)	Prior	Likelihood	Posterior (non-normalized)	Posterior (normalized)
1	(0.3, 500)	0.1	1.000	0.1	0.233
2	(0.3, 525)	0.1	0.677	0.068	0.158
3	(0.3, 550)	0.1	0.174	0.017	0.041
4	(0.3, 575)	0.1	0.012	0.001	0.003
5	(0.3, 600)	0.1	0.000	0.000	0.000
6	(0.35, 500)	0.1	0.092	0.009	0.021
7	(0.35, 525)	0.1	0.211	0.021	0.049
8	(0.35, 550)	0.1	0.427	0.043	0.100
9	(0.35, 575)	0.1	0.724	0.072	0.169
10	(0.35, 600)	0.1	0.966	0.097	0.226
			$\sum$	0.428	1.000

$$\sigma_C = \sum (C - \mu_C)^2 P(C) \tag{6.7}$$

$$\rho_{n,C} = \frac{nCP(n,C) - \mu_n \mu_C}{\sigma_n \sigma_C} \tag{6.8}$$

In these equations, the summations are carried out over all N samples; P(n), P(C), and P(n, C) are the posterior probabilities for n, C, and the (n, C) pairs, respectively; μ_n and μ_C are the mean values of n and C, respectively; σ_n and σ_C are the standard deviations of n and C, respectively; and $\rho_{n,C}$ is the correlation coefficient between n and C.

6.2.4 Experimental Setup

The experimental steps followed to collect tool life data are described in this section. Down-milling tool wear tests were completed using a 19.05 mm diameter single-insert Kennametal endmill (KICR073SD30333C). The workpiece material was AISI 1018 steel. The insert was a 9.53 mm square uncoated carbide Kennametal insert (107888126 C9 JC) with zero rake and helix angles and a 15 deg relief angle.

The first test was performed at a spindle speed of 1500 rpm (V = 89.8 m/min).

Table 6.4: Likelihood probabilities for sample (n, C) pairs given experimental tool life of 5.0min at 5000 rpm.

Sample	(n, C)	T (2500 rpm) (min)	T (5000 rpm) (min)	T (7500 rpm) (min)	Prior	Likelihood
1	(0.3, 500)	55.8	5.5	1.4	0.233	0.866
2	(0.3, 525)	65.7	6.5	1.7	0.158	0.318
3	(0.3, 550)	76.7	7.6	2.0	0.041	0.034
4	(0.3, 575)	88.9	8.8	2.3	0.003	0.001
5	(0.3, 600)	102.5	10.2	2.6	0.000	0.000
6	(0.35, 500)	31.4	4.3	1.4	0.021	0.8.02
7	(0.35, 525)	36.1	5.0	1.6	0.049	1.000
8	(0.35, 550)	41.2	5.7	1.8	0.100	0.787
9	(0.35, 575)	46.8	6.5	2.0	0.169	0.343
10	(0.35, 600)	52.9	7.3	2.3	0.221	0.071

Table 6.5: Posterior probabilities for sample (n, C) pairs after the second update.

Sample	(n,C)	Prior	Likelihood	Posterior (non-normalized)	Posterior (normal-ized)
1	(0.3, 500)	0.233	0.866	0.202	0.428
2	(0.3, 525)	0.158	0.318	0.050	0.106
3	(0.3, 550)	0.041	0.034	0.001	0.003
4	(0.3, 575)	0.003	0.001	0.000	0.000
5	(0.3, 600)	0.000	0.000	0.000	0.000
6	(0.35, 500)	0.021	0.802	0.017	0.036
7	(0.35, 525)	0.049	1.000	0.049	0.104
8	(0.35, 550)	0.100	0.787	0.078	0.166
9	(0.35, 575)	0.169	0.343	0.058	0.123
10	(0.35, 600)	0.226	0.071	0.016	0.034
			$\sum$	0.471	1.000

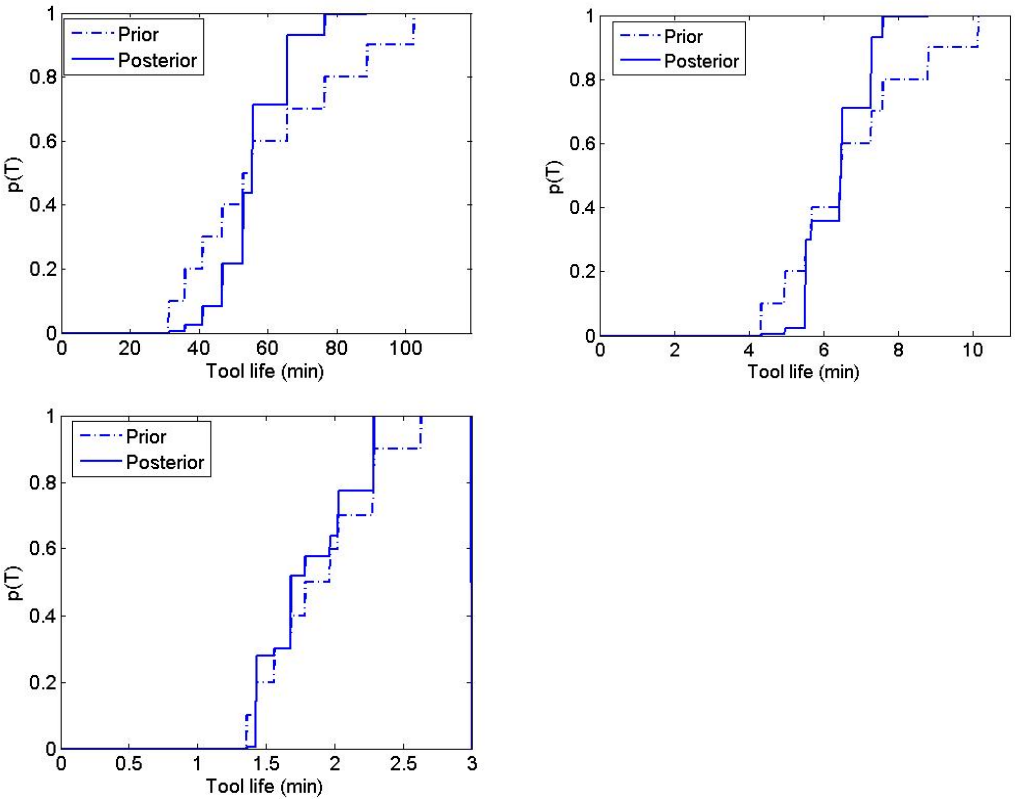

Figure 6.5: Posterior and prior tool life cdfs at 2500 rpm (top left), 5000 rpm (top right), and 7500 rpm (bottom left).

The feed per tooth was 0.06 mm/tooth and the axial and radial depths of cut were 3.0 mm and 4.7 mm (25% radial immersion), respectively. To avoid removing the insert/tool from the spindle, a portable microscope (60x magnification) was used to record digital images of the rake and flank surfaces at regular intervals. Tool life, T, was defined as the time required for the insert to reach a FWW of 0.3 mm (no crater wear was observed in these tests). Figure 6.7 shows the microscope setup for recording the flank surface. The calibrated digital images were then used to identify the FWW. Figure 6.8 shows the variation of FWW with cutting time for tests at 1500 rpm. Microscopic images of the relief face for selected cutting times are displayed in Figure 6.9.

As seen in Figure 6.8, the time to reach a FWW of 0.3 mm was 255.3 min for testing at 1500 rpm. Additional tests were also completed at 3750 rpm and 6250

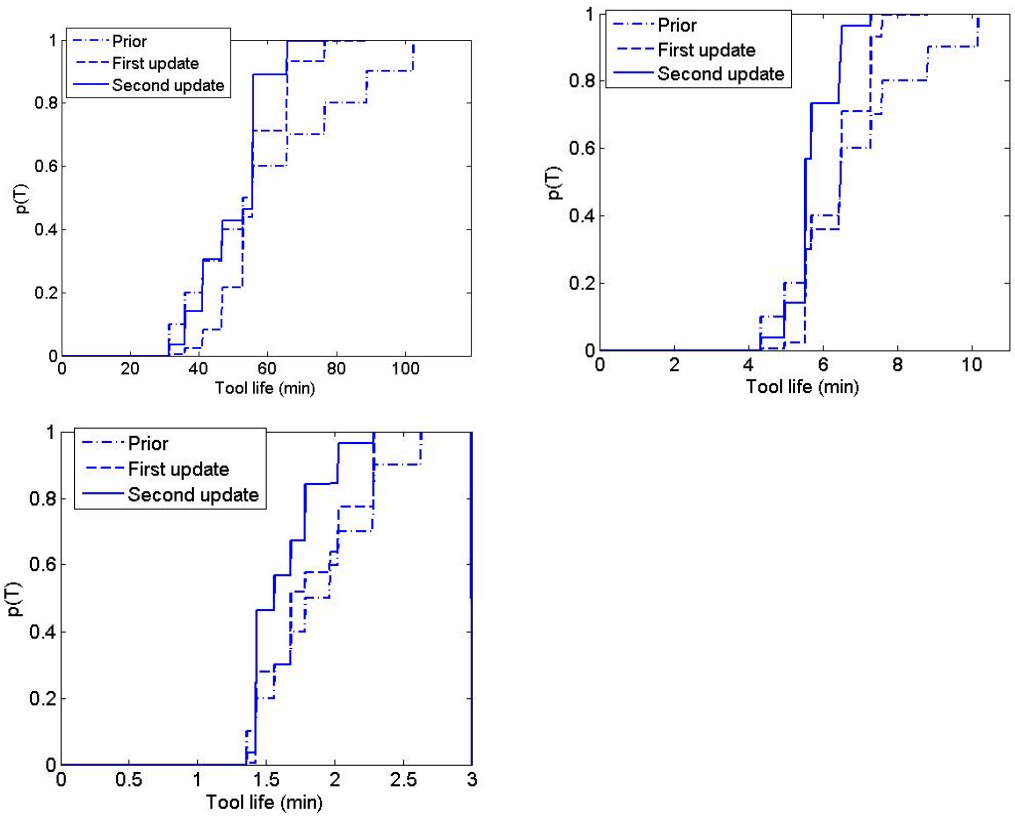

Figure 6.6: Posterior and prior cdf of tool life at 2500 rpm (top left), 5000 rpm (top right), and 7500 rpm (bottom left).

rpm. The variation in FWW with cutting time for spindle speeds is displayed in Figure 6.10. The 'o' symbols denote the intervals at which FWW was recorded. To establish the tool life for each test, linear interpolation was applied between adjacent measurement points if the FWW exceeded 0.3 mm for the final measurement interval. As expected, the tool life reduced with increasing spindle speed. These experimental results were then used to update the prior distributions of tool life over a range of spindle speeds. Table 6.6 summarizes the experimental results used for updating.

6.2.5 Tool Life Predictions

The experimental tool life results were used to update the tool life distribution. The procedure is as follows.

- For each experimental result, a likelihood value was calculated for each sample

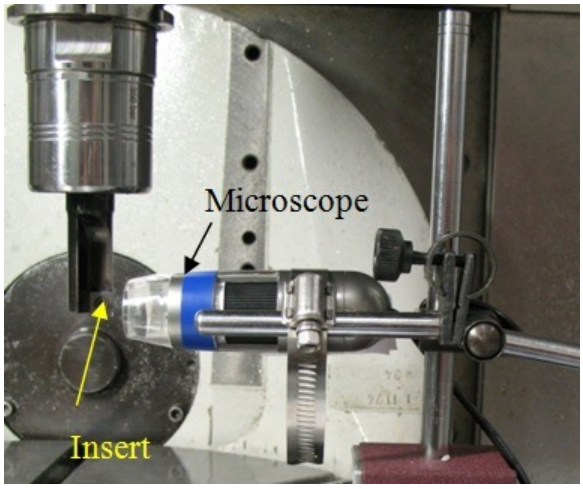

Figure 6.7: Setup for interrupted FWW measurements.

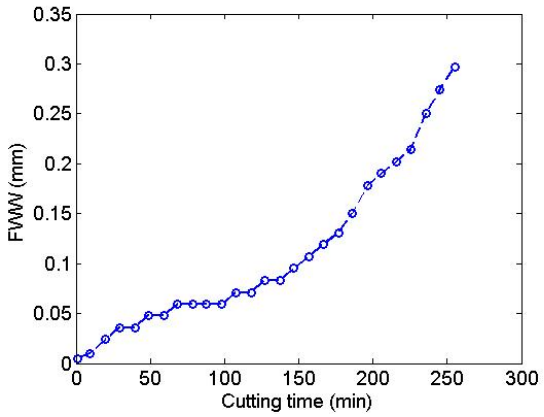

Figure 6.8: Increase in FWW with cutting time at 1500 rpm.

path from Eq. 6.3. The prior probability of each sample path was 1×10^{-5}.

- The posterior probability of each sample path was calculated as the product of the prior probability and the likelihood.
- The posterior probabilities were normalized so that the sum was equal to unity.
- For multiple experimental results, the posterior probabilities after the first update became the prior probabilities for the second and so on.

Figure 6.11 shows the posterior tool life cdf. The posterior probabilities of sample paths were used to determine the mean, standard deviation, and the correlation

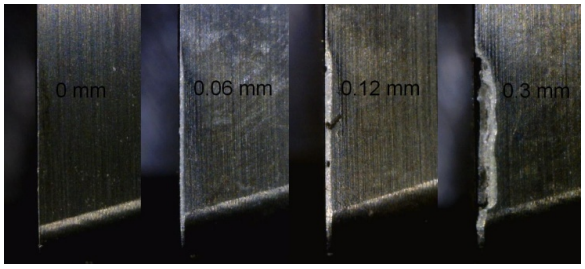

Figure 6.9: Images of FWW at 60X magnification for 1500 rpm tests. The cutting times from left to right are (0, 78.5, 166.4, and 255.3) min.

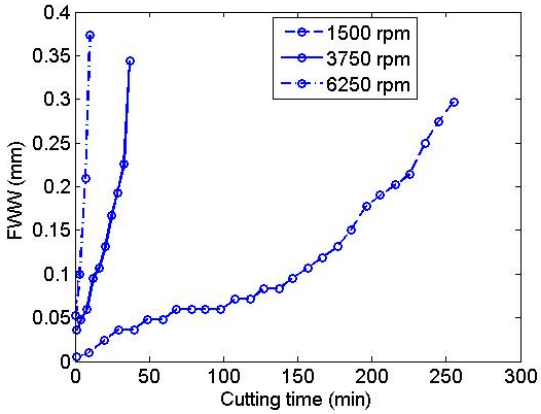

Figure 6.10: Increase in FWW with cutting time at three spindle speeds.

coefficient of the posterior (n, C) distribution using Eqs. 6.4 through 6.8. The values were (0.342, 0.0075) for n and (649.7, 33.74) for C, where the first term in the parenthesis represents the mean and the second term represents the standard deviation. The correlation coefficient between n and C was 0.67. Recall that the prior (n, C) distribution was taken as uniform.

The posterior (updated) tool life distribution was next used to predict tool life at spindle speeds other than the ones at which the tool wear experiments were performed.

Table 6.6: Experimental tool life results used for updating.

Test	Spindle seed (rpm)	Cutting speed (m/min)	Tool life (min)
1	1500	89.8	255.3
2	3750	224.4	35.5
3	6250	374.0	8.5

The posterior distribution was used to predict tool life at 2500, 5000, and 7500 rpm. Three tests were performed at each spindle speed to identify the non-repeatability. The tests were performed using the same parameters (other than spindle speed) as stated previously and the same procedure was followed to measure tool life. As before, tool life was set to be the time to reach a FWW of 0.3 mm. Table 6.7 shows the experimental tool life values observed from the nine tests.

The experimental tool life was compared to the predicted posterior distributions of tool life, T, at the corresponding spindle speeds. Additionally, a least squares curve fit of the Taylor tool life equation was completed using the results provided in Table 6.6. The values of n and C obtained from the least square fit were 0.4553 and 1120 m/min, respectively. Using this deterministic model, the tool life values were also predicted and compared with experiment. Figures 6.12, 6.13, and 6.14 display the posterior distributions of tool life at 2500 rpm, 5000 rpm, and 7500 rpm, respectively. The experimental results are marked using the 'x' symbols and the least squares prediction by the 'o' symbols on the graphs. As seen from the figures, the predicted posterior distributions provide good agreement with the experimental results, while the least squares predictions are less accurate at higher spindle speeds. Although the least squares fit was good ($R^2 = 0.9998$), the fit parameters were not reliable at higher spindle speeds. The 95% confidence bounds for n and C were determined using MATLABs curve fitting toolbox; the values were (0.232,0.6786) for n and (-258,2499) for C. One explanation for the poor performance of the curve fit is that statistical curve fits generally require a large amount of data to achieve confidence in the fit parameters and extrapolation of the prediction outside the test range is often not recommended.

6.3 Bayesian Inference of the Taylor-Type Tool Life Model

In this section, Bayesian inference of the Taylor-type tool life model (Eq. 4.4) using the random surface method is described. In Eq. 4.4, there is uncertainty in the

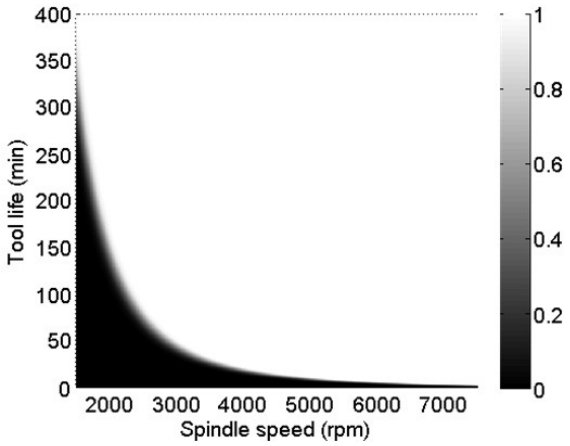

Figure 6.11: Posterior cdf of tool life.

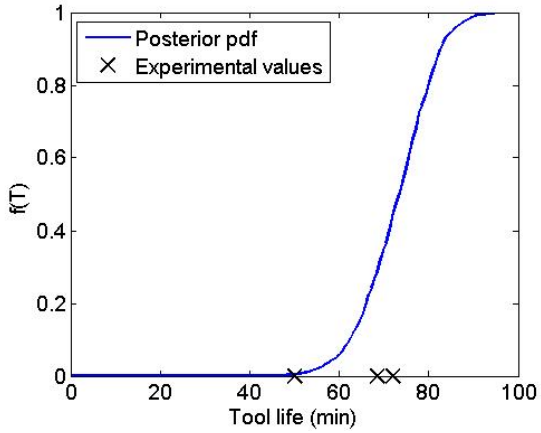

Figure 6.12: Posterior tool life cdf at 2500 rpm.

exponents, p and q, and the constant, C. As a result, there is uncertainty in the tool life. Note that tool life is dependent on both cutting speed and feed rate according to Eq. 4.4. For given values of p and q, and C, tool life may be described using a three-dimensional surface that is a function of cutting speed and feed rate. Therefore, the tool life surface was predicted by generating N tool life (sample) surfaces, each representing the true tool life surface with equal probability. As before, the prior probability that any sample surface is the true tool life surface is $1/N$. For this case,

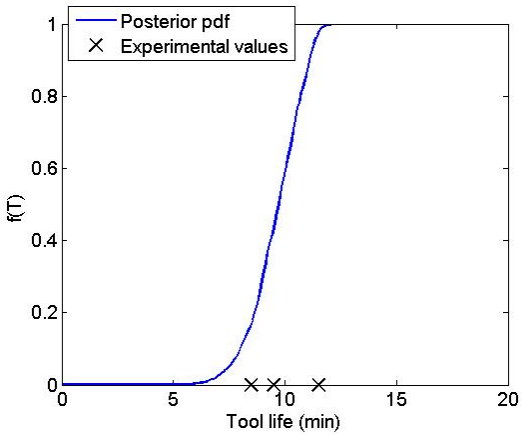

Figure 6.13: Posterior tool life cdf at 5000 rpm.

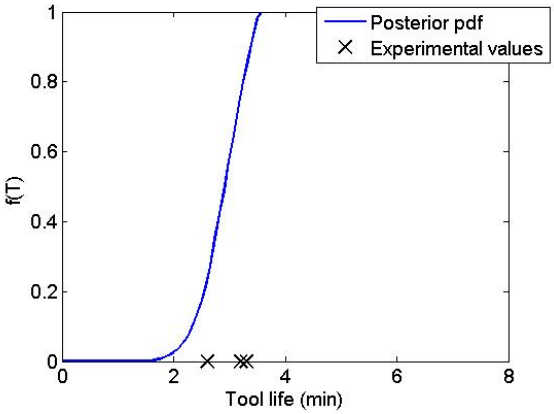

Figure 6.14: Posterior tool life cdf at 7500 rpm.

Bayes' rule can be written as the following product.

$$\mathrm{P}(\textit{surface} = \textit{true tool life surface} | \textit{test result}) \propto$$
$$\mathrm{P}(\textit{test result} | \textit{surface} = \textit{true tool life surface}) \mathrm{P}(\textit{surface} = \textit{true tool life surface})$$

Here, P(*surface = true tool life surface*) is the prior probability that a given path is the true tool life surface. Also, P(*test result* | *surface = true tool life surface*) is referred to as the likelihood, P(*test result*) is a normalization constant, and P(*surface = true tool life surface* | *test result*) is the posterior probability of the sample tool life surface given a test result. The prior sample paths were generated using random

Table 6.7: Experimental values of tool life for comparison to predictions.

Test	Spindle seed (rpm)	Cutting speed (m/min)	Tool life (min)
1	2500	149.6	50.1
2	2500	149.6	68.5
3	2500	149.6	72.0
4	5000	299.2	11.5
5	5000	299.2	9.5
6	5000	299.2	8.5
7	7500	448.8	2.6
8	7500	448.8	3.3
9	7500	448.8	3.2

samples from (p, q, C) joint pdf. The prior (initial) p, q, and C distributions were selected based on a literature review.

6.3.1 Establishing the Prior

As noted, the first step in applying Bayesian inference is to determine the prior distribution. The cutting tool used for wear testing was a coated carbide insert and the workpiece material was a forged chrome alloy steel. The turning experiments were performed on an Okuma LC-40 CNC lathe. In this case, the prior was a joint probability distribution for the Taylor-type tool life constants, p, q, and C. The initial beliefs were:

- in general, the value of the exponent p is greater than the exponent q due to a stronger influence of cutting speed on tool wear, but this is not a strict requirement.
- the value of p is between 2 and 6 and q is between 1.5 and 3 [10].
- the value of C is sensitive to the values of p and q due to the nature of the tool life equation and is in the range of 1×10^6 m/min to 1×10^8 m/min.

In this case, information was available to supply only a general range of p, q, and C. Therefore, the prior was assumed to be joint uniform distribution, i.e., it was

equally likely to obtain any value within the specified range. The constants were assumed to be independent of each other for the prior. In cases where experimental data using the same tool-material combination is available, a more informative prior (such as a normal distribution) can be selected. For this study, the marginal prior pdfs of the constants were specified as: p = U(2, 6), q = U(1, 5), and C = U(1×10^6, 1×10^8).

Random samples were drawn from the prior joint pdf of p, q, and C and the Taylor-type tool life surface was calculated for each (p, q, C) triplet. In total, 1×10^5 tool life surfaces were generated. The range of cutting speed was taken from 150 m/min to 250 m/min and feed rate from 0.5 mm/rev to 0.6 mm/rev. The prior probability that any sample surface is the true tool life surface for this case is 1×10^{-5}. The updating procedure is the same as for the random walk approach. The only difference is that the random samples form three-dimensional surfaces, rather than two-dimensional paths. To demonstrate the procedure, again consider 10 possible combinations of (p, q, C); see Table 6.8. The prior assumes that any combination is equally likely to be the true combination, so each (p, q, C) triplet was assigned a probability of 0.1. The Taylor-type tool life values were calculated for all cutting speeds and feed rates in the domain for the 10 (p, q, C) triplets. Figure 6.15 shows the sample tool life surfaces. Table 6.8 also provides the tool life values for all (p, q, C) combinations at cutting conditions of 150 m/min, 0.5 mm/rev, 150 m/min, 0.6 mm/rev, and 200 m/min, 0.5 mm/rev. Figure 6.16 shows the discrete cdf of tool life at the same cutting conditions. The cdf gives the probability of tool failure as a function of tool life.

The procedure was completed for 1×10^5 sample surfaces generated by drawing random samples from the prior (p, q, C) distribution. Since tool life depends on cutting speed as well as feed rate, the prior cdf as a function of cutting speed is conditioned on the feed rate value. Figure 6.17 shows the prior cdf of tool life as a function of cutting speed for a selected feed rate value. There is large uncertainty in

Table 6.8: Prior probabilities for sample (p, q, C) triplets.

Sample	(p, q, C)	T (150 m/min, 0.5 mm/rev) (min)	T (200 m/min, 0.5 mm/rev) (min)	T (150 m/min, 0.6 mm/rev) (min)	Prior
1	(2.50, 2.50, 1×10^7)	205.3	100.0	130.1	0.1
2	(2.75, 2.50, 1×10^7)	58.7	26.6	37.2	0.1
3	(2.50, 2.25, 1×10^7)	172.6	84.1	114.5	0.1
4	(2.75, 2.25, 1×10^6)	49.3	22.4	32.7	0.1
5	(2.50, 2.50, 5×10^6)	102.6	50.0	65.1	0.1
6	(2.75, 2.50, 5×10^6)	29.3	13.3	18.6	0.1
7	(2.50, 2.25, 5×10^6)	86.3	42.0	57.3	0.1
8	(2.75, 2.25, 5×10^6)	24.7	11.2	16.4	0.1
9	(2.50, 2.25, 7.5×10^6)	129.5	63.1	85.9	0.1
10	(2.75, 2.25, 7.5×10^6)	37.0	16.8	24.5	0.1

the tool life due to the wide (uniform) prior distribution assumed for p, q, and C. The color bar in Figure 6.17 gives the probability of tool failure at a selected tool life for any spindle speed in the domain. From the prior distribution of p, q, and C, approximately 50% of the tool life values are less than 1 min and 15% are more than 400 min at 150 m/min, 0.5 mm/rev; therefore, the probability of tool failure in Figure 6.17 is scaled from 0.5 to 0.85 for plotting purposes.

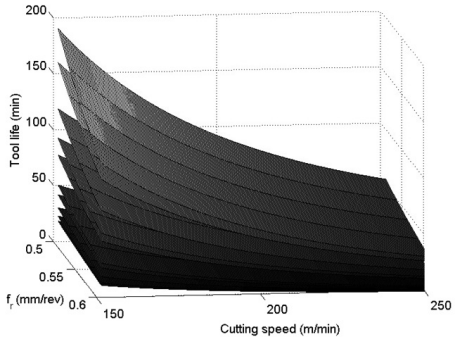

Figure 6.15: Sample tool life surfaces for (p, q, C) triplets provided in Table 6.8.

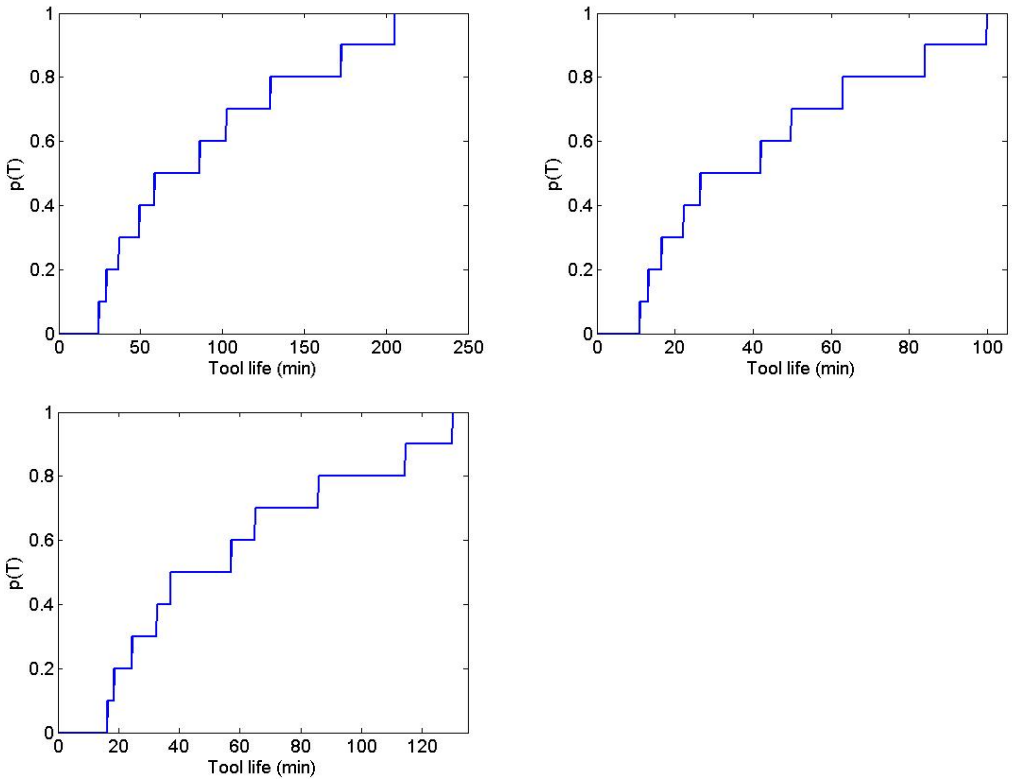

Figure 6.16: Prior cdf of tool life at (150 m/min, 0.5 mm/rev) (top left), (200 m/min, 0.5 mm/rev) (top right), and (150 m/min, 0.6 mm/rev) (bottom left).

6.3.2 Bayesian Updating

The likelihood function describes how likely it is that that the sample tool life surface is the correct surface given a measurement result at a particular cutting speed and feed. As noted, the likelihood function can be interpreted as assigning weights to sample surfaces from zero to unity, where zero indicates that the selected combination is not likely at all and unity identifies the most likely combination. The likelihood function defined in Eq. 6.3 was applied. To illustrate, again consider the 10 possible (p, q, C) triples listed in Table 6.8. Assume that an experimental tool life of 102.6 min was obtained at 150 m/min, 0.5 mm/rev and a tool life of 42.0 min was obtained at 200 m/min, 0.5 mm/rev. A likelihood value for each sample tool life surface was calculated using Eq. 6.3. The posterior probability calculations are shown in Tables 6.9 and 6.10. Note that these posterior probabilities are normalized and have

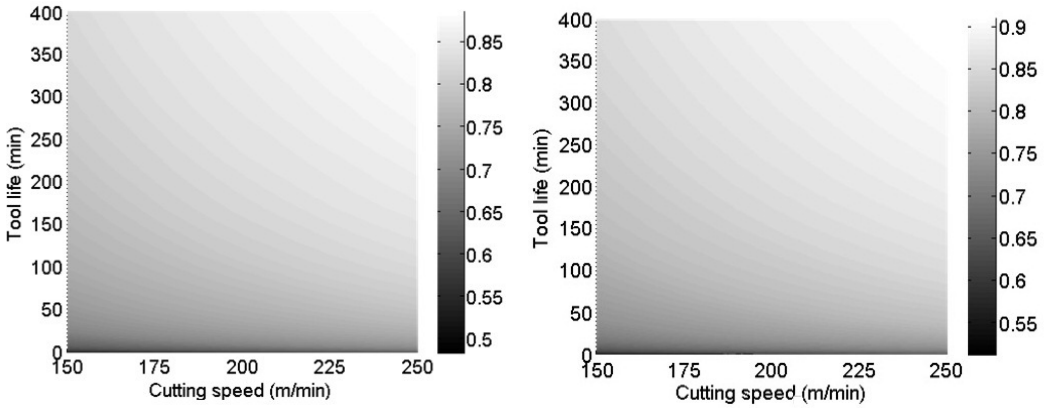

Figure 6.17: Prior cdf of tool life at 0.5 mm/rev (left) and 0.6 mm/rev (right). Note that the reduced tool life for the 0.6 mm/rev feed results in approximately 10% of the values being more than 400 min as compared to 15% at 0.5 mm/rev. The color bar scaling therefore differs.

been rounded to three significant digits. Figure 6.18 shows the posterior and prior cdf at 150 m/min, 0.5 mm/rev, 200 m/min, 0.5 mm/rev, and 150 m/min, 0.6 mm/rev.

6.3.3 Experimental Setup and Results

This section describes the experimental steps following to collect turning tool life data. The cutting tool used for wear testing was a coated carbide insert (Kennametal KC9110) and the workpiece material was forged AISI 4137 chrome alloy steel. The initial outer diameter of the steel workpiece was 174.6 mm. The spindle speed was varied to maintain constant cutting speed with reducing workpiece diameter as additional cuts were completed. The depth of cut was 4.1 mm and the length of cut for a single pass was 139.7 mm with a chamfer of 63.4 deg at the end of each cut. The flank and rake surfaces were recorded using a portable digital microscope (60X magnification) without removing the insert from the tool holder during the wear testing. The wear status of the tool was recorded after each pass and the calibrated digital images were used to identify the flank wear width (FWW). Tool life was defined as the time required for the FWW to reach 0.4 mm. The first test was completed using a cutting speed of 153.6 m/min and a feed per revolution of 0.51 mm/rev. Figure 6.19 shows

Table 6.9: Likelihood and posterior probabilities for sample (p, q, C) triplets given an experimental tool life of 102.6 min at (150 m/min, 0.5 mm/rev)

.

Sample	(p, q, C)	Prior	Likelihood	Posterior
1	(2.50, 2.50, 1×10^7)	0.1	0.000	0.000
2	(2.75, 2.50, 1×10^7)	0.1	0.101	0.044
3	(2.50, 2.25, 1×10^7)	0.1	0.003	0.001
4	(2.75, 2.25, 1×10^7)	0.1	0.034	0.015
5	(2.50, 2.50, 5×10^6)	0.1	1.000	0.435
6	(2.75, 2.50, 5×10^6)	0.1	0.002	0.001
7	(2.50, 2.25, 5×10^6)	0.1	0.730	0.317
8	(2.75, 2.25, 5×10^6)	0.1	0.001	0.000
9	(2.50, 2.25, 7.5×10^6)	0.1	0.424	0.184
10	(2.75, 2.25, 7.5×10^6)	0.1	0.006	0.003
			$\sum$	1.000

Table 6.10: Likelihood and posterior probabilities for sample (p, q, C) triplets given an experimental tool life of 42.0 min at (200 m/min, 0.5 mm/rev)

Sample	(p, q, C)	Prior	Likelihood	Posterior
1	(2.50, 2.50,1×10^7)	0.000	0.000	0.000
2	(2.75, 2.50, 1×10^7)	0.044	0.186	0.013
3	(2.50, 2.25, 1×10^7)	0.001	0.000	0.000
4	(2.75, 2.25, 1×10^7)	0.015	0.065	0.002
5	(2.50, 2.50, 5×10^6)	0.435	0.635	0.452
6	(2.75, 2.50, 5×10^6)	0.001	0.003	0.000
7	(2.50, 2.25, 5×10^6)	0.317	1.000	0.52
8	(2.75, 2.25, 5×10^6)	0.1	0.000	0.000
9	(2.50, 2.25, 7.5×10^6)	0.184	0.043	0.013
10	(2.75, 2.25, 7.5×10^6)	0.003	0.011	0.000
			$\sum$	1.000

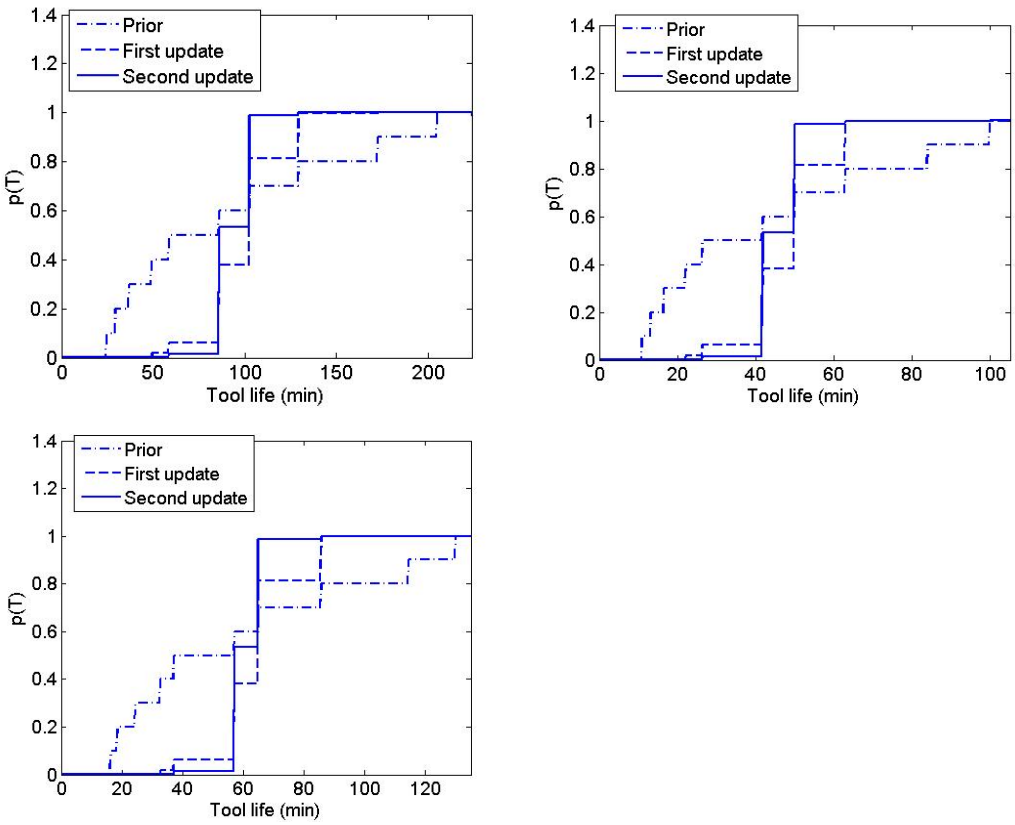

Figure 6.18: Posterior and prior cdf of tool life at (150 m/min, 0.5 mm/rev) (top left), (200 m/min, 0.5 mm/rev) (top right), and (150 m/min, 0.6 mm/rev) (bottom left).

the variation of FWW with cutting time. The time to reach a FWW of 0.4 mm was 22.5 min. Figure 6.20 shows images of the relief face at selected cutting times.

Two additional tests were performed at (V = 192.0 m/min, f_r = 0.61 mm/rev) and (V = 230.4 m/min, f_r = 0.51 mm/rev). Figure 6.21 shows the growth in FWW for all three test conditions. The 'o' symbols denote the intervals at which the FWW was recorded. The tool life was determined by linear interpolation between adjacent intervals if it exceeded 0.4 mm at the final measurement interval. The results of the three tests are summarized in Table 6.11. As expected, tool life reduced with increased cutting speed and feed rate.

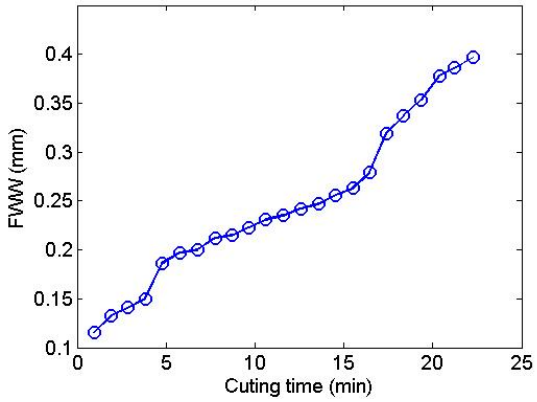

Figure 6.19: Increase in FWW with cutting time at $V = 153.6$ m/min and $f_r = 0.51$ mm/rev.

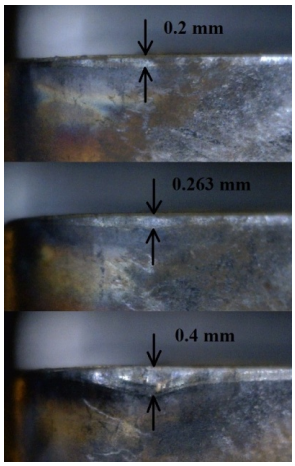

Figure 6.20: Images of FWW at 60X magnification. The cutting times from top to bottom are (6.8, 15.5, and 22.4) min.

6.3.4 Tool Life Predictions

The experimental tool life results were used to update the prior tool life distribution using the random surface method. As noted, $1{\times}10^5$ sample surfaces were generated by sampling from the prior (p, q, C) distribution. The likelihood for each test result was calculated using Eq. 6.3. The prior probabilities of the sample surfaces were updated using the experimental result following the procedure described. The posterior probability of each sample surface was calculated as the product of the prior probability and the likelihood. The posterior probabilities were normalized so that

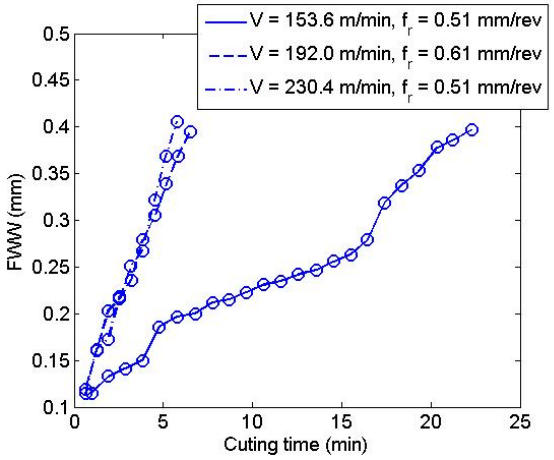

Figure 6.21: Variation of FWW with cutting time at various test conditions.

Table 6.11: Experimental tool life results used for updating.

Test	Cutting speed (m/min)	Feed (mm/rev)	Tool life (min)
1	153.6	0.51	22.5
2	192.0	0.61	6.5
3	230.4	0.51	5.6

the sum was equal to unity. Figure 6.22 shows the posterior cumulative distribution of tool life as a function of cutting speed conditioned on the feed rate value. The mean and standard deviation, for the posterior (p, q, C) distributions were (3.25, 0.19) for p, (2.81, 0.99) for q, and (5.2×10^7, 2.85×10^7) m/min for C, where the first term is the mean and the second is the standard deviation. The correlation coefficients were 0.64 between p and q, 0.71 between p and C, and 0.032 between q and C.

The posterior tool life distributions can be used to predict tool life at cutting conditions other than the ones at which the tool wear experiments were performed. The posterior distribution was used to predict tool life for two new test conditions: (V =192.0 /min, f_r = 0.51 mm/rev) and (V = 230.4 m/min, f_r = 0.61 mm/rev). Two tests were performed for each parameter combination. Other conditions were maintained constant and the same procedure was followed to measure tool life. As

before, tool life was selected to be the time for the tool to reach a FWW of 0.4 mm. Table 6.12 shows the experimental tool life values observed from the four additional tests.

The deterministic Taylor-type tool life constants were calculated using a least squares best fit to the experimental tool life data listed in Table 6.11. The p, q, and C values were 3.39, 2.63, and 9.83×10^7 m/min, respectively. Figure 6.23 shows the experimental values at $V = 192.0$ m/min and $f_r = 0.51$ mm/rev (denoted by 'x'), the posterior distribution after updating, and the deterministic tool life predictions (denoted by 'o'). Figure 6.24 shows the results for $V = 230.4$ m/min and $f_r = 0.61$ mm/rev. As seen in Figure 6.23, the observed tool life values agree with both the predicted posterior distribution and the deterministic predictions at $V = 192.02$ m/min, $f_r = 0.51$ mm/rev. In Figure 6.24, both predictions slightly overestimate the tool life. A significant difference between the two techniques, however, is that Bayesian inference assigns a probability distribution to tool life, while deterministic methods (such as curve fitting) predict a single value.

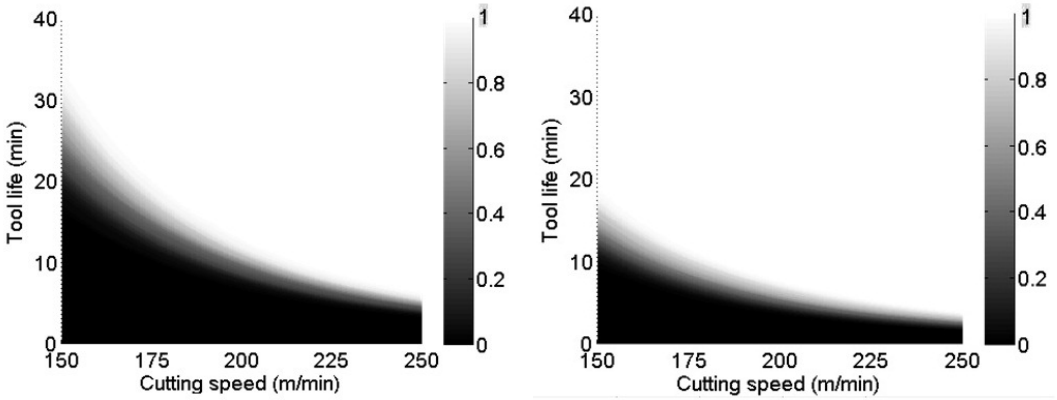

Figure 6.22: Posterior cdf of tool life at 0.5 mm/rev (left) and 0.6 mm/rev (right).

6.4 Discussion

In Bayesian inference, the posterior probability is the product of the prior and the likelihood distributions. Clearly, the posterior probabilities of the random sample

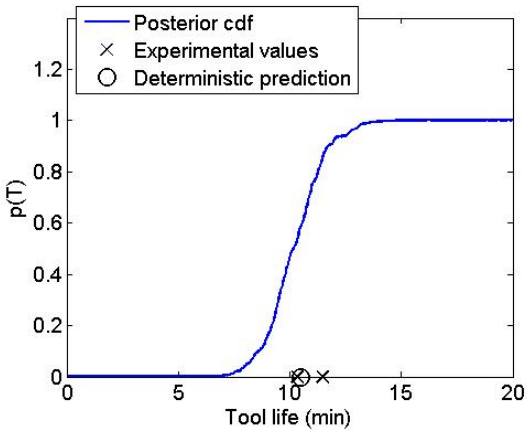

Figure 6.23: Posterior tool life cdf at $V = 192.02$ m/min, $f_r = 0.51$ mm/rev.

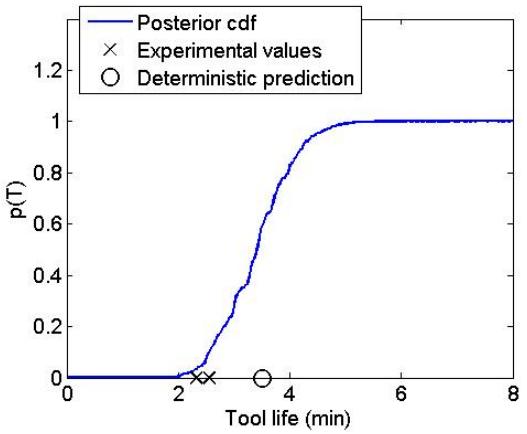

Figure 6.24: Posterior tool life cdf at $V = 230.42$ m/min, $f_r = 0.61$ mm/rev.

paths/surfaces depend on the selection of the prior and the likelihood distributions. In this section, the influence of the prior distribution and likelihood uncertainty on the posterior is evaluated. First, the influence of the likelihood uncertainty on the posterior tool life cdf is examined. In the initial analysis, a likelihood uncertainty of 20% of the experimental tool life was assumed. Here, Bayesian updating was repeated for both the milling and turning tool life models using likelihood uncertainties of 5% and 10%. Figure 6.25 displays the milling posterior tool life predictions at 2500 rpm for different likelihood uncertainties. The experimental values are denoted as 'x' and the deterministic prediction as 'o'. Table 6.13 lists the mean, standard deviation, and the correlation coefficient for the corresponding posterior n and C distributions.

Table 6.12: Experimental values of tool life for additional turning tests.

Test	Cutting speed (m/min)	Feed (mm/rev)	Tool life (min)
1	192.0	0.51	11.5
2	192.0	0.51	10.3
3	230.4	0.61	2.2
3	230.4	0.61	2.6

As seen from Figure 6.25 and the standard deviation values listed in Table 6.13, the likelihood uncertainty affects the spread of the posterior tool life distribution. A smaller likelihood uncertainty narrows the distribution. Also, as the likelihood uncertainty tends to zero, the posterior tool life cdf approaches the least squares prediction. Similar results are obtained for the turning tool life model as shown in Figure 6.26.

The influence of the prior distribution on the posterior distribution was also examined. As stated, a uniform prior was selected for (n, C) in the milling model to generate the random sample paths. To evaluate the influence of the prior distribution, a normal distribution was selected for the prior (n, C) distribution. The distribution was selected to be:

n = N(0.3, 0.03) and C = N(250, 50),

where N denotes a normal distribution and the values in the parentheses identify the mean and standard deviation, respectively. The n and C random samples were assumed to be independent. The mean values of the normal (n, C) prior distribution were deliberately selected to be lower than the posterior mean values determined in Section 6.2. Random samples were drawn from the distribution and the sample tool life curves were calculated for each. Figure 6.27 shows the new (normal) prior distribution. Bayesian updating was completed using the experimental results listed in Table 6.6. Figure 6.28 shows the posterior tool life cdf for the normal prior.

The posterior cdf for the uniform prior is also included for comparison. Table 6.14 compares the posterior means, standard deviations, and correlation coefficients for the two priors. As seen in Figure 6.28, the posterior tool life prediction is more conservative for the normal (n, C) prior, which may be a preferred result in machining operations where a tool failure can lead to significant expense and lost time. A normal prior represents a more informative case where knowledge of the distribution in (n, C) values is available. A more informative prior reflects the most likely values. Because the prior represents the initial degree of belief about the constants, if the initial belief is far from the true value, then the final results are affected. In general, the prior should be chosen to be as informative as possible considering all the available information. If enough data or prior knowledge is not available, a uniform prior may be selected.

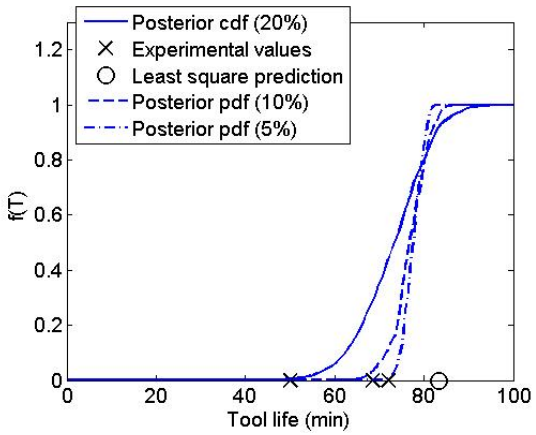

Figure 6.25: Posterior cdf at 2500 rpm for different likelihood uncertainties assumed.

6.5 Experimental Speed Selection using Value of Information

The combination of Bayesian inference and decision analysis enables a dollar value to be placed on the information gained from an experiment prior to performing it. The value of information, VOI, may be defined as the difference between the expected profit before testing and the expected profit after testing. For a fixed sales price, VOI is the expected cost prior to testing minus the expected cost after testing. In

Table 6.13: Posterior (n, C) distribution for different likelihood uncertainties in milling.

Parameters	Likelihood uncertainty		
	20%	10%	5%
(μ_n,σ_n)	(0.34, 0.0075)	(0.35, 0.0023)	(0.35, 0.0006)
(μ_C,σ_C)	(649.7, 33.7)	(676.3, 14.1)	(685.2, 7.1)
$\rho_{n,C}$	0.67	0.45	0.28

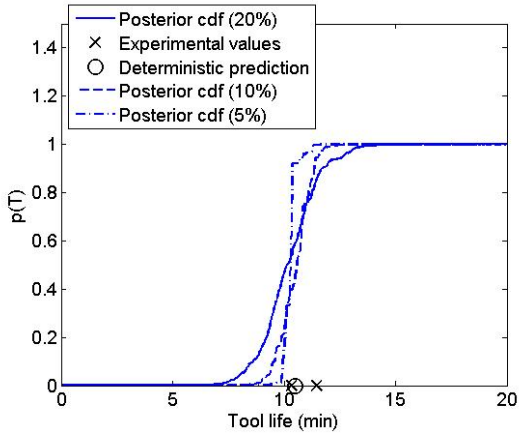

Figure 6.26: Posterior tool life cdf at V = 192.02 m/min, f_r = 0.51 mm/rev for different likelihood uncertainties.

simple terms, VOI identifies the monetary gain from performing an experiment. Note that the value of information is the expected value obtained after an experiment; it is actually calculated before performing the test. The primary motivation for calculating VOI is to design the experimental study. The experimental test point is chosen which adds the most (expected) value to the profit. In addition, if the expected cost of

Table 6.14: Posterior (n, C) distribution for normal and uniform prior.

Parameters	Likelihood uncertainty	
	Uniform	Normal
(μ_n, σ_n)	(0.342, 0.001)	(0.2661,0.02)
(μ_C,σ_C)	(649.7,33.7)	(378.1,20.6)
$\rho_{n,C}$	0.67	0.65

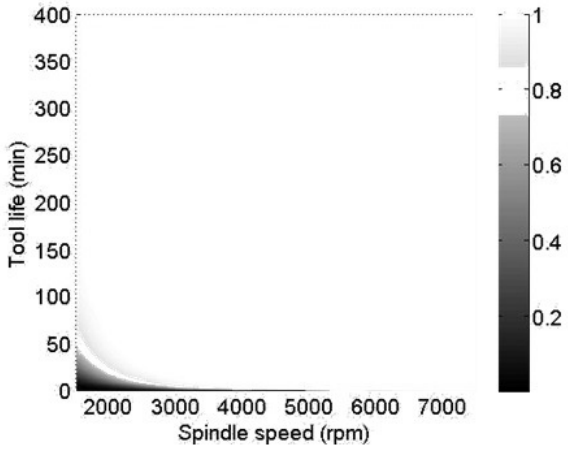

Figure 6.27: Prior cumulative distribution of tool life for the normal (n, C) prior.

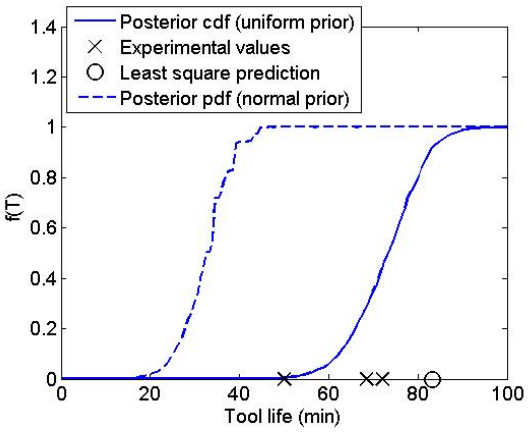

Figure 6.28: Posterior tool life cdf at 2500 rpm for different priors.

performing an experiment is greater than VOI, it is probably not a good idea to experiment at all.

6.5.1 Determining the Cost

Before calculating the value of information, it is necessary to determine the cost of performing the test given the selected operating conditions. In this study, it was assumed that a pocket was to be machined. The volume of material to be removed, Vol, was assumed to be $1{\times}10^5$ mm^3. The machining cost, C_m, is shown in Eq. 6.9.

$$C = t_m r_m + \frac{(t_m r_m + C_{te}) t_c}{T} \tag{6.9}$$

The machining time is calculated from the material removal rate, MRR, and the volume to be removed. See Eqs. 6.10 and 6.11:

$$\text{MRR} = N_t \Omega f_t a b \tag{6.10}$$

$$t_m = \frac{V}{MRR} \tag{6.11}$$

Because tool life has a probability of failure associated with it (see Figure 6.11), the machining cost is modified to be an expected cost. This requires that a user-defined cost of tool failure, L, be included in the cost expression, where tool failure denotes that the worn tool has exceeded the permissible wear limit (for example, maximum FWW) and a tool failure results in additional cost. This may be due to loss of machining time, reduced productivity, cost of reworking the part, or discarding the part altogether. The term L takes into account all the costs associated with a tool failure. The value of L need not be determined accurately; L can be interpreted as the value that must be paid to the user that will make him/her indifferent to a tool failure. The expected machining cost at any spindle speed, E(C_m), is given by Eq. 6.12, where p is the probability of tool failure (obtained from the posterior cdf as shown in Figure 6.11, for example). The best spindle speed for testing corresponds to the lowest expected cost from Eq. 6.12. To demonstrate the concept of expected cost, let the cost of machining at some spindle speed be \$10. Let the probability of tool failure be 0.1 and let L also be equal to \$10. For a production run of 100 parts, there will be (on average) ten tool failures because $p = 0.1$. This will incur an additional cost of \$10 for each of the 10 tool failures. Thus, the expected total cost of machining 100 parts is \$100×10 + \$10×10 = \$1100. The expected machining cost of a single part is then \$11. The values of the variables used to calculate machining cost for this study are listed in Table 6.15.

Table 6.15: Cost variables and values.

Variable	Value	Unit
d	19.05	mm
f_t	0.06	mm/tooth
a	4.76	mm
b	3	mm
N_t	1	-
r_m	10	\$/min
V	1×10^5	mm^3
C_{te}	10	\$
t_{ch}	2	min
L	1000	\$

$$\begin{aligned} C &= (1-p)(t_m r_m + \frac{(t_m r_m + C_{te})t_c}{T}) + p(t_m r_m + \frac{(t_m r_m + C_{te})t_c}{T} + L) \\ &= (t_m r_m + \frac{(t_m r_m + C_{te})t_c}{T}) + pL \end{aligned}$$

To illustrate the approach, consider the prior cdf shown in Figure 6.3. Assume that an experimental tool life of 7 minutes at 5000 rpm for this example. The prior cdf was updated using the procedure described in Section 6.2. Each tool life at 5000 rpm has a probability of failure associated with it. The tool life values, T, and the corresponding probability of tool failure, p, were used to calculate the expected cost for each 5000 rpm tool life by Eq. 6.12. Figure 6.29 shows the prior cost of machining at 5000 rpm as a function of tool life. At higher tool life values ($T > 9$ min), the term pL dominates the cost equation. At small values of tool life ($T < 3$ min), the value of p is close to zero. Also, at small tool life values, where a higher number of tool changes is required, the second part of Eq. 6.12 dominates the cost equation. From the prior, the minimum machining cost for a spindle speed of 5000 rpm is \$526.70 at 2.51 minutes with a probability of failure equal to 0.015. Figure 6.30 shows the posterior cost at 5000 rpm. The minimum machining cost is \$431.10 at 4.13 minutes with

Table 6.16: Optimum machining cost and tool life for prior and posterior distributions.

	Machining cost ($)	Tool life (min)	Spindle speed (min)	Probability of tool failure
Prior	482.6	5.75	3740	0.008
Posterior	422.6	6.31	4292	0.021

a probability of failure equal to 0.028. This procedure was repeated at all spindle speeds. Figure 6.31 shows the minimum cost as a function of spindle speed based on the prior and the posterior distributions of tool life. Table 6.16 summarizes the smallest value from the minimum cost curve and optimum tool life based on the prior and posterior. Risk neutrality of the user was assumed in this study. However, for a risk averse user, an acceptable threshold value of p can be set. This means that a risk averse user can say that he/she is not willing to operate at any spindle speed where a threshold value of p is exceeded. In that case, the expected cost at a spindle speed would be calculated using tool life values with p values less than the user defined threshold. Risk aversion leads to a conservative estimate of optimum tool life and the corresponding spindle speed.

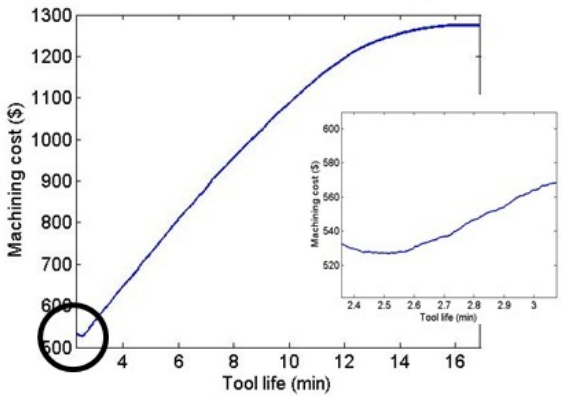

Figure 6.29: Machining cost based on the prior at 5000 rpm as a function of tool life.

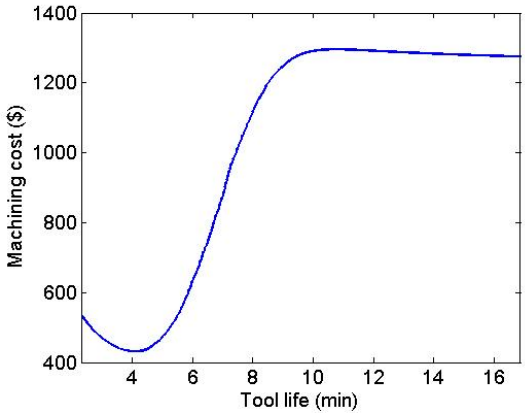

Figure 6.30: Machining cost based on the posterior at 5000 rpm as a function of tool life.

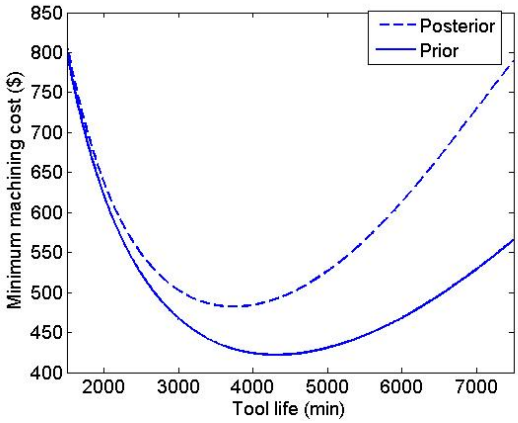

Figure 6.31: Minimum machining cost based on prior and posterior tool life distributions.

6.5.2 Selection the Best Spindle Speed

To determine an optimum test spindle speed, the test spindle speed range was divided into discrete intervals (50 rpm increments were used here). As a heuristic, it was assumed that a test at a selected spindle speed gives the expected tool life at that speed. (Recall that the value of information is determined before actually performing the test.) The uncertainty in the experimental tool life was assumed to be 20%. It was also assumed that 1000 pockets need to be machined. The value of information is then given by Eq. 2.6.

Note that there is some cost associated with performing a tool life experiment. If

the cost of performing the experiment exceeds the VOI, it suggests that no additional testing is necessary. The procedure to calculate VOI follows. First, the expected cost before testing is calculated from the prior distribution (see Figure 6.3). Second, at each test spindle speed, the prior is updated using the expected tool life at that speed from the prior distribution. Third, the expected cost after testing is calculated using the updated posterior cdf. As shown in Eq. 6.12, the expected cost of performing a test, E(C_t), is calculated as the sum of the expected cost for the experiment (the product of the expected tool life and rate of machining), the tool cost, and the expected material cost. The material cost is the product of the expected tool life, material removal rate, and the cost per unit volume of the material. The cost per unit volume of AISI 1018 steel was taken as 6×10^{-5} \$/mm^3. Note that the material removal rate is dependent on spindle speed (the number of teeth, feed per tooth, and axial/radial depths were assumed to be fixed in this study).

$$E(C_t) = E(T)r_m + C_{te} + 6 \times 10^{-5} E(T)MRR \tag{6.12}$$

To illustrate, consider three test speeds, 1500 rpm, 5000 rpm and 7500 rpm. If a test was to be performed at these speeds, it was assumed that the measured tool life would be equal to the expected tool life at those speeds. The expected tool life (determined from the prior) at 1500 rpm, 5000 rpm, and 7500 rpm is 302 minutes, 7 minutes, and 2 minutes, respectively. Table 6.16 shows the prior and posterior minimum cost given a measured tool life of 7 minutes at 5000 rpm. The same procedure is followed to calculate the posterior cost given an experimental result of 302 minutes at 1500 rpm and 2 minutes at 7500 rpm. The posterior minimum cost after testing was then used to calculate VOI. Note that it costs more to perform a test at 1500 rpm than at 7500 rpm because the tool generally lasts longer at lower cutting speeds. Table 6.17 summarizes the three results. It is observed that it is most profitable to complete a

Table 6.17: Value of information for different spindle speeds

Test speed (rpm)	Prior cost ($)	E(T)(min)	Posterior cost ($)	Test cost($)	VOI ($)
1500	482.6	302.0	413.3	3056.8	82410
5000	482.6	7.0	422.2	83.4	79660
7500	482.6	2.0	421.4	31.2	78740

test at 1500 rpm. The procedure was repeated at all speeds from 1500 rpm to 7500 rpm with an interval of 50 rpm. Figure 6.32 shows VOI as a function of spindle speed. It is seen that VOI is highest at 1900 rpm. Therefore, the best test speed is 1900 rpm.

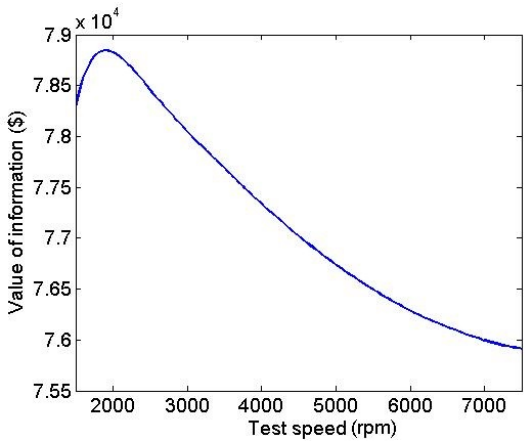

Figure 6.32: Value of information for the first test. The maximum value of information is obtained at 1900 rpm.

A test was performed at 1900 rpm using the procedure describes in Section 6.2.4. Figure 6.33 shows the variation of FWW with cutting time for tests at 1900 rpm. . The tool life was linearly interpolated between adjacent intervals if it exceeded 0.3 mm at the final measurement interval. The time to reach a FWW of 0.3 mm was equal to 164 min for testing at 1900 rpm. The prior cdf was updated using the procedure described in Section 6.2 using the experimental result. The VOI calculation procedure was repeated to find the next test speed. After the first update, the posterior was used as the new prior. Again, before performing the tests, it was assumed that a

test at any speed would yield the expected tool life at that speed. Figure 6.34 shows the value of information for the second test. According to this figure, the best test speed for the second test is 7500 rpm. A test was performed at 7500 rpm and a tool life of 3.2 min was obtained. The prior (which is the posterior after the first update) was again updated using the measured result. The procedure was repeated a third time to determine the next spindle speed for testing. Figure 6.35 shows the value of information for the third test. The test speed was 7100 rpm and the measured tool life was 3.7 min. Table 6.18 summarizes the results.

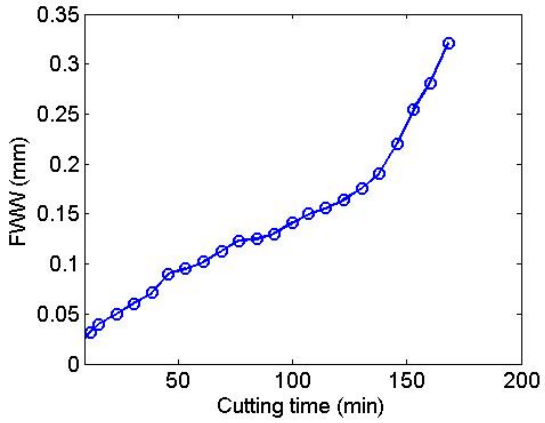

Figure 6.33: Increase in FWW with cutting time at 1900 rpm.

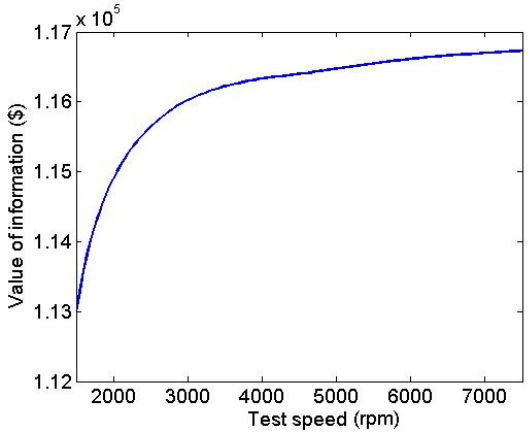

Figure 6.34: Value of information for the third test. The maximum value of information is obtained at 7100 rpm.

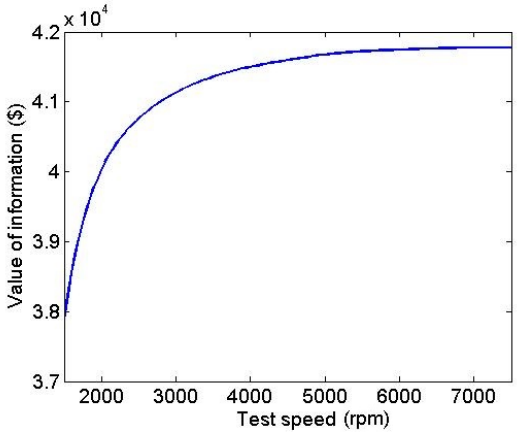

Figure 6.35: Value of information for the third test. The maximum value of information is obtained at 7500 rpm.

Table 6.18: Value of information for different spindle speeds

Test number	Test speed (rpm)	VOI ($)	Tool life (min)
1	1900	78847	164
2	7500	116730	3.2
3	7100	41777	3.7

6.6 Conclusions

A Bayesian inference approach to tool life prediction was demonstrated using a random walk method. In Bayesian inference, tool life is characterized by a probability distribution and the distribution is updated when new information is available. When new information in the form of experimental results is obtained, uncertainty in the prior distribution can be reduced. Bayesian inference therefore provides a way to combine prior data with experimental values to update beliefs about uncertain variables. Using the random walk approach for milling, the prior probability of tool life was generated using sample tool life curves, where each path potentially represented the true tool life curve. The probability that each sample path represented the true Taylor tool life curve was updated using Bayesian inference. A likelihood function was defined to describe how likely it was that that the sample tool life curve was

the correct choice given the measurement result at a particular spindle speed. An uncertainty of 20% was assumed for the measured tool life. The posterior tool life distribution was then used to predict the values of tool life at different spindle speeds and the results were compared to experiment. The same procedure was repeated using an extended form of the Taylor tool life equation to incorporate the effects of both cutting speed and feed in turning. In this case, sample tool life surfaces were generated. The probability that a sample surface was the true tool life surface was updated using Bayesian inference. The posterior tool life distribution agreed with the experimental results in both cases. Comparisons were also made to deterministic predictions using a least squares best fit to identify the Taylor tool life model empirical constants.

A value of information approach was implemented to select the best experimental test speed(s). The value of information was defined as the expected cost prior to testing minus the expected cost after testing. The experimental test point was then chosen which added the most (expected) value to the profit. This approach combined Bayesian inference with decision analysis.

CHAPTER 7: OPTIMAL PARAMETER DECISION: TITANIUM MILLING

7.1 Research Plan and Scope

The objective of this chapter is to apply the fundamental principles of decision analysis to optimal machining parameter selection in milling, while considering the uncertainty in both tool wear and stability. As a first step towards defining the milling problem, an influence diagram, which provides a graphical representation of a decision situation and the corresponding uncertainties, is provided in Figure 7.1. An influence diagram consists of several nodes with arrows connecting them. The nodes include: decision (rectangle), uncertainty (oval), value (hexagon), and deterministic (double oval) types. The arrows represent relevance between the nodes. In the figure, the objective function is profit which is represented as a value node. For constant revenue, minimizing the machining cost leads to maximized profit. The machining cost can be expressed as:

$$C = t_m r_m + \frac{(t_m r_m + C_{te}) t_c}{T} \tag{7.1}$$

where t_m is the total machining time in minutes, r_m is the rate (cost per unit time) for operating the machine in \$/min, t_{ch} is the tool changing time in minutes, C_{te} is the cost of the tool in \$, t_c is the cutting time in minutes, and T is the tool life in minutes. The machining and cutting times are dependent on the tool path, which, in turn, depends on the machining parameters, including spindle speed, Ω, feed rate, f_r, axial depth of cut, b, and the radial depth of cut, a. The tool life is also dependent on the machining parameters. The cost per unit time and tool changing time depend

on the selected machine.

The machining parameters, Ω, f_r, b, and a and the tool path are selected by the user and represent the decision nodes. However, there is uncertainty in the machining cost as a result of uncertainty in stability and tool life, which both depend on the selection of the machine, tool, part material, and machining parameters. The objective of this research is to select the optimal machining parameters which minimize cost while considering the uncertainty in tool life, and stability, for a given machine, tool, tool path and workpiece material. A titanium alloy has been selected due to its commercial relevance and low machinability.

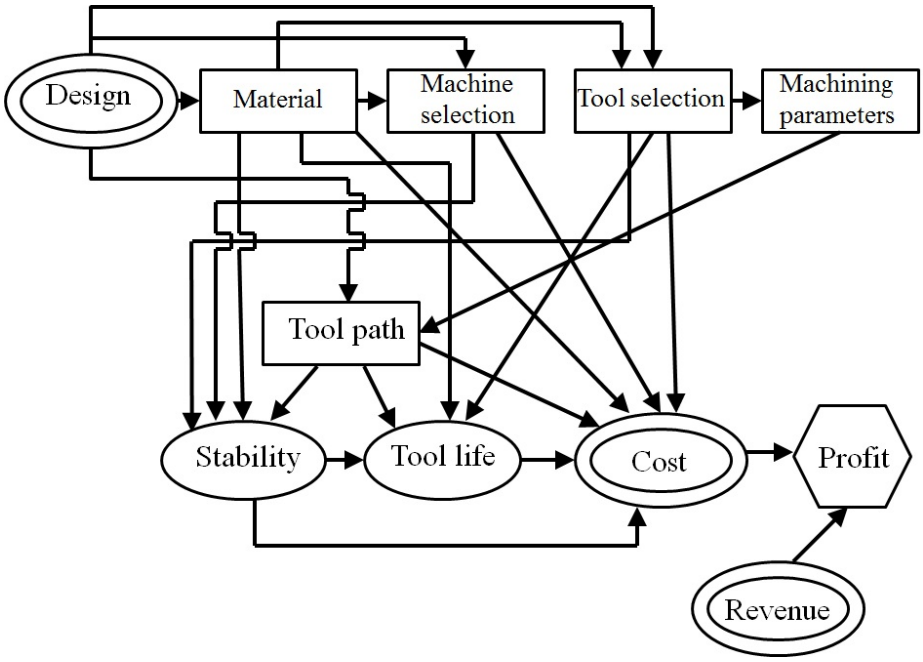

Figure 7.1: Influence diagram for milling optimization in the presence of uncertainty in stability and tool life. The design is assumed to include the part model/design drawings, dimensions and tolerances, and desired functionality.

The data in the uncertain nodes can be represented by distribution trees. The potential outcomes associated with each uncertainty are described using probabilities in a distribution tree (see Figure 7.2). In Figure 7.2, p_s denotes the probability of stability for a given parameter combination and p_t denotes the probability of tool failure for a given tool life at a given parameter combination. For a selected set of

machining parameters, defined in the corresponding decision node, the uncertainties in stability and tool life (uncertain) nodes are quantified in the process distribution tree.

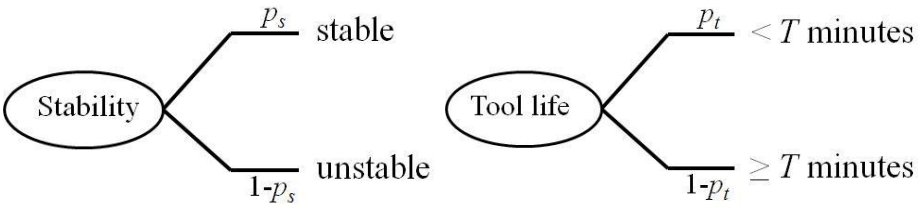

Figure 7.2: Probability tree of stability (left) and tool wear (right)

The uncertainty node probability trees shown in Figure 7.2 are combined to construct the process probability tree. The probability tree represents all possible combinations of outcomes and their probabilities. Figure 7.3 displays the probability tree for milling parameter selection. The probability of each path through the tree is the product of the probabilities at the branches, which is the joint probability of the outcomes. For example, at selected machining parameters, the probability of obtaining: 1) stable cutting conditions; and 2) a tool life greater than the selected tool life value is the product: $p_s(1- p_t)$. Note that the sum of all the joint probabilities must be unity since the outcomes are mutually exclusive and collectively exhaustive.

Each path has a corresponding machining cost associated with it. The total machining cost for the selected machining parameters and tool path also depends on the stability of the operating conditions, the tool life, and the final part accuracy. For example, if the tool fails before the tool change time, there is additional cost incurred due to the loss of machining time and subsequent reworking (or scrapping) of the part. Similarly, if the final machined surface is undercut (i.e., less material is removed than commanded due to forced vibrations during cutting), additional cost is required to rework the part. If it is overcut (i.e., more material is removed than commanded), however, the part may need to be scrapped and machined again unless material can be added back (by welding, for example) prior to re-machining. These

costs are incorporated in the machining costs as follows. Let U be the additional cost associated with unstable cutting conditions, and L be the additional cost associated with tool failure. Let C be the cost of machining the part under stable cutting conditions given by Eq 7.1. The values U and L need not be determined accurately; they can be based on subjective assessment of the user depending on the cost of the part and the tool. In this way, the cost associated of machining the part under stable cutting conditions and having a tool failure is $C + L$, since, in addition to the machining cost, extra cost is required to address the tool failure. Figure 7.3 also shows the machining costs associated with each path of the probability tree. Each selected (Ω, f_t, b, a) combination will have an expected machining cost which is equal to the product of the probability of the path and the cost associated with the path. (Recall that the value of p_t is dependent on T.) For a selected set of machining parameters, T can be chosen such that the expected machining cost is minimum. For a risk neutral user, the optimum combination of machining parameters will be the one with the lowest expected machining cost.

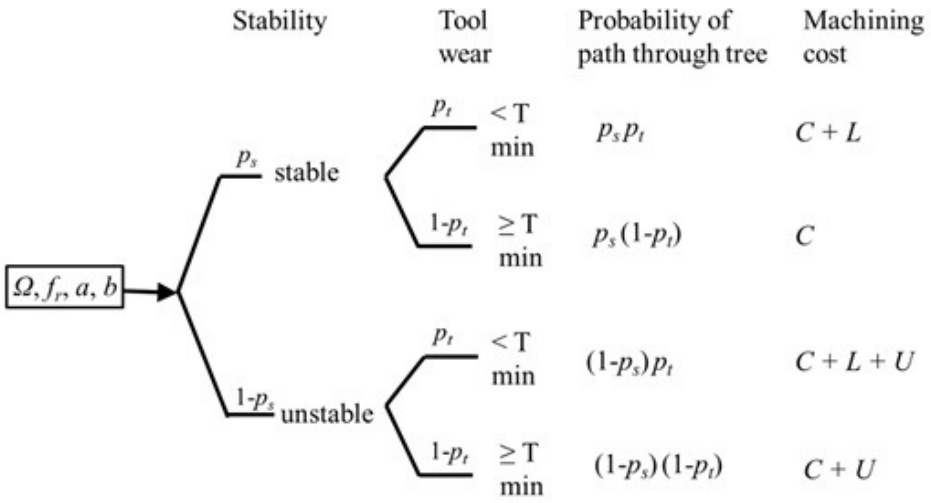

Figure 7.3: Probability tree for the decision problem with machining cost for each path.

7.2 Application

The procedure for optimal machining parameter was completed for machining a Ti-6Al-4V part. Titanium and titanium alloys find widespread application due to excellent corrosion resistance, high strength-to-weight ratio, and the ability to maintain their properties at high temperatures. However, titanium has a low thermal conductivity which results in reduced tool life at high speed and feed rates. As a result, titanium machining is traditionally restricted to low cutting speeds (v = 30 m/min - 50 m/min) [70, 71, 72]. Improving titanium machining productivity remains a challenge and, therefore, titanium was selected for this study. The objective is to find the optimal parameters for machining titanium considering uncertainty in stability and tool wear. As shown in Chapter 5, there is increased stability at low spindle speeds (1000 rpm) due to the process damping phenomenon. The goal is to find the optimum among the stable operating points considering the cost of tool, tool life and the cost of tool failure. For titanium, note that there is a trade-off between higher speeds and tool life. Higher cutting speeds enable higher material removal rates, but the tool life decreases exponentially at higher speeds which increases the cost.

Figure 7.4 shows the demonstration part, an I-section that was selected to model common aerospace components. The dimensions of the initial block are 152.4 mm $\times$ 80 mm $\times$ 76.2 mm. The thickness of the flanges and the ribs is 12.7 mm with a depth of 12.7 mm. The total volume to be removed by machining was calculated as 1.063 $\times$ 105 mm^3. The machining center was a three-axis CNC Haas TM-1 milling machine. A single-tooth indexable square end mill, 18.54 mm diameter (Kennametal model KICR-0.73-SD3-033.3C) was used. The inserts were coated carbide with a 15 degree relief angle, 0 degree rake angle, and no edge preparation and TiCN coating(Kennametal KC725M). Note that the selection of the machine, tool, and tool path were not considered in the decision framework (see Figure 7.1)

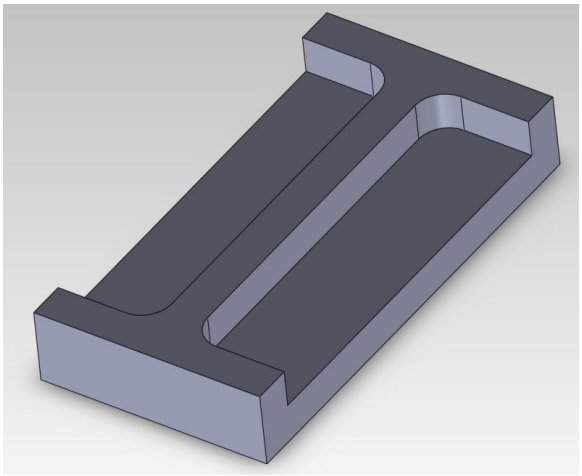

Figure 7.4: Solid model for the titanium I-section.

The next step was to decide the range of possible values for the machining parameters: spindle speed, axial depth, feed per tooth, and radial depth. For the Hass machine and tool selected, the maximum permissible spindle speed and axial depth values were 4000 rpm and 7 mm, respectively. The following ranges were selected for the machining parameters: 1) Ω: 200 rpm to 4000 rpm; 2) b: 0.5 mm to 7 mm; 3) f_t: 0.05 mm/tooth to 0.1 mm/tooth. For this work, the radial depth was kept constant at 9.27 mm (50% radial immersion). The ranges for Ω, b, and f_t were divided into discrete intervals of 100 rpm, 0.5 mm, and 0.025 mm/tooth, respectively, resulting in a total of 30861 possible parameter combinations. As stated, the optimal parameter combination is where the expected machining cost is the lowest. To calculate the expected machining cost, the first step was to determine the probability of stability, p_s, and the probability of tool failure as a function of tool life, p_t, for every parameter combination.

7.2.1 Stability Assessments

Each parameter combination selected has some probability of being stable, denoted by p_s, and a related probability of being unstable, (1- p_s). As shown in Chapter 4, the probability of stability can be modeled as a random walk in the absence

of knowledge of the system dynamics. The method is non-informative; it does not consider the underlying dynamics of the system. In this chapter, the probability of stability was assessed by performing a Monte Carlo simulation using the process damping stability model assuming uncertainty in the cutting force and process damping coefficients. The method is described in Chapter 5. The method takes advantage of the model and the system dynamics. In this case, the tool point frequency response function (FRF) of the system were measured and used in the process damping stability model. Figure 7.5 shows the FRFs for the machine's x (left) and y (right) direction. Note that no uncertainty is assumed in the measured FRFs.

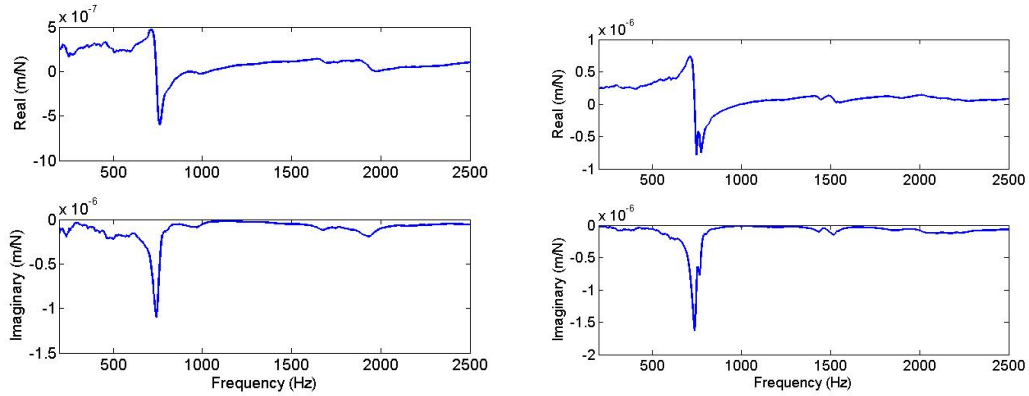

Figure 7.5: FRFs in the x (left) and y (right) directions.

The cutting force coefficients were identified using a linear regression on the mean forces in the x and y directions at different feed per tooth values. The cutting force was measured under stable cutting conditions using a cutting force dynamometer (Kistler model 9257B). For these tests, the insert wear was monitored using in-process optical flank wear measurements and the insert was replaced if the wear exceeded a predetermined value. The mean and standard deviation of the force coefficients were calculated from three measurements. The marginal prior distributions of the force coefficients were: $K_t = \mathrm{N}(2111.2,\ 78.3)$ N/mm^2 and $K_n = \mathrm{N}(1052.6,\ 27.9)$ N/mm^2, where N denotes a normal distribution and the terms in parenthesis provide the mean and standard deviation, respectively. The prior marginal distribution of

C was decided to be uniform, U(1.2×10^5, 0.1×10^5) N/m, where the values in the parenthesis denotes the lower limit and the upper limit, respectively [73]. The prior distributions of K_t, K_n, and C were assumed to be independent of each other. Note that, in practice, the coefficients may be correlated to each other; however, since no data regarding the correlation value was available, an independent assumption is appropriate since it is conservative. Random samples (1×10^5) were drawn from the prior distributions of and the stability limit was calculated for each sample. Figure 7.6 shows the prior cumulative distribution function (cdf) of stability. Figure 7.7 show the probability of stability, p(stability), as a function of axial depth at 1500 rpm (left) and 4000 rpm (right), respectively. As expected, the probability of stability decreases at higher axial depths at a given spindle speed.

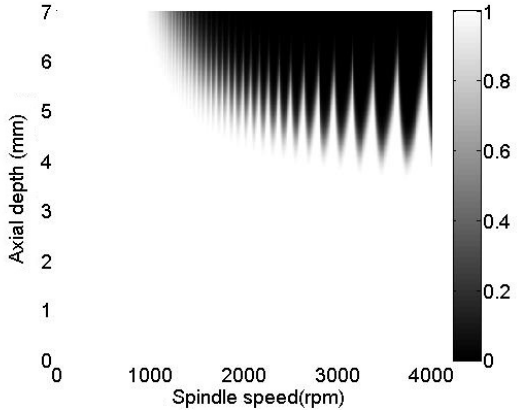

Figure 7.6: Prior cdf of stability.

7.2.2 Tool Life Assessments

Tool wear can impose a significant limitation on machining productivity, particularly for titanium alloys. In this study, the dependence of tool life on spindle speed, feed per tooth and axial depth was considered. An extended Taylor-type tool life equation was used as shown in Eq. 7.2.

$$\Omega^p f_t^q b^r T = C \tag{7.2}$$

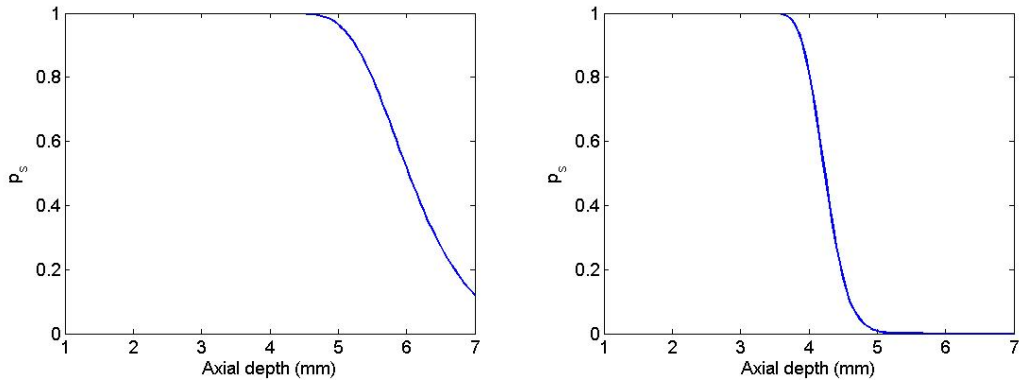

Figure 7.7: Probability of stability at 1500 rpm (left) and 4000 rpm (right).

where p, q, r, and C are the Taylor tool life constants. Note that the value of tool life at a given (Ω, f_t, b) combination is more sensitive to the exponents, p, q, and r, than the constant C. The dependence of tool life on radial depth was not considered [10]. As noted, the Taylor-type tool life constants are uncertain; the first step is to determine their distributions.

Tyler *et al.* performed tool wear tests using the same Kennametal insert and Ti-6Al-4V work material [73]. Figure 7.8 shows the tool life values as a function of spindle speed [73]. Based on the experimental results, the distributions of the Taylor tool life constants were calculated as: 1) p = N(1.05, 0.01); 2) q = N(1.00, 0.01); 3) r = N(1.00, 0.01); and 4) C = N(267, 10). The distribution of the coefficients was based on the experimental results reported in [73] and the user's beliefs regarding tool life distributions at different feeds and speeds. N here denotes a normal distribution and the terms in the parenthesis denote the mean and standard deviation, respectively. The exponent p has a mean value higher than the exponent's q and r, implying a stronger dependence on spindle speed than feed per tooth and axial depth.

A Monte Carlo simulation was performed to determine the distribution of tool life. Random samples were drawn from the prior distributions of the Taylor constants and the tool life was calculated for each (Ω, f_t, b) combination. The prior distributions of the constants were assumed to be independent of each other. To illustrate, Figure 7.9

shows the histogram of tool life at 500 rpm, 1000 rpm, and 3000 rpm. The feed per tooth value was 0.05 mm/tooth and the axial depth was 2 mm. The experimental values reported in [73] are denoted by 'x'. Figure 7.10 shows the mean tool life as a function of spindle speed and axial depth at 0.05 mm/tooth (top left), 0.075 mm/tooth (top right) and 0.01 mm/tooth (bottom right). The tool life samples were used to calculate the cdf of tool life for each (Ω, f_t, b) combination. To illustrate, Figure 7.11 shows the cdf of tool life at different spindle speeds; the vertical axis denotes the probability of tool failure, p_t.

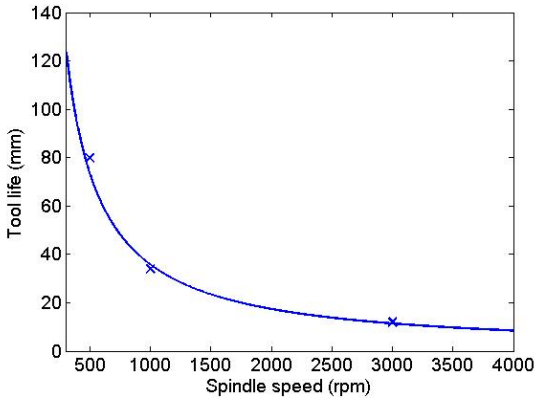

Figure 7.8: Experimental tool life values reported in [ref].

7.3 Results

The probability of stability and probability of tool life were used to calculate the expected cost for each machining parameter combination; see Figure 7.1. Note that for a selected (Ω, f_t, b) combination, the probability of tool failure is a function of the selected tool life value. Therefore, the expected cost calculation is performed at every possible tool life value with a probability of tool failure from zero to unity. The optimum tool life value for a certain (Ω, f_t, b) combination is selected as the value which minimizes expected cost; see the cost calculation procedure described in Chapter 6. The cost associated with the tool failure was taken as \$1000. The cost of an unstable cut was assumed to be negative infinity due to the potential damage

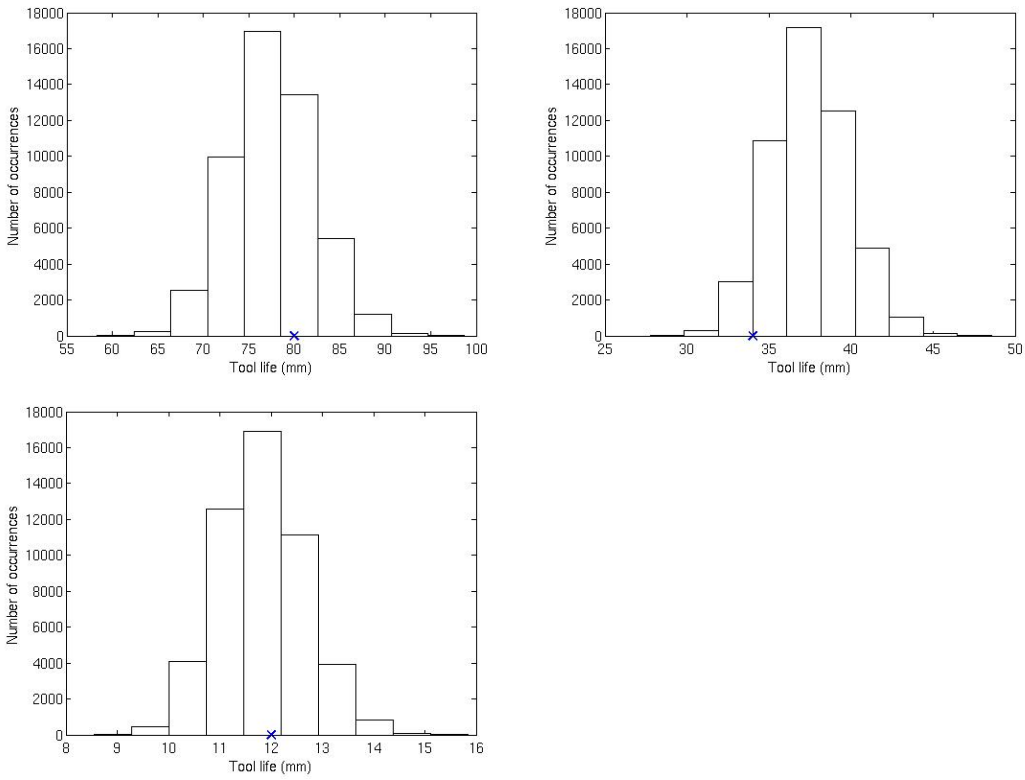

Figure 7.9: Histogram of tool life at 500 rpm (top left), 100 rpm (top right), and 3000 rpm (bottom left).

to the part and spindle. This specification implies that machining is not feasible at unstable cutting conditions. Therefore, machining parameter combinations which are known to be stable with certainty *a priori* are considered for the optimal calculation. The parameters used for cost calculations are summarized in Table 7.1.

The procedure is repeated at every (Ω, f_t, b) combination; Table 7.2 summarizes the optimum parameters for milling the part. The time required for machining was 6.74 minutes with an expected cost of $191. The tool path was generated using MasterCam; the actual machining time was measured to be as 7.27 minutes. Figure 7.12 shows the final machined surface. The machining of the I-section was stable; as noted, the probability of stability was equal to unity at the optimum machining parameters. Table 7.2 also lists the manufacturer/handbook recommended feed and speed values for the given tool-workpiece combination [72, 74]. The recommended parameters do

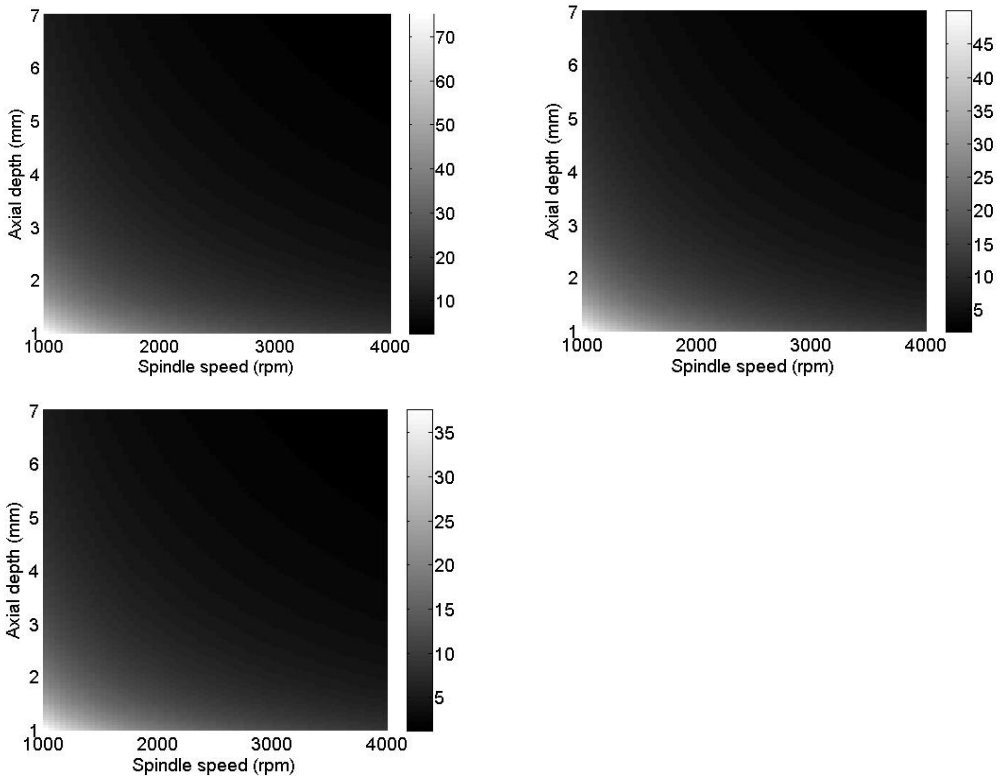

Figure 7.10: Mean tool life as a function of spindle speed and axial depth at 0.05 mm/tooth (top left), 0.075 mm/tooth (top right) and 0.01 mm/tooth (bottom left).

not take into account the dynamics and stability of the system and the probabilistic nature of tool life and are therefore conservative. As observed, there is a 90% reduction in the cost to machine the part.

As shown, the probability distributions of stability and tool life can be updated using experimental results and Bayes' rule. The procedure is as follows. The random walk method for Bayesian updating can be used to update the probability that each sample path is the true path using experimental results. For a particular machining parameter combination, an experimental result provides stable/unstable and tool life. The procedure is described in detail for application to stability and tool life in Chapter 4/Chapter 5 and Chapter 6, respectively. Note that for tool life, the sample paths will be modified to sample volumes since the dependence of tool life on axial depth is considered along with feed and speed. However, depending on the prior

Table 7.1: Parameters for cost calculations

Parameter	Value	Unit
r_m	10	\$/min
$t_c h$	2	min
$C_t e$	10	\$
L	1000	\$
U	$-\infty$	\$

Table 7.2: Optimum machining parameters for the part.

Parameter	Optimum		Recommended	
	Value	Unit	Value	Unit
Ω	3900	rpm	1000	rpm
f_t	0.1	mm/tooth	0.05	mm/tooth
a	9.27	mm	9.27	mm
b	4	mm	2	mm
T	1.68	min	5	min
p_s	0.003		-	
p_t	1		-	
$Cost$	191	\$	1834	\$

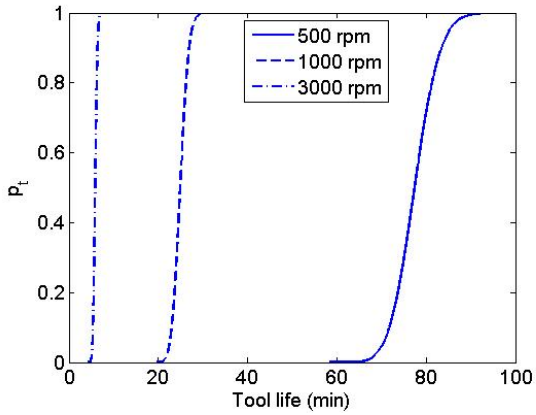

Figure 7.11: Probability of tool failure as a function of spindle speed.

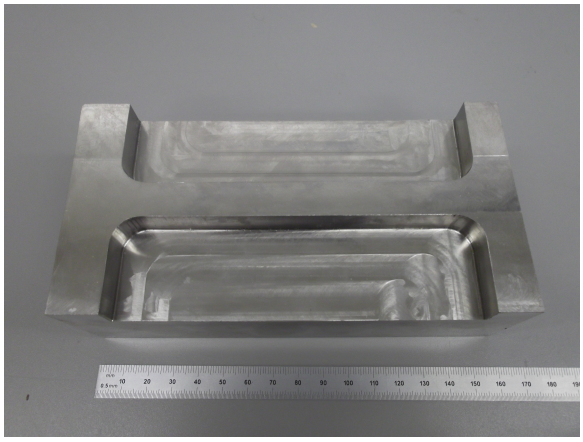

Figure 7.12: Machined I-section.

beliefs, additional experimentation may not be worthwhile. Therefore, the value of experimentation method should be used to determine if additional testing is necessary and at which parameters the tests should be performed. The procedure to calculate value of information is also described in Chapters 4 - Chapter 6.

7.4 Conclusions

A decision analytic framework for optimal machining parameter selection in titanium milling was described in this chapter. The objective was to minimize expected machining cost, considering uncertainty in stability and tool life. The data in the uncertain stability and tool life nodes were represented by distribution trees and com-

bined to form a process probability tree. Here, p_s denoted the probability of stability for a given parameter combination and p_t denoted the probability of tool failure for a given tool life at a given parameter combination. For a machining parameter combination, the outcomes in stability (stable/unstable) and tool life (failure/no failure) have a probability and a cost associated with them. The expected cost was calculated as a product of the probabilities and the cost. The optimal machining parameters were selected to minimize the expected machining cost.

CHAPTER 8: CONCLUSIONS AND FUTURE SCOPE

The research is this dissertation focuses on optimal machining parameter selection in milling, while considering uncertainty in tool life and machining stability. The research was divided into three steps: 1) consider uncertainty in stability neglecting tool wear; 2) consider uncertainty in tool life assuming stable cutting conditions; and 3) combine uncertainty in both stability and tool wear. In the first step, stability was characterized as a probability distribution instead of a deterministic boundary. The distribution of stability was updated using experimental results. Two approaches were considered: 1) the prior distribution of stability was modeled using a random walk method assuming no underlying model; and 2) a process damping model was used to model stability distributions. A value of information method was used for selecting test points and the method converged to optimum machining parameters by maximizing the value gained from the test. The proposed method has many advantages over traditional design of experiments techniques, such as response surface methodology and Taguchi orthogonal arrays. In the second step, tool life was modeled using a probability distribution which was updated using experimental results. The method was used for pre-process selection of optimal spindle speed and corresponding tool life value. In the final approach, uncertainties in stability and tool life were combined. The optimal parameter selection was based on minimizing the expected machining cost. Results showed a 90% decrease in cost for milling a particular titanium part compared to the manufacturer/handbook recommended parameters.

The future scope of the research is to work on a generalized probabilistic and decision theory-based approach for dealing with uncertainty in manufacturing. A

preliminary objective is to develop a unified approach for selecting optimal machining parameters considering uncertainties in stability, tool wear, surface location error, and surface roughness. In addition, a decision framework methodology could be developed to include decisions such as selecting the best manufacturing process, tool, and tool path. Additional studies in the manufacturing domain will focus on uncertainty quantification and analysis concerning free-form surface metrology and tool condition monitoring.

REFERENCES

[1] Tlusty, J., and Polacek, M., The stability of machine tools against self-excited vibrations in machining, Proceedings of the ASME International Research in Production Engineering Conference, 205 (1963), 465-474.

[2] Tlusty, J., Zaton, W., and Ismail, F., Stability lobes in milling, Annals of the CIRP, 32(1) (1983), 309-313.

[3] Tobias, S. A., and Fishwick, W., Theory of Regenerative Machine Tool Chatter, The Engineer, London, 258 (1958).

[4] Merrit, H., Theory of self-excited machine tool chatter, Journal of Engineering for Industry, 87 (1965), 447-454.

[5] Arnold, R., The Mechanism of Tool Vibration in the Cutting of Steel, Proceedings of the Institution of Mechanical Engineers, 54 (1946), 261-284.

[6] Gradisek, J., Govekar, E., Grabec, I., and Kalveram, M. On stability prediction for low radial immersion milling, Journal of Machine Science and Technology, 9(1) (2005), 117-130.

[7] Bayly, P., Halley, J., Mann, B., and Davies, M. Stability of interrupted cutting by temporal finite element analysis, Journal of Manufacturing Science and Engineering, 125(2) (2003), 220-225.

[8] Mann, B., Bayly, P., Davies, M., and Halley, J. Limit cycles, bifurcations, and accuracy of the milling process, Journal of Sound and Vibration, 277(1-2) (2004), 31-48.

[9] Campomanes, M., and Altintas, Y. An improved time domain simulation for dynamic milling at small radial immersions, Journal of Manufacturing Science and Engineering, 125(3) (2003), 416-422.

[10] Tlusty, J., Manufacturing Processes and Equipment, Prentice Hall, Upper Saddle River, NJ, 2000.

[11] Dimla, E., and Snr., D. Sensor signals for tool-wear monitoring in metal cut-ting operations: a review of methods, International Journal of Machine Tools and Manufacture, 40 (2000), 1073-1098.

[12] Tool life testing using single-point turning tools, ISO.

[13] Howard, R., Decision analysis: applied decision theory, In Proceedings of the 4th International Conference on Operational Research (1966), 55-57.

[14] Howard, R., Decision analysis: Practice and promise, Management Science, 34 (1988), 679-695.

[15] Raiffa, H., Decision Analysis: Introductory Lectures on Choices under Uncertainty, Addison-Wesley, Reading, MA, 1968.

[16] Howard, R., Information value theory, IEEE Transactions on Systems Science and Cybernetics, 2(1) (1966), 22-26.

[17] Howard, R., Decision analysis: perspectives on inference, decision and experimentation, Proceedings of the IEEE, 58(5) (1970), 632-643.

[18] Gelman, A., Carlin, J., Stern, H., and Rubin, D, Bayesian Data Analysis, Chapman and Hall/CRC Press, Boca Raton, FL, 2009.

[19] Grimmett, G., and Stirizaker, D, Probability and Random Processes, Oxford University Press, New York, NY, 2004.

[20] Neumann, J. V., and Morgenstern, O., Theory of Games and Economic Behaviour, Princeton University Press, Princeton, NJ, 1944.

[21] Grayson, C. Jr., Decisions Under Uncertainty: Drilling Decisions by Oil and Gas Operators, Harvard Business School, Division of Research, Boston, MA, 1960.

[22] Newendorp, P., Decision Analysis for Petroleum Exploration, Penn Well Books, Tulsa, OK, 1975.

[23] Brennan, M., and Schwartz, E., Evaluating natural resource investments, Journal of Business, 58 (1985), 135-157.

[24] Olsen, T., and Stensland, G., Optimal shut down decisions in resource extraction, Economics Letters, 26 (1988), 215-218.

[25] Paddock, J., Siegel, D., and Smith, J., Option valuation of claims on real assets: The case of o shore petroleum leases, Quarterly Journal of Economics, 103 (1988), 479-508.

[26] Clarke, H., and Reed, W., Oil-well valuation and abandonment with price and extraction rate uncertain, Resources and Energy, 12 (1990), 361-382.

[27] Keefer, D., Resource allocation models with risk aversion and probabilistic dependence: O shore oil and gas bidding, Management Science, 37 (1991), 377-395.

[28] Gibson, R., and Schwartz, E., The Valuation of Long Term Oil-Linked Assets, In Stochastic Models and Option Values, Elsevier Science Publishers, B.V,

Amsterdam, Ned., 1991.

[29] Smith, J., and McCardle, K., Valuing oil properties: Integrating option pricing and decision analysis approaches, Operations Research, 46(2) (1998), 198-217.

[30] Schmitz, T., and Smith, K., Machining Dynamics: Frequency Response to Improved Productivity, Springer, New York, NY, 2009.

[31] Kumanchik, L., and Schmitz, T., Improved analytical chip thickness model for milling, Precision Engineering, 31 (2007), 317-324.

[32] Andrieu, C., de Freitas, N., Doucet, A., and Jordan, M., An introduction to MCMC for machine learning, Machine Learning, 50 (2003), 5-43.

[33] Metropolis, N., Rosenbluth, A., Rosenbluth, M. N., Teller, A., and Teller, E., Equations of state calculations by fast computing machines, Journal of Chemical Physics, 21(6) (1953), 1087-1092.

[34] Hastings, W. Monte Carlo sampling methods using Markov chains and their applications, Biometrika, 57 (1970), 97-109.

[35] Roberts, G., Gelman, A., and Gilks, W., Weak convergence and optimal scaling of random walk metropolis algorithms, Annals of Applied Probability 7(1) (1997), 110-112.

[36] Duncan, G., Kurdi, M., Schmitz, T., and Snyder, J., Uncertainty propagation for selected analytical milling stability limit analyses, Transactions of NAMRI/SME, 34 (2006), 17-24.

[37] Taylor, F., On the art of cutting metals, Transactions of the ASME, 28 (1906), 31-248.

[38] Merchant, M., Metal cutting research theory and practice, ASM (1950), 5-44.

[39] Komanduri, R., Machining and grinding: A historical review of the classical papers, Applied Mechanics Review, 46(3) (1993), 80-132.

[40] Koenisgberger, F., and Sabberwal, A., An investigation into the cutting force pulsations during milling operations, International Journal of Machine Tool Design and Research, 1 (1961), 15-33.

[41] Tlusty, J., Analysis of the state of research in cutting dynamics, Annals of the CIRP, 27(2) (1978), 583-589.

[42] Smith, S., and Tlusty, J., An overview of modeling and simulation of the milling process, Journal of Engineering for Industry, 113(2) (1991), 169-175.

[43] Smith, S., and Tlusty, J., Efficient simulation programs for chatter in milling, Annals of the CIRP, 42(1) (1993), 463-466.

[44] Smith, S., and Tlusty, J., Current trends in high-speed machining, Journal of Manufacturing Science and Engineering, 119(4B) (1997), 655-663.

[45] Ehmann, K., Kapoor, S., DeVor, R., and Lazoglu, I., Machining process modeling: A review, Journal of Manufacturing Science and Engineering, 119(4B) (1997), 655-663.

[46] Altintas, Y., and Weck, M., Chatter stability of metal cutting and grinding, Annals of the CIRP, 53(2) (2004), 619-642.

[47] Merchant, M., An interpretive look at 20th century research on modeling of machining, Machining Science and Technology, 2(2) (1998), 157-163.

[48] Schmitz, T., and Duncan, G., Three-component receptance coupling sub-structure analysis for tool point dynamics prediction, Journal of Manufacturing Science and Engineering, 127(4) (2005), 781-790.

[49] Kim, H., and Schmitz, T., Bivariate uncertainty analysis for impact testing, Measurement Science and Technology, 18 (2007), 3565-3571.

[50] Hicks, C., and Turner, K. Jr., Fundamental concepts in the design of experiments, Oxford University Press, New York, NY, 1999.

[51] Jiju, A., Design of experiments for engineers and scientists, Elsevier Ltd., Burlington, MA, 2003.

[52] Tobias, S., Machine Tool Vibrations, Blackie and Sons Ltd., Glasgow, UK, 1999.

[53] Altintas, Y., and Budak, E., Analytical prediction of stability lobes in milling, Annals of the CIRP, 44(1) (1995), 357-362.

[54] Wallace, P., and Andrew, C., Machining forces: Some effects of tool vibration, Journal of Mechanical Engineering Science, 7 (1965), 152-162.

[55] Sisson, T. R., and Kegg, R. L., An explanation of low-speed chatter effects, Journal of Engineering for Industry, 91 (1969), 951-958.

[56] Peters, J., Vanherck, P., and Van Brussel, H., The measurement of the dynamic cutting coe cient, Annals of the CIRP, 21(2) (1971), 129-136.

[57] Wu, D. W., A new approach of formulating the transfer function for dynamic cutting processes, Journal of Engineering for Industry, 111 (1989), 37-47.

[58] Elbestawi, M. A., Ismail, F., Du, R., and Ullagaddi, B. C., Modeling machining dynamics damping in the tool-workpiece interface, Journal of Engineering for Industry, 116 (1994), 435-439.

[59] Lee, B. Y., Trang, Y. S., and Ma, S. C., Modeling of the process damping force in chatter vibration, International Journal of Machine Tools and Manufacture, 35 (1995), 951-962.

[60] Huang, C. Y., and Wang, J. J., Mechanistic modeling of process damping in peripheral milling, Journal of Manufacturing Science and Engineering, 129 (2007), 12-20.

[61] Ahmadi, K., and Ismail, F., Experimental investigation of process damping nonlinearity in machining chatter, International Journal of Machine Tools and Manufacture, 50 (2010), 1006-1014.

[62] Budak, E., and Tunc, L. T., A new method for identification and modeling of process damping in machining, Journal of Manufacturing Science and Engineering, 131 (2009), 1-10.

[63] Altintas, Y., Eynian, M., and Onozuka, H., Identification of dynamic cutting force coe cients and chatter stability with process damping, Annals of the CIRP, 57(1) (2008), 371-374.

[64] Tyler, C., Schmitz, T., Process damping analytical stability analysis and validation, Transactions of the NAMRI/SME, 40 (2012), 37-47.

[65] Stephenson, D., and Agapiou, J., Metal Cutting Theory and Practice, CRC Press, Boca Raton, FL, 2006.

[66] Kronenburg, M., Machining Science and Application, Pergamon Press, Ox-ford, MA, 1966.

[67] Creese, R., Introduction to Manufacturing Processes and Equipment, Marcel Dekker, Inc., New York, NY, 1999.

[68] Cui, Y., Fussell, B., Jerard, R., and Esterling, D., Tool wear monitoring for milling by tracking cutting force model coefficients, Transactions of NAMRI/SME, 37 (2009), 613-620.

[69] Karandikar, J., Schmitz, T., and Abbas, A., Tool life prediction using Bayesian updating, Transactions of NAMRI/SME, 39 (2011), 17-24.

[70] Jawaida, A., Che-Hatona, C., and Abdullah, A., Tool wear characteristics in turning of titanium alloy Ti-6246, Journal of Material Processing Technology, 92

(1999), 329-334.

[71] Su, Y., He, N., Li, L., and Li, X, An experimental investigation of effects of cooling/lubrication conditions on tool wear in high-speed end milling of Ti-6Al-4V, Wear, 261(7-8) (2006), 760-766.

[72] Odberg, E., Jones, F., Horton, F., Ryffel, H., Machinery's handbook, 28th Edition, Industrial Press, NY, 2009.

[73] Tyler, C., and Schmitz, T., Process damping coefficient identification for milling, Proceedings of ASPE annual meeting, October, 2013.

[74] Kennametal website: http://www.kennametal.com/kennametal/en/products/.

VITA

The author was born in the city of Mumbai (formerly known as Bombay), India in 1985. After spending his early years in Mumbai, he, along with his family, moved to the small town of Pune, India, popularly known as the Oxford of the East. After finishing his high school education in 2003, he pursued his under-graduate degree in Mechanical Engineering at the University of Pune, India. After four grueling years of studies, project assignments and voluntary community service activities, the author obtained his Bachelor's degree in mechanical engineering with distinction. After working with Forbes Marshall Pvt. Ltd. as a design engineer for a year, the author quit his job in order to pursue graduate studies in Mechanical Engineering at University of Florida (UF), Gainesville. He completed his Master's with thesis from UF in May 2010. The author transferred to UNCC in January 2011 to continue his PhD studies with Dr. Tony L. Schmitz at the Center for Precision Metrology. The author plans to join Georgia Tech as a post-doctoral research associate after graduation.